

PYROCLASTS: A WINDOW INTO THE VOLCANIC CONDUIT

by

KATHLEEN R. TRAFTON

A DISSERTATION

Presented to the Department of Earth Sciences  
and the Division of Graduate Studies of the  
University of Oregon in partial fulfillment of the  
requirements  
for the degree of  
Doctor of Philosophy

December 2021

DISSERTATION APPROVAL PAGE

Student: Kathleen R. Trafton

Pronouns: Any

Title: Pyroclasts: A Window into the Volcanic Conduit

This dissertation has been accepted and approved in partial fulfillment of the requirements for the Doctor of Philosophy degree in the Department of Earth Sciences by:

Thomas Giachetti	Chair
Leif Karlstrom	Core Member
Heather Wright	Core Member
Meredith Townsend	Core Member
Amanda Cook	Institutional Representative

and

Krista Chronister	Vice Provost of Graduate Studies
-------------------	----------------------------------

Original approval signatures are on file with the University of Oregon Division of Graduate Studies.

Degree awarded December 2021.

© 2021 Kathleen R. Trafton

## DISSERTATION ABSTRACT

Kathleen R. Trafton

Doctor of Philosophy

Department of Earth Sciences

December 2021

Title: Pyroclasts: A Window into the Volcanic Conduit

Billions of people live in the shadow of a volcano. Explosive eruptions produce myriad hazards, saturating airways with noxious gases and volcanic particles that damage infrastructure and crops. Above all, these eruptions result in loss of life. Better mitigating these hazards necessitates study of their erupted products, which can help constrain the size, duration, and potential impact of future eruptions and give a glimpse into the subterranean volcanic conduit. In Chapter II, I study thousands of porous pyroclasts from the 1060 CE eruption of Medicine Lake Volcano. I find that pyroclast's size, shape, and texture directly reflects conduit processes; sub-millimeter scale pyroclasts are more elongate and preserve elongated bubbles, whereas centimeter-scale pyroclasts are more blocky with roundish bubbles. In Chapter III, I use physical data from juvenile products to understand the explosive-effusive transition at 640 B.C. rhyolitic eruption of Newberry Volcano. I find pulsatory explosive behavior and changes in obsidian texture and proportion to herald the final switch to lava extrusion. In Chapter IV, I contextualize pumices from these eruptions with two eruptions from Mt. Mazama-Giiwas, finding that pumice in general can form from cyclic events of magma fragmentation and sintering. These studies not only change our modern perception of pyroclast formation and conduit



dynamics, but also importantly provide data usable in numerical tephra dispersion models.

## CURRICULUM VITAE

NAME OF AUTHOR: Kathleen R. Trafton

PRONOUNS: Any

GRADUATE AND UNDERGRADUATE INSTITUTIONS ATTENDED:

University of Oregon, Eugene, OR  
Colby College, Waterville, ME  
University of Geneva, Geneva, Switzerland

DEGREES AWARDED:

Doctor of Philosophy in Earth Sciences, University of Oregon  
Bachelor of Arts in Geology, Colby College  
Bachelor of Arts in French, Colby College

AREAS OF SPECIAL INTEREST:

Geologic hazard mitigation  
Physical characterization of erupted volcanic products  
Outreach and science education

PROFESSIONAL EXPERIENCE:

Graduate Teaching Fellow, University of Oregon, Eugene, 2016-2022  
Paleosedimentological Research Assistant, Colby College, 2015-2016  
Biogeochemical Research Assistant, Colby College, 2014  
Science, Technology, and Society Research Assistant, Colby College, 2013-2014  
Presidential Scholar Historical Research Assistant, Colby College, 2012-2013

GRANTS, AWARDS, AND HONORS:

Oregon representative, Catalyzing Advocacy in Science and Engineering  
Workshop, American Association for the Advancement of Science, 2020  
Steinman Award, University of Oregon, 2020  
Women in Graduate Sciences Karfilis Award, University of Oregon 2019  
Earth Sciences Travel Grant, University of Oregon, 2019  
Grant-in-Aid-of-Research, Sigma Xi, 2018  
Community for Minorities in STEM travel grant, University of Oregon, 2018  
Graduate Research Fellowship Program Honorable Mention, National Science  
Foundation, 2018  
Kleinman Grant, U.S. Geological Survey, 2017  
Research Grant, Geological Society of America, 2017  
Promising Scholar, University of Oregon, 2016

Alternate Fulbright Fellow, 2016  
Tagliacozzo Memorial Scholarship, American Institute of Professional Geologists, 2016  
Travel Grant, Geological Society of America, 2015  
Excellence in French award, Colby College, 2013, 2014, 2015  
Presidential research grant x2, Colby College  
Dana scholar – academic excellence, Colby College  
Marsden scholar – top geology student, Colby College  
Presidential scholar for outstanding scholastic merit, Colby College  
*Magna cum laude* and distinction in both majors, Colby College

#### PUBLICATIONS:

- Trafton, K. and Giachetti, T. (2021) Tracking the explosive-effusion transition through the geochemistry and physical attributes of juvenile products. *Bulletin of Volcanology* (submitted)
- Giachetti, T., Trafton, K., et al. (2021) The products of primary magmatic fragmentation finally revealed by pumice agglomerates. *Geology*.
- Trafton, K., Giachetti, T. (2021) The morphology and texture of Plinian pyroclasts reflect their lateral sourcing in the conduit. *Earth & Planetary Science Letters*.

## ACKNOWLEDGEMENTS

I thank my siblings, Jennifer and Carol Lipshultz, for their hearts in the face of disparaging odds. I would not be here without your support, and I am so proud of you. I thank my late father, who gave to me his mischievous curiosity, steadfast morality, and dancing feet. To my Eugene family, Anne, Jeff, Charles, Grace, and Adair Sharman: you brought me light on the darkest of winter days. I will never forget the meals we shared nor the games we played.

To my nat 20 of friends, Becca Bussard (strength), Lissie Connors (wisdom), Angela Olsen (charisma), Nicole Abib (intelligence), and Paul Regensburger (constitution): you helped me climb to new heights - metaphorically and literally. Angela, with you, I'm always in the mood for dancin' – you give me the feels! Becca, so long as you set to me, I can fly higher. To Becca and Sydeny [*sic*] Dybing, your authenticity – whether on grass or ice or in the hallowed (harrowing) halls of academia – proves that you were born to make history. To Amelia Winner, Brittany Carter, and Sage Kemmerlin, your antics will be sorely missed. You weathered the seasons with me and seasoned my life – with something other than cinnamon. See you on the homestead circa next decade.

I also acknowledge the consistent support and guidance of my advisor, Thomas Giachetti. Thank you for ensuring humanity remains in the sciences. I additionally recognize my committee for their time, patience, and valuable input. This research was supported by several grants, including ones from Sigma Xi, the U.S. Geological Survey, the Geological Society of America, and the University of Oregon.

## DEDICATION

This thesis is dedicated to Sage Kemmerlin. Her compassion and moral compass served as my foremost guide on the tortuous path of higher education. Ingenious, kind, and integrous, she embodies the truest nature of a scientist. I will forever strive to live up to her example. Thank you, Sage, for instilling in me the audacity to continue.

I remember the sounds of summer and rolling hills, the backdrop of effervescent liquid against the bucolic expanse.

“We’ll be best friends,” I said, hoping you’d agree.

And indeed, we weathered the seasons together, a cacophony of sorrow drowning the verdant vastness. The deluge poured again, and again, and time and time I found myself trapped in the grays of expectation and incident. But you extended an umbrella, hands chafed with vulnerability, a smile soft with sunrise.

And so I learned to craft my own umbrella.

And so too did we construct a shelter.

And so too would this stronghold asylum others seeking passage.

And, so too, did my smile take on the warmth of future days.

I will never forget the rain. Now, I hear the sounds of summer.

## TABLE OF CONTENTS

Chapter	Page
I. INTRODUCTION . . . . .	1
II. THE MORPHOLOGY AND TEXTURE OF PLINIAN PYROCLASTS REFLECT THEIR LATERAL SOURCING IN THE CONDUIT . . . . .	8
2.1. Introduction . . . . .	8
2.2. Background . . . . .	12
2.3. Methodology . . . . .	14
2.3.1. Sampling and preparation . . . . .	14
2.3.2. Homogeneous vs. heterogeneous pumices . . . . .	16
2.3.3. Density . . . . .	17
2.3.4. Clast shape . . . . .	17
2.3.5. Vesicle shape and size distributions . . . . .	18
2.4. Results. . . . .	20
2.4.1. Componentry . . . . .	20
2.4.2. External texture . . . . .	21
2.4.3. External morphology . . . . .	21
2.4.4. Internal texture . . . . .	23
2.4.4.1. Vesicle shape and size distributions . . . . .	23
2.4.4.2. Density . . . . .	24
2.5. Discussion . . . . .	25
2.5.1. Post-fragmentation alteration of pyroclast size . . . . .	29

Chapter	Page
2.5.2. Transport-related sorting . . . . .	32
2.5.3. Clast size and texture reflect lateral sourcing . . . . .	33
2.5.4. Syn-eruptive sintering of porous pyroclasts . . . . .	36
2.5.5. Tephra dispersion models . . . . .	38
2.6. Conclusions . . . . .	39
2.7. Bridge . . . . .	44
III. LEVERAGING PHYSICAL DATA OF JUVENILE SILICIC PRODUCTS TO UNDERSTAND THE EXPLOSIVE-EFFUSIVE TRANSITION . . . . .	45
3.1. Introduction . . . . .	45
3.2. Geologic Setting . . . . .	48
3.2.1. Locality . . . . .	48
3.2.2. The 640 C.E. Big Obsidian eruptive period . . . . .	50
3.3. Methodology . . . . .	51
3.4. Results . . . . .	53
3.4.1. General trends. . . . .	56
3.4.2. Lower Newberry Pumice (LP) . . . . .	56
3.4.3. Upper Newberry Pumice 1 (UP1) . . . . .	57
3.4.3.1. Lapilli-dominated layers. . . . .	57
3.4.3.2. Ash-dominated layers. . . . .	57
3.4.4. Upper Newberry Pumice 2 (UP2) . . . . .	59
3.5. Discussion . . . . .	59

Chapter	Page
3.5.1. LP .....	60
3.5.2. UP1 .....	63
3.5.3. UP2 .....	67
3.5.4. The continuity of the 640 CE eruption .....	68
3.5.5. Comparison with the eruption of Cordón Caulle. . . .	71
3.6. Conclusion .....	73
3.7. Bridge .....	74
IV. THE PRODUCTS OF PRIMARY MAGMA FRAGMENTATION FINALLY REVEALED BY PUMICE AGGLOMERATES .....	75
4.1. Introduction .....	75
4.2. Methods .....	77
4.3. Porosity and External Texture of the Lapilli Suites .....	78
4.4. Identifying Protopyroclasts .....	80
4.5. Sintering of Protopyroclasts .....	83
4.6. Implications .....	84
V. CONCLUSIONS .....	87
APPENDICES	
A. APPENDIX CHAPTER I: THE MORPHOLOGY AND TEXTURE OF PLINIAN PYROCLASTS REFLECT THEIR LATERAL SOURCING IN THE CONDUIT	
A.1. Methodological flowchart .....	90



Chapter	Page
A.2. Map of sample locations at Glass Mountain . . . . .	91
A.3. Methods used for determining the volume of a clast . . . . .	92
A.4. Volume determination . . . . .	93
Table A.1. Vesicle number data . . . . .	95
Table A.2. Componentry of the proximal and medial samples . . . . .	96
A.5. Plot of median elongation for clasts . . . . .	97
A.4. Interpretation supplement for Fig. 5d . . . . .	98
A.5. Vesicle size distributions . . . . .	99
A.6. Density-size distributions . . . . .	100
A.7. Grain Size distributions . . . . .	101
A.8. Density data for manually fragmented pyroclast . . . . .	102
B. APPENDIX CHAPTER II: LEVERAGING PHYSICAL AND GEOCHEMICAL DATA OF JUVENILE SILICIC PRODUCTS TO UNDERSTAND THE EXPLOSIVE-EFFUSIVE TRANSITION	
B.1. Square root of area vs. ln(thickness) plot . . . . .	103
C. APPENDIX CHAPTER III: THE PRODUCTS OF PRIMARY MAGMA FRAGMENTATION FINALL REVEALED BY PUMICE AGGLOMERATES	
C.1. Methodology elaboration . . . . .	104
C.2. Textural data table . . . . .	110
REFERENCES CITED . . . . .	111

## LIST OF FIGURES

Figure	Page
2.1. Pyroclasts from 1060 CE Medicine Lake eruption . . . . .	16
2.2. Percent of Medicine Lake pumices that are tubular . . . . .	22
2.3. Medicine lake pumice characteristics . . . . .	26
2.4. Percent texture by area . . . . .	27
2.5. Deformation and orientation of vesicles . . . . .	28
2.6. Porosity/density as a function of pyroclast size . . . . .	29
2.7. Terminal Velocity of pyroclasts . . . . .	40
2.8. Conceptual model of pyroclast formation . . . . .	43
3.1. Locality map of Newberry Volcano . . . . .	49
3.2. Stratigraphy of 640 CE Newberry Pumice deposit . . . . .	54
3.3. Physical attributes of samples . . . . .	55
3.4. Componentry of bulk samples . . . . .	58
3.5. Physical data by stratigraphic layer for 2 pits . . . . .	61
3.6. Density and mass distribution for different layers from pit KT-10a . . . . .	52
3.7. Pictures of internal and external texture . . . . .	65
3.8. Conduit model of the 640 CE Big Obsidian eruption . . . . .	70
4.1 Pyroclast bulk porosity distribution . . . . .	77
4.2. CT images of Cascade Volcano pumices . . . . .	79
4.3. Particle size distributions of protopyroclasts . . . . .	81
4.4. Diagram illustrating primary and secondary fragmentation . . . . .	86

LIST OF TABLES

Table	Page
3.1. Physical attributes of juvenile products of the Big Obsidian period . . . . .	64

## CHAPTER I

### INTRODUCTION

Highly-silicic volcanic eruptions present a variety of geohazards that threaten human life and livelihood. As of 2015, more than 8% of the world's population lives within 100 km of a volcano that had significantly erupted at least once. While >14% of the world lives within 100 km of a volcano that has erupted during the Holocene (Freire et al., 2019), volcanic eruptions have even farther-reaching consequences. Tephra from these eruptions can encircle the globe, disrupting climate and aviation, and damaging infrastructure and crop yields (Wilson et al., 2014). To determine how past eruptions transpired, and thus how future ones may proceed, study of these volcanoes, particularly their resulting products, is imperative.

Pyroclasts, cooled blebs of once-molten magma, preserve textures largely inherited from magma's ascent to the surface (Shea et al., 2010). By reading, quantifying, and interpreting these textures, pyroclasts can offer a window into the conduit. As magma rises from the reservoir through the conduit, volatiles initially dissolved within the magma exsolve (e.g. H<sub>2</sub>O, CO<sub>2</sub>), leading to the nucleation and growth of bubbles of supercritical fluid (Gonnermann and Manga, 2007). As volatile solubility decreases at lower pressures (Newman and Lowenstern, 2002; Liu et al., 2015; Zhang et al., 2007), a positive feedback loop ensues: as the magma becomes progressively less dense, it rises faster, further driving bubble nucleation and growth (Sparks, 1978). The melt depletes of water and other volatiles, and overpressure builds as bubble expansion is restricted by an increasingly viscous melt (Gonnermann and Manga, 2013). When bubble overpressure exceeds the tensile strength of the melt by ~2-3 MPa (Alidibirov, 1994; Zhang, 1999;

Spieler et al., 2004; Mueller et al., 2008), the foamy magma catastrophically fragments into molten blebs that egress the volcano in an expanding gas phase (Dingwell, 1996; Papale, 1999; Gonnermann and Manga, 2007). These blebs cool to form solid pyroclasts on which textural interpretations are made (Shea et al., 2010).

Whether an eruption progresses explosively depends thus on timescales of competing factors, namely those of ascent, degassing, and outgassing (Gonnermann and Manga, 2007). If ascent is sufficiently slow and gas can efficiently escape the magma via permeable pathways (Gonnermann and Manga, 2003; Tuffen and Dingwell, 2005; Rust et al., 2004), then overpressure builds slowly and fragmentation may be avoided (Eichelberger et al., 1986; Westrich and Eichelberger, 1994). Thus, magma instead erupts as a flow/dome. If gas remains trapped or is unable to exit the magma during rapid ascent, fragmentation ensues (Wilson et al., 1980). Such is a classical physical model of how Plinian volcanic eruptions proceed. These eruptions produce largely stable eruptive column tens of kilometers high (Woods, 2013) and deposits dominated by pumiceous products that reach thousands of square kilometers in the case of large eruptions (e.g. climactic eruption of 5670 B.C. eruption Mt. Mazama; Bacon, 1983; Young, 1990).

Different styles of eruptions, such as Vulcanian eruptions, can explosively erupt following sudden decompression of stagnant, bubbly magma when sudden removal of overlying material depressurizes the system (Druitt et al., 2002; Wright et al., 2007; Clarke et al., 2007). These eruptions tend to be more limited in scale as compared to Plinian eruptions, but produce similar eruptive products (Kennedy et al., 2005; Giachetti et al., 2010) and thus associated hazards. Stromboli Volcano, known for its milder punctuated Strombolian eruptions, periodically produces much stronger Vulcanian events

(e.g. August 2019 eruption). These eruptions are accompanied by pyroclastic flows and kilometers-high eruptive columns with ballistic material (Giordano and Astis, 2020).

Other factors, such as the presence of meteoric water, forces explosive behavior, leading to phreatomagmatic eruptions (Self and Sparks, 1978; Sheridan and Wohletz, 1983; White and Houghton, 2000). Even less silicic to mafic endmembers can exhibit explosive behavior provided sufficiently rapid magma ascent (e.g. basaltic Plinian eruption of the San Antonio Tephra, Masaya Caldera, Nicaragua, Pérez et al., 2020; weak to sub-Plinian basaltic eruptions at Halema 'uma 'u crater, Kilauea volcano, U.S.A.; Rahimi, 2017; see also Moitra et al., 2013).

As explosivity spans the gamut of volcano and eruption type, constraining associated geohazards and particularly their duration is becoming ever important in a populating world. In this vein, recent work has heavily focused on the explosive-effusive transition in volcanic eruptions with particular attention to more silicic endmembers. The onset of effusive behavior (i.e. a lava flow) has often heralded the end of explosive activity (Eichelberger and Westrich, 1981; Woods and Koyaguchi, 1994; Scandone et al., 2007; Cassidy et al., 2018; Wadsworth et al., 2020), although concurrent behavior is possible (e.g. 2011 of Cordon Caulle, Chile; Schipper et al., 2013), as well as transitions from effusive to explosive behavior (e.g. explosions following dome growth, Pinatubo, Philippines, 1991; Pallister et al., 1992). To date, numerous studies have examined, among other characteristics, magma decompression rate (Castro et al., 2008; Alidibirov and Dingwell, 1996), crystal/bubble content (Mueller et al., 2008; Pistone et al., 2015; Parmigiani et al., 2017), conduit geometry (de' Michieli Vitturi et al., 2008), external assimilates (Austin-Erickson et al., 2008), crustal properties (Jaupart and Allègre, 1991;

Kennedy et al., 2010), and tectonic regime/stress field (Pinel and Jaupart, 2000; Scandone et al., 2007) as modulators of eruption style. However, with the potential for myriad feedback loops (e.g., Tait et al., 1989; Cassidy et al., 2018), precisely characterizing eruptive behavior seems an enigmatically complex process.

Still, despite the triggers and dynamics of volcanic eruptions being myriad and varied, eruption models often hinge on a common assumption – that pyroclasts serve as representative snapshots of conduit conditions. Analyses (e.g., Polacci et al., 2006; Mueller et al., 2011; Schipper et al., 2013; Rotella et al., 2014), experiments (Martel et al., 2003; Spieler et al., 2004; Toramaru, 2006; Hamada et al., 2010; Brugger and Hammer, 2010), and computational models (Melnik and Sparks, 2002; Gonnermann and Manga, 2007; Schwaiger et al., 2012) incorporate or verify results using data gleaned from a subset of pyroclasts from a given eruption. Pyroclasts' characteristics are largely assumed to be acquired near fragmentation and thus to preserve the final state of the magma (Shea et al., 2010; Rust and Cashman, 2011).

But how representative are these pyroclasts? How representative are the methodologies we use to assess their properties? What are studies missing that examine a limited size fraction of a component (i.e. ash or lapilli) or only one component at all (i.e. obsidian or pumice)? How might such patchwork approaches to studying volcanic material impact interpretations of the conduit and of numerical models of ash dispersion?

To answer these questions, I leverage mass quantities of data to examine conduit processes for multiple eruptions at Cascade Volcanoes. Several high and very high threat volcanoes – so named by the USGS based on their danger to human life in the event of an eruption - comprise the Cascade Volcanic Arc in the Pacific Northwest. In my second

chapter, I focus individually on the 1060 C.E. Glass Mountain eruption of Medicine Lake Volcano (high threat; Ewert et al. 2018), and focus on spacial heterogeneities in the conduit. In the third chapter, I examine spacial and temporal variations in conduit processes for the 640 C.E. eruption of Newberry Volcano (very high threat; Ewert et al. 2018). In the fourth chapter, I and co-authors examine common traits among rhyolitic pyroclasts, leveraging data from the two aforementioned eruptions along with those of the 5670 B.C.E. Cleetwood and climactic eruptions of Mt. Mazama (very high threat; Young, 1990; Bacon, 1983; Ewert et al., 2018).

In **Chapter II**, I investigate the relationships between the size, shape, density and texture of thousands of juvenile pyroclasts from the Plinian phase of the 1060 CE Glass Mountain eruption of Medicine Lake Volcano (California, USA; Heiken, 1978; Donnelly-Nolan et al., 2007). Analyzed pyroclasts, which originate from representative beds of both proximal and medial deposits, range from 0.125 mm to several centimeters in diameter. I show that the size, shape, density and texture of juvenile Plinian pyroclasts are intimately interrelated: as the size of pyroclast decreases from 64 mm to 0.125 mm, their shape shifts from equant to tabular to elongate. Moreover, while rounded vesicles dominate the largest clasts, elongate and distorted vesicles become progressively more present with decreasing clast size. Concurrently, clast density continually increases in a sigmoidal way from  $\sim 0.4 \text{ g.cm}^{-3}$  (>80% porous) in the largest clasts to  $\sim 1.7\text{--}1.9 \text{ gcm}^{-3}$  (20–30% porous) by 0.125 mm. These observations are identical for both the proximal and medial locations. I also show that expansion, compaction and secondary fragmentation did not significantly change the texture of juvenile pyroclasts after fragmentation.



The size dependency of density and texture of Plinian pyroclasts is instead interpreted to originate from the lateral position of the magma in the conduit prior to fragmentation: smaller clasts result from higher shearing closer to conduit walls, where greater shear stresses increasingly elongate vesicles and fragment particles in smaller pieces. Moreover, ~5% of pyroclasts 1–8 mm in size are likely agglomerates of mono-texture ash particles that sintered within the conduit during or shortly after primary fragmentation. This work shows that future studies should analyze the full spectrum of clast sizes, from the micron-to centimeter-scale, to fully capture the complexity and breadth of eruptive processes across the volcanic conduit.

In **Chapter III**, I examine the 640 C.E. rhyolitic eruption of Newberry Volcano (OR, USA), which began with sub-Plinian pyroclastic fallout and terminated effusively with an obsidian flow (Kuehn, 2002; Rust and Cashman, 2007). I combine previous work on the geochemistry and textures of obsidian pyroclasts with new detailed physical and textural analyses of the pumiceous products, using juvenile products to understand eruption dynamics throughout the shallow conduit. I examine thousands of pumices for external texture, density, and mass distribution, pulling samples from 37 layers spanning 4 pits along the dispersal axis of the fallout deposit. Ultimately, transitory Vulcanian-like pulses are the link between Subplinian and effusive activity.

In **Chapter IV**, I and co-authors evaluate juvenile porous lapilli from four volcanic eruptions from the the Cascades, including the two aforementioned as well as the 5670 B.C.E. Cleetwood and climactic eruptions of Mt. Mazama (Young, 1990; Bacon, 1983). Textural observations of these sub-Plinian and Plinian pumice lapilli reveal that some primary products of magma fragmentation survive by agglomerating and

sintering together within seconds of magma break-up. Their size distributions reflect the energetics of fragmentation, consistent with products of rapid decompression experiments. We find that pumice aggregates thus offer a unique window into the previously inaccessible primary fragmentation process.

## CHAPTER II

### THE MORPHOLOGY AND TEXTURE OF PLINIAN PYROCLASTS REFLECT THEIR LATERAL SOURCING IN THE CONDUIT

This chapter was published in *Earth and Planetary Sciences letters* under the title “The morphology and texture of Plinian pyroclasts reflect their lateral sourcing in the conduit.” This publication was co-authored with T. Giachetti. K.R. Trafton conceived the study, gathered and curated the data, analyzed and interpreted the data, acquired funding, and wrote the paper. T. Giachetti helped in conceiving the study, as well as with data analysis interpretation, funding acquisition, and paper revisions. Both co-authors extensively discussed ideas to ameliorate the final product.

#### **1. Introduction**

During magma’s ascent towards the Earth’s surface, dissolved volatiles exsolve via the nucleation of vapor bubbles. Multiple populations of micron- to millimeter-scale bubbles can result as bubbles variably grow (Klug et al., 2002; Polacci et al., 2003; Lautze and Houghton, 2007) and coalesce (Adams et al., 2006; Gurioli et al., 2008; Giachetti et al., 2010) during cycles of ascent and stagnation. At a given depth, higher shear stress near conduit margins stretches bubbles and may promote coalescence, resulting in elongated and/or polylobate vesicles (Polacci et al., 2001, 2003; Klug et al., 2002; Rust et al., 2003).

If magma ascends rapidly, it can fragment into discrete, bubbly parcels that are carried upwards in an expanding gas phase (Gonnermann, 2015). A mixture of gas and these bubbly fragments, called pyroclasts, then egresses the volcano in an explosive eruption. A variety of patently dangerous volcanic hazards are associated with the

ensuing tephra fallout from the eruptive column (Costa et al., 2009; Bonasia et al., 2011; Macedonio et al., 2016) and/or pyroclastic density currents (e.g., Mueller et al., 2015; and references therein). Pyroclasts record a complex history of conduit processes; their morphology and internal texture can provide a snapshot of conditions near the point of magma fragmentation, provided post-fragmentation alteration of morphology and texture is minimal or can be accounted for (Shea et al., 2010; Giachetti et al., 2010; Rust and Cashman, 2011).

Lapilli 1.6-3.2 cm in diameter are commonly examined to glean insight into conduit dynamics; they are thought to undergo minimal textural alteration following fragmentation. Density is relatively constant in this size range and evaluation of 100-200 1.6-3.2-cm lapilli for a given eruption reveals standard deviations of 10-20% about the mean (e.g., Houghton and Wilson, 1989; Gardner et al., 1996; Manville et al., 2002; Polacci et al., 2003; Shea et al., 2010; Hiroi and Miyamoto, 2016; Mitchell et al., 2018). Lapilli >3.2 cm may undergo post-fragmentation expansion, during which bubbles expand in a still-molten interior as pyroclasts continue to decompress in the eruption column (Gardner et al., 1996; Kaminski and Jaupart, 1997; Mitchell et al., 2018). At the millimeter scale and smaller, interpretations may be biased by introduction of chips of highly vesicular pyroclasts resulting from secondary fragmentation (Kueppers et al., 2012). In high-energy collisional regimes such as those in the conduit, particles preferentially break into fragments that are large fractions of their initial size, and rounding is minimal (Dufek et al., 2012). In pyroclastic density currents, low-energy collisions among grains abrade and round lapilli (Dufek and Manga, 2008; Manga et al.,

2011; Dufek et al., 2012; Kueppers et al., 2012; Jones et al., 2017), saturating the fine ash size fraction with larger pyroclasts' broken bubble walls and septa (Mueller et al., 2015).

To date, textural studies have largely focused on endmember size fractions, whether 1.6-3.2 cm lapilli (e.g., Whitham and Sparks, 1986; Houghton and Wilson, 1989; Klug and Cashman, 1994; Gardner et al., 1996; Polacci et al., 2001; Mitchell et al., 2018) or micron-scale ash (e.g., Walker, 1980; Wright et al., 2012; Cannata et al., 2014). As a result, these studies also examine particle morphology on those same scales. Brittle fragmentation of silicic magma creates blocky, angular lapilli with planar and curvilinear sides (e.g., Alidibirov and Dingwell, 1996; Dufek et al., 2012). At the submillimeter scale, ash particles from explosive eruptions can fragment into plate-like, elongate, jagged particles (e.g., Polacci et al., 2003; Liu et al., 2015; Saxby et al., 2020). Some ash deposits have been reported to be highly concentrated in elongated pumiceous particles, so-called "stick pumices" or "needles" (Rosi et al., 1999; Larsen et al., 2001; Polacci et al., 2003; Saxby et al., 2020), but the reason for which has yet to be fully examined. Additionally, whether a continuum exists between the two morphologies characteristic of lapilli and ash, or at what size fraction one morphology begins to dominate, has yet to be determined. If, as some studies have suggested, a relationship exists between bubble and pyroclast shape (e.g., stick pumices preserving elongated vesicles; Palladino and Taddeucci, 1998), what might a coupled textural-morphological investigation of pyroclasts from the micron to centimeter scale reveal? In order to aptly characterize the breadth of conduit processes, a thorough investigation of pyroclasts' characteristics spanning the size spectrum is necessary.

Beyond contextualizing conduit processes, study of variations in pyroclasts' characteristics with size is essential to tephra dispersion models that are used to predict fallout and ultimately assess future geohazards (e.g., Bonadonna and Phillips, 2003; Pfeiffer et al., 2005; Barsotti and Neri, 2008). The size, density, and shape of pyroclasts largely control their terminal velocity, and thereby determine for how long particles remain airborne and where they land (Walker et al., 1971; Riley et al., 2003; Bagheri and Bonadonna, 2016; Saxby et al., 2020). However, current models use single values of density from ash to lapilli for a given magma composition (e.g., Taddeucci et al. 2002; Folch et al. 2008) or simplified log-linear relationships between average density and particle diameter,  $d$ , for pyroclasts  $8 \mu\text{m} < d < 2 \text{ mm}$  (Bonadonna and Phillips, 2003). Below  $8 \mu\text{m}$ , ash is considered the density of glass ( $2.3\text{-}2.6 \text{ g cm}^{-3}$ , depending on magma composition), whereas pyroclasts are considered 70-80% porous above  $2 \text{ mm}$  (e.g., Bonadonna and Phillips, 2003). Total grain size distribution models also resort to constant values of density (Pioli et al., 2019) or log-linear models (Rust and Cashman, 2011) to avoid introducing artificial kinks via an uncalibrated size-density trend. These assumptions result from a paucity of quantitative data for particle shape, despite shape-dependent drag equations producing more accurate results than spherical approximations (Ganser, 1993; Bagheri and Bonadonna, 2016; Dioguardi et al., 2018). For example, Saxby et al. (2018) report a 44% increase in travel distance for  $100 \mu\text{m}$  particles modelled as non-spherical (sphericity = 0.5) versus spherical counterparts. In order to accurately predict where pyroclasts and ash will fall and assess associated hazards, proper calibration of these models requires ground-truthed data.

Eychenne and Le Pennec (2012) evaluated changes in pyroclast density as a function of their size for the 2006 subplinian basaltic eruption of Tungurahua volcano, Ecuador. They report a sigmoidal relationship between the density of scoria and their diameter, wherein density increases  $1.5\times$  as particles decrease in size from 23 mm to 0.09 mm. Whether highly silicic pumices exhibit the same trend across such a size spectrum has yet to be thoroughly examined. To the best of our knowledge, only Manville et al. (2002) have reported a continuous density spectrum of highly-silicic pyroclasts ranging in size from ash to lapilli: they describe an increase in the mean density of pumice clasts from the 1800a Taupo ignimbrite (New Zealand) from  $0.5 \text{ g cm}^{-3}$  to  $1.2 \text{ g cm}^{-3}$  ( $\sim 80\%$  to  $50\%$  porosity) as particles decrease in size from 16 mm to 0.125 mm.

In this study, we examine whether pyroclasts' shape, texture, and density are systematically a function of their size. We measure the volume and mass of  $>3,500$  individual particles 0.125-64 mm in diameter to provide robust density measurements of juvenile pumiceous pyroclasts from a proximal and medial pit from the 1060 CE eruption of Medicine Lake Volcano, CA. We then quantify variations in external clast morphology and compare it with internal textures to determine whether and what pre-, syn- or post-fragmentation processes control clast texture. We finally contextualize our findings with previous studies' conduit models to discuss implications for tephra dispersion models.

## **2. Background**

The  $1060 \pm 90$  CE Glass Mountain eruption of Medicine Lake Volcano (CA) began with a Plinian phase that deposited  $0.27 \text{ km}^3$  of rhyolitic pyroclastic material and terminated effusively with rhyolitic and dacitic flows totaling  $\sim 0.7 \text{ km}^3$  (Heiken, 1978;

Donnelly-Nolan et al., 2007). The explosive phase is solely fallout (Heiken, 1978; Nathenson et al., 2007) with no reported deposits of pyroclastic density currents. Due to dominant winds, most of the tephra were deposited east-northeast of the vent, forming an irregular ellipse (Heiken, 1978). Glass Mountain pyroclasts are rhyolitic (74% SiO<sub>2</sub>, 14% Al<sub>2</sub>O<sub>3</sub>, 4% K<sub>2</sub>O, <10% other), and the major element chemistry does not significantly change over time, regardless of clast morphology and size (Heiken, 1978). Pyroclasts are crystal-poor to crystal-free, containing only trace phenocrysts of plagioclase and orthopyroxene (Heiken, 1978; Stevenson et al., 1996). Lithic fragments include basalt and andesite that comprise up to a third of a given deposit bed (Heiken, 1978). The density of Glass Mountain glass is  $2.36 \pm 0.05 \text{ g.cm}^{-3}$  (Giachetti et al., 2020).

Heiken (1978) examined the Glass Mountain tephra deposits at multiple outcrops, including a 3.7-m-thick pit 2.8 km east of the vent that comprises eleven tephra beds. He also described the tephra deposit at distances of 3-11 km east, 3-11 km north, and 1-3 km south and west of the vent, and found 2-3 tephra beds at each locality having combined thicknesses of 22-131 cm. Heiken noted the remarkable uniformity of the Glass Mountain tephra in that all deposits consist of reversely graded or massive beds of grey medium-sized-ash to lapilli-sized tephra. New field investigations of more than seventy pits ~2-15 km of the vent in all directions, including a 14-m-thick section 1.8 km northeast of the vent, corroborate these observations (Giachetti and Shea, in prep). Heiken (1978) sieved particles from each of the 11 beds (units) of his 3.7 m-thick pit, compared the results with those from a section located 5-6 km NNE of Glass Mountain, and found no systematic changes in grain-size characteristics from unit to unit (Table 4 of Heiken, 1978). All beds at a given locality are similar in terms of particle median size and contain poorly-sorted



lapilli, though those farther from the vent are more finely grained in medium to coarse ash-sized particles. Heiken (1978) also studied clast and vesicle shapes, density, and componentry for sizes 2-16 mm and concluded that pumiceous pyroclasts for a given clast size among all beds of the 3.7 m-thick pit are “remarkably homogeneous in their composition and morphology.” He reports that lapilli across all size fractions and in all beds are equant to slightly elongate, blocky fragments that, on average, have length to width ratios of 1.4-1.6. They have sharp and angular surfaces and ovoid to elongate vesicles 5-90  $\mu\text{m}$  wide and 20-700  $\mu\text{m}$  long.

### **3. Methodology**

The next sections detail the different methods and instruments used to gather pyroclast and vesicle characteristics from two sampled locations. We evaluated the density, shape, and size of clasts, and the shape and size of vesicles for clasts 0.125-64 mm approximately every 1  $\phi$  (henceforth called size fractions), where  $\phi = -\log_2(d)$  and  $d$  is expressed in mm. We encourage the reader to follow the methodological flow chart found in Appendix A (Fig. A.1).

#### *3.1. Sampling and preparation*

We collected samples from two pits, one proximal and one medial (Fig. A.2). The proximal sample was collected in a quarry 1.9 km NNE of the summit of Glass Mountain, from a 30 cm-thick bed situated ~60 cm below the top of the Glass Mountain tephra deposit (Fig. A.2). The sampled bed is reversely graded and poorly sorted, similar to the proximal beds examined by Heiken (1978). Although the base of the Glass Mountain tephra deposit was not reachable at that site, the outcrop is located just 300 m

downwind of a 14 m-thick outcrop excavated in the same quarry that exhibits the complete Glass Mountain deposit (Giachetti and Shea, unpublished data). We thus believe that the full Glass Mountain tephra deposit must be on the order of 10 m where we collected the proximal sample. We sampled the entire 30 cm-thick bed in bulk and collected additional lapilli in the same bed to have a statistically significant amount available for textural investigation. The medial sample was collected 9.2 km NNW of the summit of Glass Mountain (Fig. A.2). The deposit at this site appears as a single reversely-graded 12 cm in thickness. This bed was sampled in its entirety. Bedding, sorting, and morphology and texture of the lapilli from these two pits are qualitatively comparable to other lapilli from multiple beds and pits surrounding Glass Mountain (Heiken, 1978; Giachetti and Shea, in prep). As such, we believe our samples herein are representative of the overall fallout deposit. Quantitative characterization of clast and vesicle shape and size further support this assertion (see Sections 4.3 and 4.4).

Clasts were dry sieved approximately every 1  $\phi$  for  $-6 < \phi < 4$  (i.e.,  $0.063 \text{ mm} < d < 64 \text{ mm}$ ; Eychenne et al., 2012), washed, and dried overnight in a furnace at  $100^\circ\text{C}$ . They were then sorted into four categories: pumice, obsidian, lithics, and free crystals, with the naked eye for those  $>8 \text{ mm}$  and via microscope for clasts  $<8 \text{ mm}$  (Table B.2). The texture and morphology of the pumiceous pyroclasts were then assessed for particles  $>0.125 \text{ mm}$  (Fig. 1,  $>3500$  particles in total).

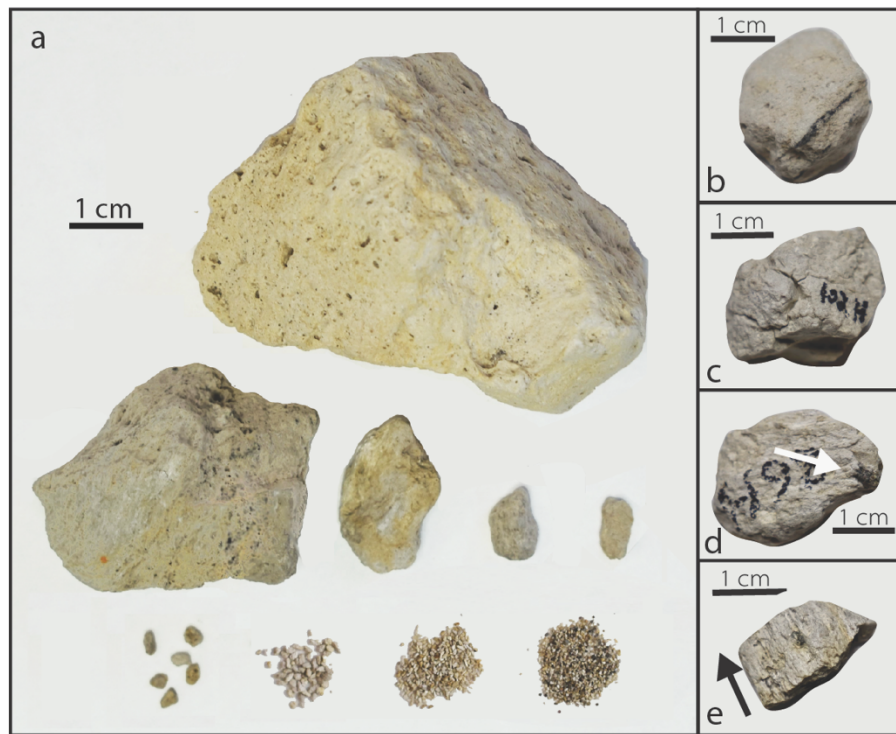


Figure 1: a) Homogeneous clasts from the Glass Mountain eruption of Medicine Lake Volcano spanning  $0.125 < d < 64$  mm from each phi size fraction measured. The bottom right hand pile is an example of a bulk sample (i.e., all components) spanning  $0.125 \text{ mm} < d < 0.25 \text{ mm}$ . Right-hand photos are heterogeneous clasts exhibiting b) obsidian banding, c) breadcrusting, d) crystals, and e) elongate/tubular vesicles.

### 3.2. Homogeneous vs. heterogeneous pumices

Clasts  $>8$  mm were defined as homogeneous or heterogeneous based on their outward textural appearance (Fig. 1). Clasts exhibiting obviously elongated vesicles, alternate banding of pumice- and obsidian-like textures, crystals, or breadcrusting were considered heterogeneous. All others were considered homogeneous. Clasts with sharp edges with an undulatory rather than smooth surface were considered broken during transport and not included in analyses (Mitchell et al., 2018); these clasts comprise  $\sim 3\%$

of proximal clasts and were not present in the medial sample given the paucity of larger lapilli.

### 3.3. Density

For clasts >8 mm, density was calculated using individual mass and volume measurements (density = mass/volume) of singular clasts. Volume was determined via classical immersion method (Houghton and Wilson, 1989; Fig. A.3a) or dynamic image analyzer (Microtrac PartAn<sup>3D</sup>; Fig. A.3b) and mass was obtained using a high-precision balance. For pumiceous particles 0.125-8 mm, density was calculated for every size fraction: the volume of 45-250 clasts was measured using the PartAn<sup>3D</sup> (Fig. A.3b) and at least 100 particles were weighed, giving an average particle volume and average particle mass that were then used to calculate the average density of the corresponding size fraction. Particles 0.063-0.125 mm were mounted in epoxy pucks and porosity was estimated from Scanning Electron Microscope (SEM) images. We report and plot data in terms of both density and porosity, and similarly report size in terms of diameter ( $d$ ), volume ( $V$ ), and phi size ( $\phi$ ). Clast porosity,  $\alpha$  in %, is given by

$$\alpha = \frac{M}{\rho V} \times 100, \quad \text{Eq. (1)}$$

where  $M$  is the mass of a particle,  $V$  its volume,  $\rho = 2.36 \pm 0.05 \text{ g cm}^{-3}$  (Giachetti et al., 2020) is the density of the solid phase, and assuming a density of air of  $0 \text{ g cm}^{-3}$ .

### 3.4 Clast shape

Qualitative clast shape was determined via assessment of hand samples (>500 4-64 mm clasts) or using SEM images of cross-sections (>200 0.125-4 mm clasts)

following Blott and Pye (2008): equant clasts are those with approximately equal dimensions; tabular clasts are plate-like, exhibiting one slightly shorter dimension; and elongate clasts are rod-like, having a distinctly long axis. Clast shape was then quantified in hand sample using high precision calipers or a particle size analyzer (Microtrac PartAn<sup>3D</sup>; Fig. A.3b) for batches of 45-250 clasts 0.125-64 mm. We measured the longest ( $l$ ) and shortest ( $b$ ) axes of these clasts to calculate clast elongation,  $D_c = (l-b)/(l+b)$ .

### *3.5 Vesicle shape and size distributions*

Thin sections were made on five proximal clasts >8 mm that have a porosity within 3% of the median porosity for their size fraction. Several to tens of 0.125-8 mm clasts from both pits were mounted in epoxy every size fraction. Pucks and thin sections were carbon coated for imaging on a Quanta 1000 Scanning Electron Microscope (SEM) and images were taken at multiple magnifications towards both the rim and core of each clast.

Images were then binarized using the Fiji (ImageJ) image processing package and analyzed using FOAMS (Shea et al., 2010). Percent area of a given image as occupied by elongate, rounded, or distorted vesicles was evaluated spanning sieved size fractions. Data from clasts >8 mm were amalgamated and considered as one size fraction for this step only in order to make a more robust data set. Seven to fifty clasts were evaluated per size fraction. Vesicle shape was then quantitatively assessed for each size fraction using a single representative clast (no breadcrusting, obsidian banding, nor large crystals, and with proportions of rounded, elongate, and distorted bubbles within the standard deviation of the median for all clasts in that size fraction).

Vesicles cut by the edge of the image and those smaller than 20 px<sup>2</sup> were excluded from analysis, resulting in 150-1,750 vesicles analyzed per pumice. For statistical representativity, the largest vesicle measured had an area smaller than 1/5<sup>th</sup> of that of the image (Shea et al., 2010). We analyzed vesicles ~1-100 μm in diameter in nine pyroclasts spanning all evaluated size fractions. Circularity,  $C$ , was calculated as:

$$C = \frac{4\pi A}{P^2} \quad \text{Eq. (2)}$$

where  $A$  is area and  $P$  is perimeter, and varies between 0 and 1 (disc). Circularity was chosen to quantify vesicle shape given the complexity and variety of vesicle shapes in this analysis, as circularity quantifies both form and roughness (Shea et al., 2010; Liu et al., 2015). Because low pixel count can artificially inflate the roughness of analyzed objects, images with similar pixel densities were used (~1-3 pixels/μm). We also report vesicle elongation (Rust et al., 2003), elsewhere referred to as deformation (Dingwell et al., 2016), via the dimensionless parameter,  $D_v$ :

$$D_v = \frac{l-b}{l+b} \quad \text{Eq. (3)}$$

where  $l$  and  $b$  are respectively the semi-major and semi-minor axes of the sheared vesicle. Higher values of  $D_v$  correspond to a more elongated shape. Finally, we quantified vesicle orientation using the angle function in ImageJ, which calculates the angle between the main axis of a given shape and a line parallel to the x-axis of the image.

To assess the viability of post-fragmentation expansion, we analyzed vesicle shape and size distribution (VSD) of both the rim and the core of three proximal lapilli. Analyzed clasts span about 1.5 orders of magnitude in volume and were chosen so that their porosity is within 3% of the median for that size fraction (Table B.1). Two to five SEM images of varying magnifications were used for a given location within each clast

(rim or core) depending on qualitative assessment of the range in vesicle sizes. At least 120 vesicles per magnification were evaluated, resulting in 122-927 vesicles analyzed per size distribution.

#### **4. Results**

In the subsequent paragraphs, we describe changes in pyroclasts' characteristics as a function of their size for both proximal and medial pits. We first describe variations in componentry of the sample and external texture and morphology of the clasts, before detailing changes in their internal texture and density/porosity. Throughout, subscripts "p" and "m" refer to the proximal and medial samples, respectively.

##### *4.1 Componentry*

Estimates from the field indicate that pumice comprises >90% of >32 mm clasts. For both pits, obsidian content never exceeds 20% for any given size fraction, and free crystals average ~10% of a size fraction on the submillimeter scale (Table B.2). In the proximal sample, lithic content reaches a maximum of ~30% for the size fraction 0.85-2 mm and decreases at both larger and smaller size fractions. Pumice content inversely mirrors this trend, being greatest at endmember size fractions (~90% for 0.063-0.09 mm; ~98% for 16-32 mm). In the medial sample, pumice content gradually decreases from 100% to ~50% as clast size decreases from 32 mm to 0.063 mm, whereas obsidian, lithic, and free crystal content increase (Table B.2).

#### 4.2 External texture

No proximal pumices >48 mm in diameter exhibit surface heterogeneities (i.e., crystals, obsidian banding, breadcrusting, or elongated vesicles; Fig. 1). For clasts 8-48 mm, >75% of the proximal lapilli and all medial clasts lack breadcrusting, obsidian banding, and external crystals. Obsidian-banding and breadcrusting are respectively exhibited by <5% and <15% of the proximal lapilli. Obsidian-banding is the predominant feature for only 2 proximal lapilli, and only one proximal lapillus contains breadcrusting pervasive enough to classify it as the predominant heterogeneity. Crystals are a transitory feature: no clasts exhibit crystals as a predominant heterogeneity, though ~25% of proximal lapilli sampled exhibit at least one sub-mm to mm-scale crystal on their surface.

In general, pumices most commonly exhibit elongated/tubular vesicles as a heterogeneity, especially small clasts: as clast size decreases from 64 mm to 0.125 mm, the percent of clasts exhibiting predominantly elongate vesicles increases from 14% to >70% (Fig. 2). The same trend is observed in the medial sample: the proportion of clasts with elongated/tubular vesicles increases from ~30% for clasts >8mm to ~80% for clasts 0.125-0.25 mm.

#### 4.3 External morphology

For both pits, clast shape changes from equant to elongate as clast diameter decreases from 64 mm to 0.125 mm (Fig. 3; Fig. B.1). Pyroclasts are predominantly equant for 8-64 mm ( $D_{cp} = 0.29 \pm 0.09$ ;  $D_{cm} = 0.32 \pm 0.09$ ), become largely tabular for 0.5-8 mm ( $D_{cp} = 0.32 \pm 0.09$ ;  $D_{cm} = 0.35 \pm 0.1$ ), and are tabular to elongate for 0.125-0.5 mm ( $D_{cp} = 0.38 \pm 0.09$ ;  $D_{cm} = 0.39 \pm 0.1$ ; Fig. B.1).



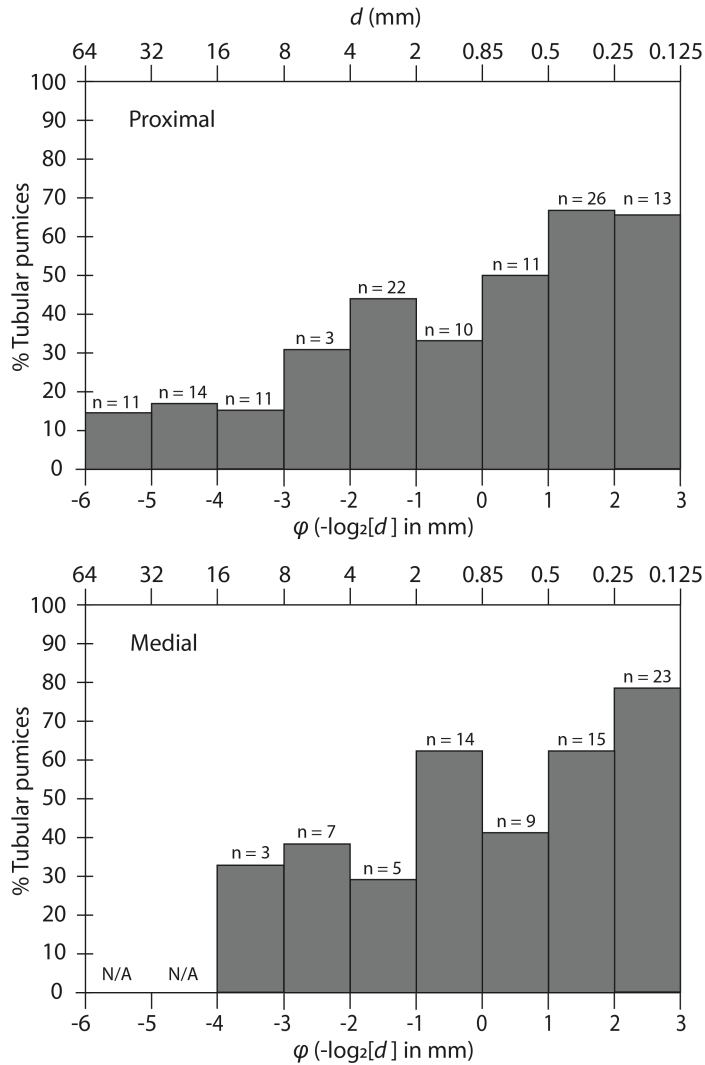


Figure 2: Percent of tubular pumices (pumices predominated by elongated/tubular vesicles) out of all pumices for a given size fraction.  $n$  = number of tubular pumices as based entirely on SEM images for the medial pit. For the proximal pit, hand samples were evaluated for clasts 4 mm and larger, and SEM images used for smaller clasts. SEM images were used to ensure that clasts are both elongated in shape and contain elongated vesicles, thereby classifying them as tubular pumices.

#### 4.4 Internal texture

##### 4.4.1 Vesicle shape and size distributions

As clast size decreases from 64 mm to 0.125 mm, the predominant internal texture shifts from rounded to elongate vesicles (Fig. 3). For both pits, the percent area of clasts occupied by rounded vesicles, as analyzed on SEM images, decreases from >50% to <20% as clast size decreases from 64 mm to 0.125 mm (Fig. 4). Conversely, percent area of elongate vesicles increases from <40% to >70% over the same range of clast sizes. Percent area of distorted vesicles is relatively constant at 10-20% for proximal pumices but reaches 35-40% for medial pumices 0.85-4 mm in size. At both pits, clasts 0.125-0.50 mm exhibit predominantly elongate vesicles (Figs. 2, 3).

For both pits, vesicle shape parameters systematically vary with both vesicle size and clast size. Regardless of their size, vesicles are more circular, less elongate and have fewer contorted shapes in larger clasts than those in smaller clasts. As clast size decreases from 64 mm to 0.125 mm, median vesicle circularity,  $C$  significantly decreases from  $0.65 \pm 0.2$  to  $0.35 \pm 0.2$  (Figs. 3; 5a). Lapilli at both pits tend to have vesicles similarly elongated regardless of their size ( $D_v \sim 0.3 \pm 0.18$ ; Figs. 3; 5b, c), whereas vesicles in clasts <2 mm are more elongated, reaching a median  $D_v \sim 0.59 \pm 0.10$  in the smallest clast analyzed (Fig. 5b). These clasts also have larger vesicles that are more elongated than smaller ones (Fig. 5c). Finally, while vesicles in clasts >2 mm do not exhibit any obvious predominant direction of alignment, they are progressively more aligned in smaller clasts and ~60-70% of the vesicles are aligned within  $10^\circ$  of a main direction in the smallest clasts analyzed (Fig. 5d; Fig. B.2).

Vesicle sizes are largely between 0.01 – 1 mm, though smaller vesicles persist down to a few microns, particularly in smaller clasts. For the three clasts analyzed for vesicle size distributions (VSDs), both the VSD and porosity do not vary significantly from rim to center of a given clast (Fig. 6; Table B.1) and all size distributions are unimodal. The largest clast ( $d = 45$  mm) has a mean vesicle diameter of 0.1 mm, whereas the other two clasts ( $d = 23$  mm and 11 mm) have mean values of 0.03-0.05 mm. However, the two smaller clasts exhibit similar vesicle size distributions despite being half an order of magnitude different in volume, consistent with their porosity being similar (70-75%). The Gaussian shape of all vesicle size distributions further suggests that all three samples experienced a single nucleation event followed by vesicle growth (Fig. B.3; e.g., Shea et al., 2010).

#### 4.4.2 Density

The size-density distribution curve is overall sigmoidal for pumiceous pyroclasts from both pits (Fig. 6). The largest pumices 4-64 mm, comprising the tail of the sigmoid, evidence their own trend in both samples, wherein density increases from  $0.47 \pm 0.2$  to  $0.8 \pm 0.2$  g cm<sup>-3</sup> for the proximal pit, and from  $0.4 \pm 0.2$  to  $0.7 \pm 0.2$  g cm<sup>-3</sup> for the medial pit with decreasing clast size (Figs. 6; B.4). Between ~1 and 10 mm, density values plateau to 0.7-0.8 g cm<sup>-3</sup> (i.e., porosity of ~70%) in both samples. Between 0.125-1 mm, density more than doubles, increasing from 0.7 to 1.7 g cm<sup>-3</sup>. Finally, for  $d < 0.125$  mm, density plateaus at 1.7-1.8 g cm<sup>-3</sup> and smaller samples likely will remain somewhat porous until micron-scale bubbles no longer persist (Manville et al., 2002), at which point they become the density of rhyolitic glass (~2.36 g cm<sup>-3</sup>; Giachetti et al., 2020).

Such density variations are corroborated by microscope observations of pumice textures (Fig. 3).

Visually heterogeneous proximal lapilli (i.e., those exhibiting elongated vesicles, obsidian banding, crystals, or breadcrusting) as considered apart from homogeneous clasts, exhibit a similar trend overall in that they generally become denser with decreasing size, increasing from  $\sim 0.3 \pm 0.1 \text{ g cm}^{-3}$  to  $0.9 \pm 0.2 \text{ g cm}^{-3}$  (Figs. 6; B.4). We thus feel justified including these samples as part of the larger suite of pumices used in determining the size-density curve for the proximal pit (Fig. 8). The medial pit did not have lapilli with externally visible heterogeneities, though this could be due to lack of lapilli overall in the sample. When plotted together with visually homogeneous samples, proximal samples with crystals account for most of the scatter around the average, likely because the crystals are inherently denser than the surrounding pumice and may disrupt vesicle networks.

## 5. Discussion

Overall, clast morphology shifts from equant to tabular to elongate as clast size decreases from 64 mm to 0.125 mm. Moreover, as clast size decreases, the internal texture changes as well; clasts increasingly contain more domains of elongate and distorted vesicles, until only elongate or distorted vesicles entirely comprise clasts by 0.125 mm. This shift in internal texture is captured by an increase in density from 0.4-0.5 to 0.7-0.8  $\text{g cm}^{-3}$  for the proximal sample, and from  $0.4 \pm 0.2$  to  $0.7 \pm 0.2 \text{ g cm}^{-3}$  in the medial sample by 0.125 mm (Fig. 6), corresponding to a decrease in porosity from about 80% to 20-30%. Changes in external clast morphology and size are thus mirrored by


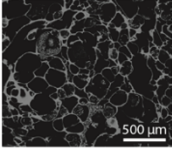

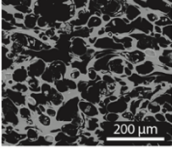

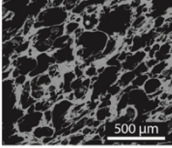

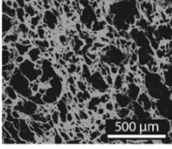

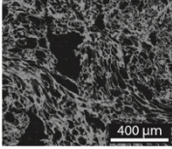

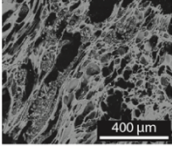
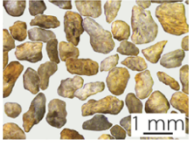
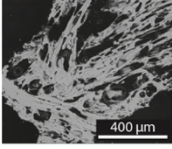
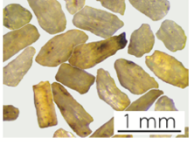
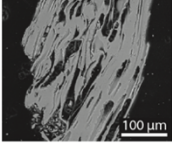
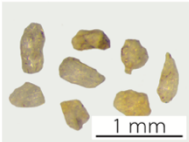
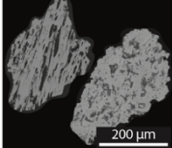
Size	Typical Clast Morphology	Dominant Clast Shape	Typical Internal Textures	Dominant Bubble Shape
32 - 64 mm $-6 < \phi < -5$		Equant $D_{cp} : 0.28 \pm 0.10$ $D_{cm} : \text{N/A}$		Rounded $D_{vp} : 0.30 \pm 0.19$ $D_{vm} : \text{N/A}$
16 - 32 mm $-5 < \phi < -4$		Equant $D_{cp} : 0.28 \pm 0.09$ $D_{cm} : 0.33 \pm 0.09$		Rounded $D_{vp} : 0.29 \pm 0.18$ $D_{vm} : 0.31 \pm 0.17$
8 - 16 mm $-4 < \phi < -3$		Equant to tabular $D_{cp} : 0.31 \pm 0.09$ $D_{cm} : 0.31 \pm 0.09$		Rounded to elongate $D_{vp} : 0.30 \pm 0.17$ $D_{vm} : 0.30 \pm 0.17$
4 - 8 mm $-2 < \phi < -3$		Tabular $D_{cp} : 0.32 \pm 0.09$ $D_{cm} : 0.36 \pm 0.11$		Elongate $D_{vp} : 0.31 \pm 0.18$ $D_{vm} : 0.30 \pm 0.17$
2 - 4 mm $-2 < \phi < -1$		Tabular $D_{cp} : 0.30 \pm 0.09$ $D_{cm} : 0.33 \pm 0.09$		Elongate $D_{vp} : 0.42 \pm 0.17$ $D_{vm} : 0.35 \pm 0.18$
0.85 - 2 mm $-1 < \phi < 0$		Tabular $D_{cp} : 0.33 \pm 0.1$ $D_{cm} : 0.32 \pm 0.1$		Elongate $D_{vp} : 0.45 \pm 0.17$ $D_{vm} : 0.46 \pm 0.20$
0.5 - 0.85 mm $0 < \phi < 1$		Tabular to elongate $D_{cp} : 0.35 \pm 0.1$ $D_{cm} : 0.38 \pm 0.1$		Elongate to distorted $D_{vp} : 0.48 \pm 0.16$ $D_{vm} : 0.55 \pm 0.22$
0.25 - 0.5 mm $1 < \phi < 2$		Elongate $D_{cp} : 0.32 \pm 0.09$ $D_{cm} : 0.42 \pm 0.09$		Elongate to distorted $D_{vp} : 0.64 \pm 0.20$ $D_{vm} : 0.57 \pm 0.17$
0.125 - 0.25 mm $2 < \phi < 3$		Elongate to tabular $D_{cp} : 0.44 \pm 0.1$ $D_{cm} : 0.37 \pm 0.1$		Elongate or distorted $D_{vp} : 0.58 \pm 0.19$ $D_{vm} : 0.59 \pm 0.20$

Figure 3: Clast shape ( $D_c$ : elongation, also referred to as the deformation index; Rust et al., 2003; Shea et al., 2010) and bubble shape ( $D_v$ : elongation) for every phi size analyzed. Pictures of typical clast morphologies and internal textures are shown. Subscripts ‘p’ and ‘m’ refer respectively to proximal and medial pits.

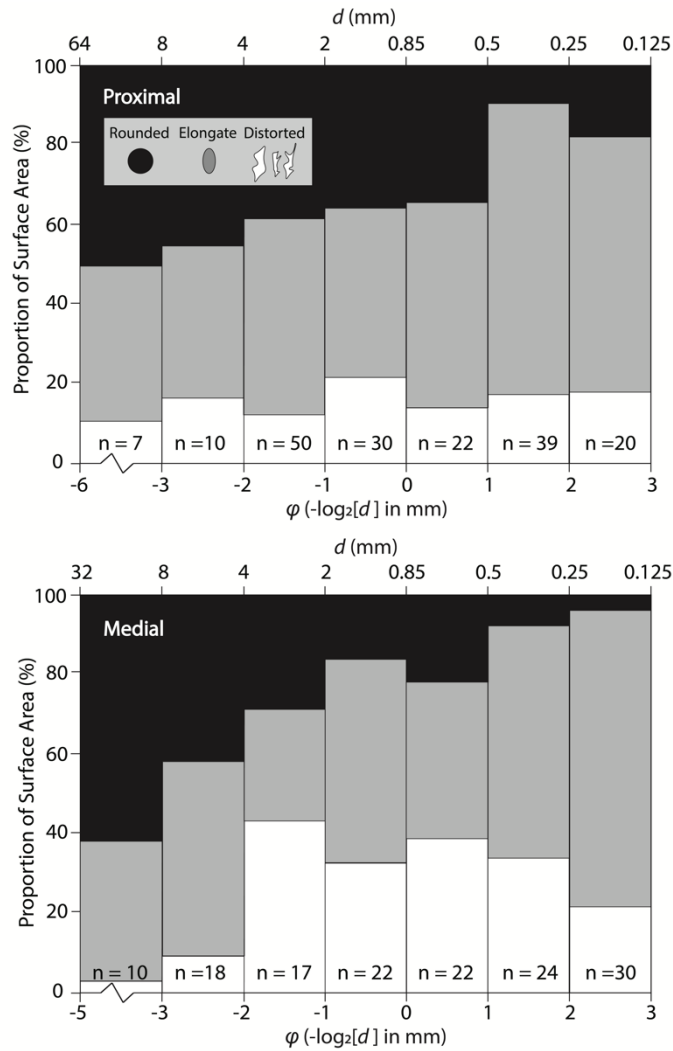


Figure 4: Percent texture by area of SEM images for every phi size analyzed. Vesicles were classified as rounded, elongate, or distorted. The number of images analyzed (n) is listed. Smaller clasts tend to have more distorted and elongated vesicles, whereas larger clasts predominantly preserve domains of rounded vesicles.

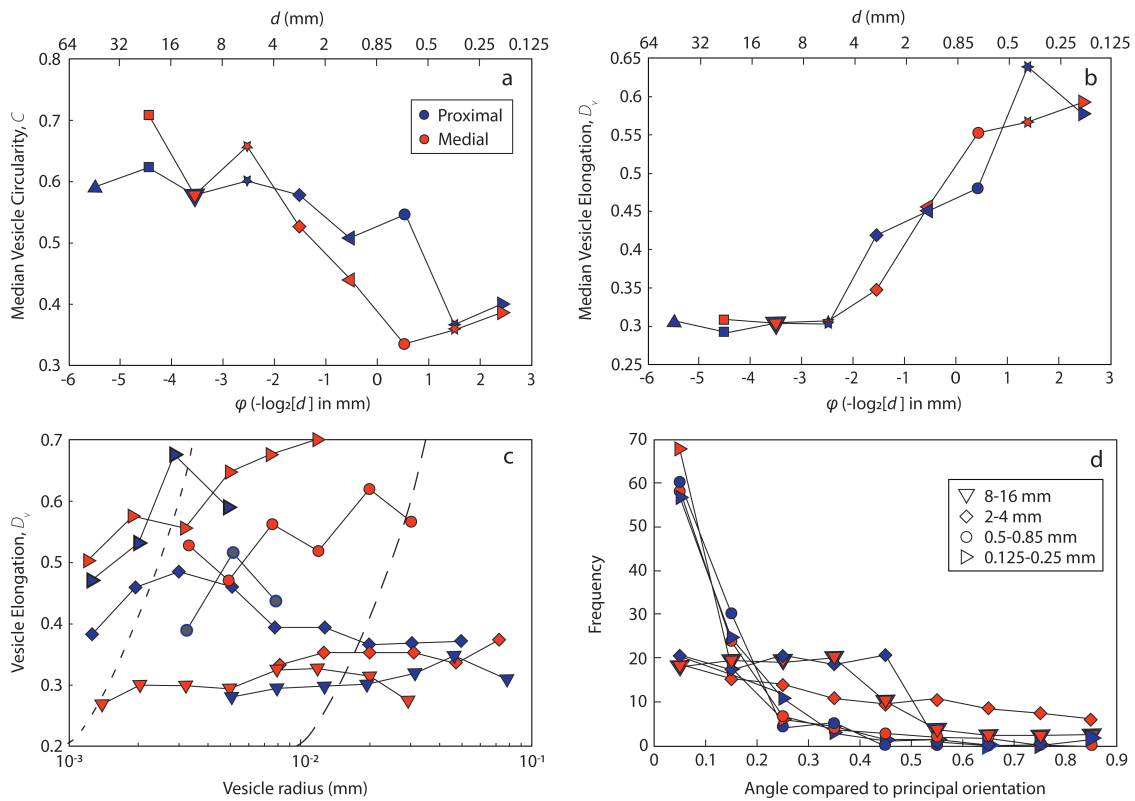


Figure 5: Circularity, deformation (elongation) and orientation of vesicles as a function of vesicle and clast size. Median a) circularity and b) vesicle elongation as a function of pyroclast size. c) Vesicle elongation,  $D_v$ , both as functions of vesicle radius in nine pyroclasts from each size fraction. At least 20 vesicles were counted per bin. The dashed lines correspond to predicted elongation assuming  $D_v = Ca$ , where  $G$  equals either  $10^{-2} \text{ s}^{-1}$  (long dashes) or  $10^{-3} \text{ s}^{-1}$  (short dashes), see Eq. (3). d) Distribution of vesicle orientation compared to the main direction of alignment as a function of pyroclast size. Note that alignment is more pronounced as clast size decreases. See Fig. B2 for further explanation.

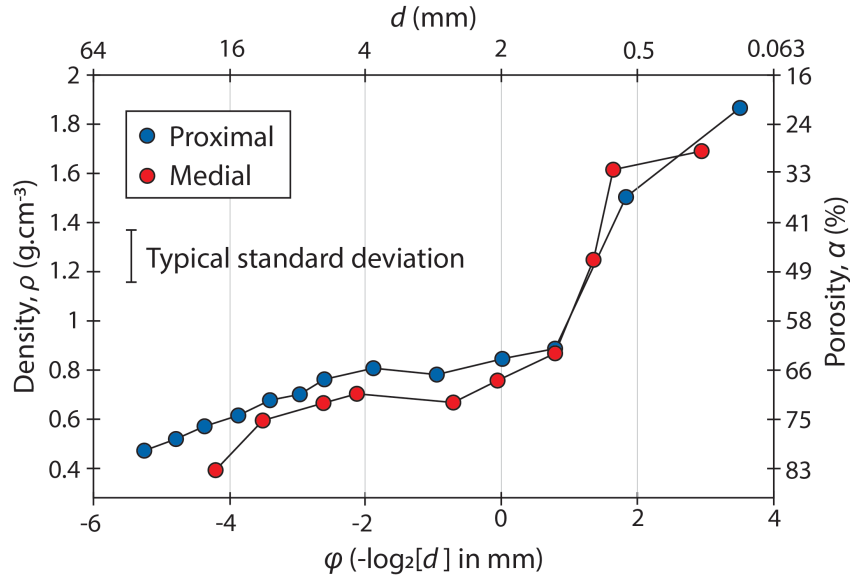


Figure 6: Porosity/density as a function of size for clasts  $0.125 \text{ mm} < d < 64 \text{ mm}$  (lapilli to ash). Pumiceous pyroclasts quadruple in density over this range. Standard deviation for a given point is typically  $0.2 - 0.4 \text{ g.cm}^{-3}$ .

changes in internal texture and density. In this discussion, we first investigate the potential impact of post-fragmentation processes (secondary fragmentation, compaction, and expansion) and transport-related sorting on the shape of our size-density profile. We then justify why we interpret clast size to largely reflect their lateral origin in the conduit and contextualize our results with other studies. We also investigate the origin of the multiple heterogeneous juxtaposed textures observed in some of the smallest clasts (Fig. 3). Lastly, we make suggestions for data use in tephra dispersion models.

### 5.1 Post-fragmentation alteration of pyroclast size

After fragmentation, numerous interparticle collisions, whether inside the conduit or in the plume, result in sample breakage via disruption, abrasion, and or comminution (Dufek and Manga, 2008; Dufek et al., 2012; Jones and Russell, 2017), therefore altering the size distribution of pyroclasts. Numerical simulations of pyroclast disruptive



collisions in the conduit show that larger pyroclasts tend to be more preserved towards the center of the conduit, whereas secondary fragmentation of pyroclasts to smaller sizes is more likely towards the conduit sides (Dufek et al., 2012). Smaller clasts may thus primarily be the product of the secondary fragmentation of larger pyroclasts. Because of their smaller sizes, these clasts would contain fewer large vesicles (the mode of the vesicle size distribution is between 30 and 100  $\mu\text{m}$  (Fig. B.3) and would therefore be relatively denser than the larger clasts they come from.

To investigate this possibility, three homogeneous clasts  $>10\text{ cm}^3$  were manually broken with a hammer into smaller pieces that were then subsequently broken until  $>20$  clasts below  $0.1\text{ cm}^3$  were produced. For each large sample and at each fragmentation step, both the size and the porosity of the fragments  $>2\text{ mm}$  were measured. As all three experiments produced similar results, we present data for only one clast. Summing a weighted density of all of the broken particles from manual fragmentation of the original clast yields a density of  $0.58\text{ g.cm}^{-3}$ , a value within the margin of error of the density of the original clast ( $0.5\text{ g.cm}^{-3}$ , see Fig. B.6). Results show that the average density of the smaller fragments broken from the large clast does not vary in the range  $\sim 2\text{-}30\text{ mm}$ , although density becomes more variable (Fig. B.6). As such, secondary fragmentation alone cannot explain the decrease in clast density with clast size observed for samples  $>1\text{ cm}$  (Fig. 6). Still, secondary fragmentation did produce smaller clasts with a near-constant average density down to particles  $\sim 1\text{ mm}$  in diameter, potentially emulating the plateau in density (porosity) observed in Fig. 6 for samples  $\sim 1\text{-}10\text{ mm}$ . Nonetheless, secondary fragmentation cannot account for the change of texture (i.e., vesicle shape) observed with variation in particle size.

Inter-particle collisions could also compact the rim of colliding clasts, provided that clasts are still partly molten at the time of impact. Such collisions would reduce pyroclast size as porous exteriors densify upon impact(s). This compaction effect would more greatly increase the density of smaller clasts owing to their relatively larger surface area to volume ratios. If not broken upon impact, these compacted clasts should exhibit more flattened vesicles towards their rim. To assess whether post-fragmentation alteration affected final pyroclast size, we compared the internal texture and vesicle size distributions for the center and rim of lapilli 8-64 mm (Figs. 3; B.3). Inspection of SEM images of tens of clasts from across this size range show that viscously-distorted and flattened vesicles exist; however, they remain dispersed throughout clasts in clusters, rather than being preferentially located towards the clasts rim (Fig. 3). Thus, post-fragmentation collision-induced compaction is unlikely to have happened on a large scale during this eruption.

Post-fragmentation expansion can also alter pyroclast size. During this process, the quickly quenched exterior of a clast preserves its molten interior, providing time for gas bubbles to grow. The larger the clast, the longer the interior remains insulated, thus granting more time for bubbles to expand prior to complete quench. Such inflation increases the overall size of the clast (Gardner, 1996; Mitchell et al., 2018), and may cause the dense exterior to crack as it accommodates the expansion, thereby creating a breadcrusted surface (e.g., Wright et al., 2007; Giachetti et al., 2010). Similar to compaction, expansion causes the core of a clast to be more porous than its rim, a disparity that should increase with clast size. If pyroclasts are later broken by inter-particle collisions, the denser rim of compacted or expanded clasts could comprise some

of the smaller samples, which would partly explain the increase in density with decreasing pyroclast size (Fig. 6). However, post-fragmentation expansion was also likely a limited process: both the density and vesicle size distributions of three representative clasts, which cover two orders of magnitude in terms of clast volume, do not significantly change from rim to core (Fig. B.3; Table B.1). Additionally, only one proximal clast of the >700 lapilli analyzed exhibits pervasive breadcrusting; furthermore, the <15% proximal lapilli with some evidence of light breadcrusting tend to have only localized fractures on the order of 1 cm or less in length.

### *5.2 Transport-related sorting*

Transport-related sorting could partly control the size-density curve (Fig. 6), wherein large, lighter particles settle out at the same time as small, dense particles. For a constant density ( $0.472 \text{ g.cm}^{-3}$ , i.e., 80% porosity, typical of the most porous lapilli, or  $2.36 \text{ g.cm}^{-3}$ , i.e., 0% porosity, the density of GM rhyolitic glass), terminal velocities for centimeter-scale spherical particles are 10-20 m/s, whereas submillimeter scale particles have terminal velocities of ~1-10 m/s (Fig. 7; Saxby et al., 2020; Bagheri and Bonadonna, 2016). For a typical Plinian eruption column of 20 km, these terminal velocities give settling times on the order of 20-30 minutes for centimeter-scale pyroclasts versus hours for submillimeter-scale particles. Smaller particles in a given bed could thus in part result from earlier phases, which could bias textural interpretations. We find that clasts from the medial pit are overall finer than those from the proximal sample (Fig. B.5), and lapilli from the proximal pit tend to also be denser (Fig. 6). However, regardless of location sampled, the same sigmoidal density-size trend, and parallel in

changes in clast shapes and textures, prevail. We therefore interpret our trends to largely reflect conduit processes rather than sorting mechanics. Additionally, given that data from a singular bed representing ~3% of the whole proximal pit mirror that of an entire medial pit, clast shapes and vesicle textures reflect conduit dynamics that largely did not change over the course of the eruption.

### *5.3 Clast size and texture reflect lateral sourcing in the conduit*

Larger lapilli's size may have changed after fragmentation via limited expansion and secondary fragmentation; however, we surmise that the size, shape, and texture relationships observed in most pyroclasts result from processes occurring prior to, and at fragmentation. We attribute the increase in density as clast size decreases to the increase in the proportion of elongate vesicles and general textural variability. We also infer that clast size actually reflects lateral sourcing in the conduit, wherein larger clasts tend to preserve rounded-vesicle textures from the interior of the conduit. Smaller clasts result from higher strain rates at conduit margins, which also elongates the vesicles preserved therein (Fig. 8). Although vesicles may somewhat relax after fragmentation (Rust et al., 2003; Dingwell et al., 2016), the preservation of tubular and distorted textures in pyroclasts of all sizes shows that this process is probably limited, especially in small samples for which quenching occurs more rapidly.

Because the flow of magma in the conduit prior to fragmentation is laminar ( $Re \lesssim 1-100$ ; e.g., Gonnermann and Manga, 2007), bubbles' shape and orientation change over time until they reach a steady geometry. The final geometry of vesicles thus depends on

the relative effect of shearing stresses versus restoring stresses, expressed as the capillary number,  $Ca$ :

$$Ca = \frac{rG\mu}{\sigma}, \quad \text{Eq. (4)}$$

where  $r$  (m) is the undeformed vesicle radius,  $G$  ( $s^{-1}$ ) is the shear rate,  $\mu$  (Pa.s) is the melt viscosity, and  $\sigma$  ( $N\ m^{-1}$ ) is the surface tension. Previous studies have shown that vapor bubbles in silicate melts are expected to reach a stable shape rather than break in steady shear flow (e.g., Bentley and Leal, 1986), and that effects of surfactants can be ignored because coalescence textures are abundant in pumice (e.g., Klug and Cashman, 1996) and there are no known surfactants in magmas (e.g., Pal, 2003).

In the case of simple shear and a low-deformation regime ( $Ca \ll 1$ ), Rust et al. (2003) show that vesicle elongation ( $D_v$ ; Eq. 2) equals  $Ca$ . We are justified in similarly exploiting this relationship: during simple shear, bubbles of all sizes are oriented in a single direction (e.g., Rust et al., 2003; Dingwell et al., 2016), which is largely true for our data (Fig. 5d). Our results corroborate those of Dingwell et al. (2016), who examine vesicles in a tubular pumice from the Ramadas Volcanic Center, Argentina. Assuming a magmatic temperature of 850 °C and a water content of ~1 wt% in the rhyolitic melt at fragmentation (Giachetti et al., 2020) yields a viscosity of  $3 \times 10^6$  Pa s (Hess and Dingwell, 1996) and a surface tension of 0.17  $N\ m^{-1}$  (Bagdassarov et al., 2000). We use these values, along with calculated  $D_v$  values, to quantify the shear rates that produced these textures and found  $10^{-3}\ s^{-1} < G < 10^{-2}\ s^{-1}$  (Fig. 5c). However, these shear rates are minimums, as they use  $D_v$  values derived from 2D rather than 3D data. As pyroclast size decreases, the vesicles contained therein are progressively more sheared: vesicles in smaller clasts are less circular (Fig. 5a) and more elongated for all vesicles within a given

clast (Fig. 5b), corresponding to approximately an order-of-magnitude difference between average shear rates when comparing sub-mm to cm-scale clasts (Fig. 5c). We therefore surmise that the size of pyroclasts created at fragmentation depends on the radial position in the conduit, wherein larger clasts are sourced closer to the conduit's center (Fig. 8). This textural interpretation is corroborated by Ohashi et al. (2018), who show that at a given depth,  $D_v$  tends to be higher for bubbles closer to conduit walls where shear rates are nearly an order of magnitude larger than those recorded in the center of the conduit. This conduit location-dependency of the size of pyroclast might be further enhanced by secondary fragmentation, as Dufek et al. (2012) report a higher probability of disruptive inter-pyroclast collisions (and thus production of smaller clasts) near conduit margins following fragmentation.

Our interpretations and conceptual model are also consistent with previous observational work on the texture and shape of pyroclasts. Many studies have interpreted textural heterogeneities, such as vesicle textures (Polacci et al., 2001; Taddeucci and Wohletz, 2001; Rosi et al., 2004; Palladino et al., 2008; Pardo et al., 2014; Shea et al., 2014), as resulting from the flow velocity profile that controls the residence time of magma in the conduit. Particularly, these studies point out that higher shear would concentrate magma containing elongate or polylobate bubbles towards conduit margins. Other studies have also found stick-shaped pumices, which largely contain elongated vesicles, concentrated in the ash size fraction (Rosi et al., 1999; Larsen et al., 2001; Polacci et al., 2003; Saxby et al., 2020). These pumices were interpreted to have formed closer to conduit walls based on their texture and morphology. The aforementioned studies disparately evaluate variations in texture and morphology or do both but only for

a narrow range in pyroclast sizes. In studying both the texture and morphology of pyroclasts for a broad swath of pyroclast sizes, we found that not only do lateral variations in shear control texture and shape, but pyroclast size as well.

At present, only one study exists that reports size-density trends for multiple pits for a given eruption. Eychenne and Le Pennec (2012) evaluated changes in pyroclast density as a function of their size for the 2006 subplinian basaltic eruption of Tungurahua volcano, Ecuador. Regardless of sampled pit, they report a sigmoidal relationship between the density of scoria and their size, wherein density increases  $1.5\times$  as particles decrease in size from 23 mm to 0.09 mm. Despite pyroclasts being from two chemically-distinct eruptions at different volcanoes, vesicular juvenile products have a sigmoidal size vs. density trend wherein density rapidly shifts over a few phi sizes. However, magma composition may impact the range of pyroclast sizes over which density rapidly changes. Eychenne and Le Pennec (2012) see rapid densification over 0.25-4 mm, whereas pumiceous pyroclasts in this study densify over smaller grain sizes, 0.125-2 mm. As silicic magmas generally fragment more energetically, total grain size distributions for mafic eruptions tend to contain <10% by mass fraction of very fine particles (Mastin et al., 2009) as opposed to silicic eruptions (30-50% particles <100  $\mu\text{m}$ ; Rose and Durant, 2009). Such energetic differences could result in the difference in size-density trends.

#### *5.4 Syn-eruptive sintering of porous pyroclasts*

Less than 10% of proximal ash particles 0.125-0.25 mm preserve singular domains of highly distorted vesicles, resembling the interstitial spaces between sintered grains seen in some pyroclastic obsidians from Mono Craters (California; Gardner et al.,

2017; Watkins et al., 2017) and in ash sintering experiments (Gardner et al. 2018, 2019). Gardner et al. (2017) interpret obsidian pyroclasts from Mono Craters to be agglomerated ash particles, which are individually created during magma fragmentation. They then agglomerate and partly sinter on the conduit walls above the fragmentation level before being re-entrained into the eruptive column and ejected together with porous material. Sub-mm-scale particles may thus represent ash agglomerates.

Some of our pumices may have formed by a similar mechanism, wherein they are pumiceous agglomerates of magma fragments that are a few tens of microns to several mm in diameter with variable porosities. Nearly 5-10% of our highly vesicular pumices 0.85-8 mm preserve variable amounts of domains of 1) sheared vesicles oriented in different directions and/or 2) rounded vesicles juxtaposed with domains of sheared vesicles (Fig. 3). We infer these samples to represent multiple pyroclasts that agglomerated and partly sintered immediately after fragmentation, in a manner like that suggested by Gardner et al. (2017). However, given the preservation of porous textures and overall high porosity of our samples, we believe these clasts did not sit and sinter *on the conduit walls* for a few to a few tens of minutes, but rather collided, agglomerated, and partly sintered quickly *inside the conduit* while ascending towards the surface. Each individual pyroclast comprising the agglomerate thus essentially preserves its original texture acquired before fragmentation. Because disruptive collisions are more frequent towards the sides of the conduit (Dufek et al., 2012) and because sintering timescale increases with pyroclast size (Wadsworth et al., 2016; 2019), we believe the interior of the conduit contains larger individual clasts ( $d > 8$  mm) that are inherently less likely to sinter to one another (Fig. 9). This is supported by the fact that textural juxtapositions are



most prominent for 0.85-8 mm, and less so for larger pyroclasts sizes. Further work is necessary and underway, before such a theory can be confirmed (Giachetti et al., *submitted*).

### *5.5 Tephra dispersion models*

Current tephra dispersion models use simplified linear relationships between average density and particle diameter,  $d$ , for pyroclasts  $8 \mu\text{m} < d < 8 \text{ mm}$  (Bonadonna and Phillips, 2003). Pyroclasts  $< 8 \mu\text{m}$  are considered to be pure glass with a density of 2.3-2.6  $\text{g}\cdot\text{cm}^{-3}$  depending on magma composition, whereas those  $> 8 \text{ mm}$  are 70-80% porous. As in Eychenne and Le Pennec (2012), and as interpolated by Manville et al. (2002), we report a sigmoidal rather than a linear relationship between density and clast size. However, not only are data non-linear, the shape of the size-density curve (i.e., where the rapid densification with a small decrease in pyroclast size occurs) is variable, potentially as a result of different magma chemistries and ensuing primary and secondary fragmentation dynamics. Silicic pyroclasts evaluated herein much more rapidly densify over a narrower decrease in clast size as opposed to the proposed linear model.

Density and clast shape directly impact the terminal velocity and thus the amount of time particles remain in the air post-eruption (e.g., Saxby et al., 2020). Here we use the shape-dependent terminal velocity model of Bagheri and Bonadonna (2016) to compare terminal velocities for our data versus particles modeled as spherical and having either a) a constant density or b) a log-linear relationship between size and density (i.e., as in Bonadonna and Phillips, 2003; Fig. 7). Above 8 mm, the log-linear model also uses a constant density of  $0.44 \text{ g cm}^{-3}$ , the average density of our largest proximal lapilli. The constant density models produce the poorest fit to our data, whereas the log-linear model

produces terminal velocity values within 10% of those calculated using real data. For example, 1 mm particles from this study and the log-linear model predict ~4 hours for particles to fall from a 20 km plume, whereas they would take 2 hours using the constant density model of  $0.44 \text{ g.cm}^{-3}$ . Ash (i.e., particles  $< 2 \text{ mm}$ ) typically comprises  $>30\%$  of silicic deposits (Rose and Durant, 2009) and represents a long-term hazard that pollutes air and drinking water (Horwell and Baxter, 2006; Stewart et al., 2006). Given discrepancies between the constant density models and subsequent calculated fall times, we recommend using ground-truthed size-density-shape relationships or log-linear models to improve tephra dispersion models for hazard mitigation.

## 6. Conclusions

Juvenile, mainly porous pyroclasts usually constitute  $>70\%$  of the volume ejected during Plinian eruptions. However, to date and to the best of our knowledge, the study of the relationship between their size and textural characteristics has been limited: studies tend to focus either on a few physical properties or a narrow range of clast sizes. Here, we measure the size, shape and density (porosity) of thousands of pyroclasts spanning  $0.125 \text{ mm} < d < 64 \text{ mm}$ . These clasts were taken from proximal and medial pits of the deposits of the Plinian phase of the 1060 CE eruption of Medicine Lake Volcano, California. We additionally quantified their inner textures by evaluating vesicle size and shape distributions in representative samples spanning the same size range. We ultimately interpret our results in the context of syn- and post-fragmentation processes.

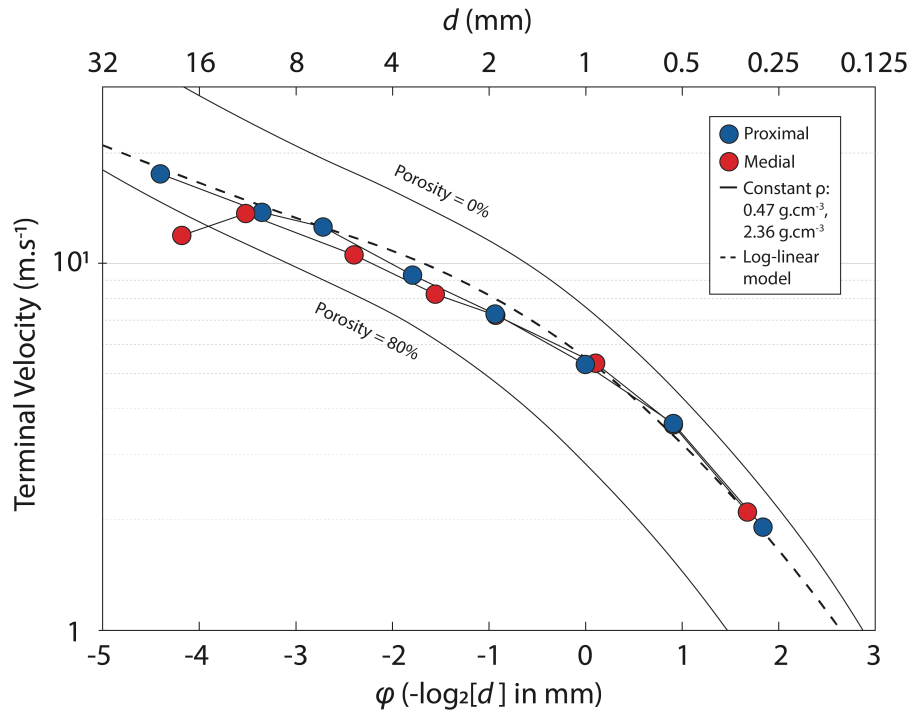


Fig. 7: Calculations of terminal velocity (Bagheri and Bonadonna, 2016) using data from pumiceous particles from Glass Mountain (GM) as well as the constant density and the linear model (L) proposed by Bonadonna and Phillips (2003) for rhyolitic clasts. Clasts for the constant density and log-linear models are assumed spherical. Average shape values for a given size fraction are used for GM data.

Our results show that the size, shape, density and texture of juvenile Plinian pyroclasts are intimately interrelated. As their size decreases from 64 mm to 0.125 mm, pyroclasts shift from equant to tabular to elongate in shape. While rounded vesicles dominate the largest clasts, elongate and distorted vesicle networks become progressively more present with decreasing clast size. Such characteristics are quantified via increase in elongation and a decrease in circularity of vesicles. Concurrently, juvenile pyroclast density increases in a sigmoidal manner from  $0.47 \pm 0.2$  to  $0.8 \pm 0.2$  g.cm<sup>-3</sup> for the

proximal pit, and from  $0.4 \pm 0.2$  to  $0.7 \pm 0.2$  g.cm<sup>-3</sup> for the medial pit as clasts decrease from centimeters to sub-millimeters in diameter. This increase in density (decrease in porosity) is accompanied by a systematic increase in elongated vesicles as pyroclast become smaller. We also note that clast density is almost constant for clasts in the range 1-8 mm, the range over which pyroclasts preserve variable amounts of differently-oriented shear domains, as well as domains of rounded vesicles juxtaposed with domains of shear vesicles.

We show that expansion, compaction and secondary fragmentation did not significantly change the texture of juvenile pyroclasts after fragmentation, but rather interpret the size-dependency of density and texture of Plinian pyroclasts to originate from the lateral position of the magma at fragmentation. Smaller clasts result from higher shearing closer to conduit walls, where greater shear stresses increasingly fragment particles and elongate vesicle networks. However, some pyroclasts 1-8 mm in size likely originate from the agglutination and partial sintering of smaller ash particles immediately after fragmentation.

Tephra dispersion models can be improved by incorporating size-density-shape data rather than constant density models. However, we recognize that at present the paucity of these data may preclude use of the former. In that case, log-linear models suffice to produce reasonable terminal velocity estimates. Still, we suggest that future studies collect data on chemically-similar eruptions to those being modeled, incorporating size-density distributions and shape evaluation of tens to hundreds of pyroclasts every 1 phi spanning lapilli to ash in size.

If our observations and subsequent interpretations of the relationships between Plinian pyroclast size and textures reveal common to all Plinian eruptions, the traditional study of 16-32 mm clasts would thus be informative of eruptive processes occurring in the central part of the conduit only. Consequently, depending on their goal, future studies would have to consider the full spectrum of clast sizes, from the centimeter- to micron-scale, in order to fully capture and understand the complexity of conduit processes.

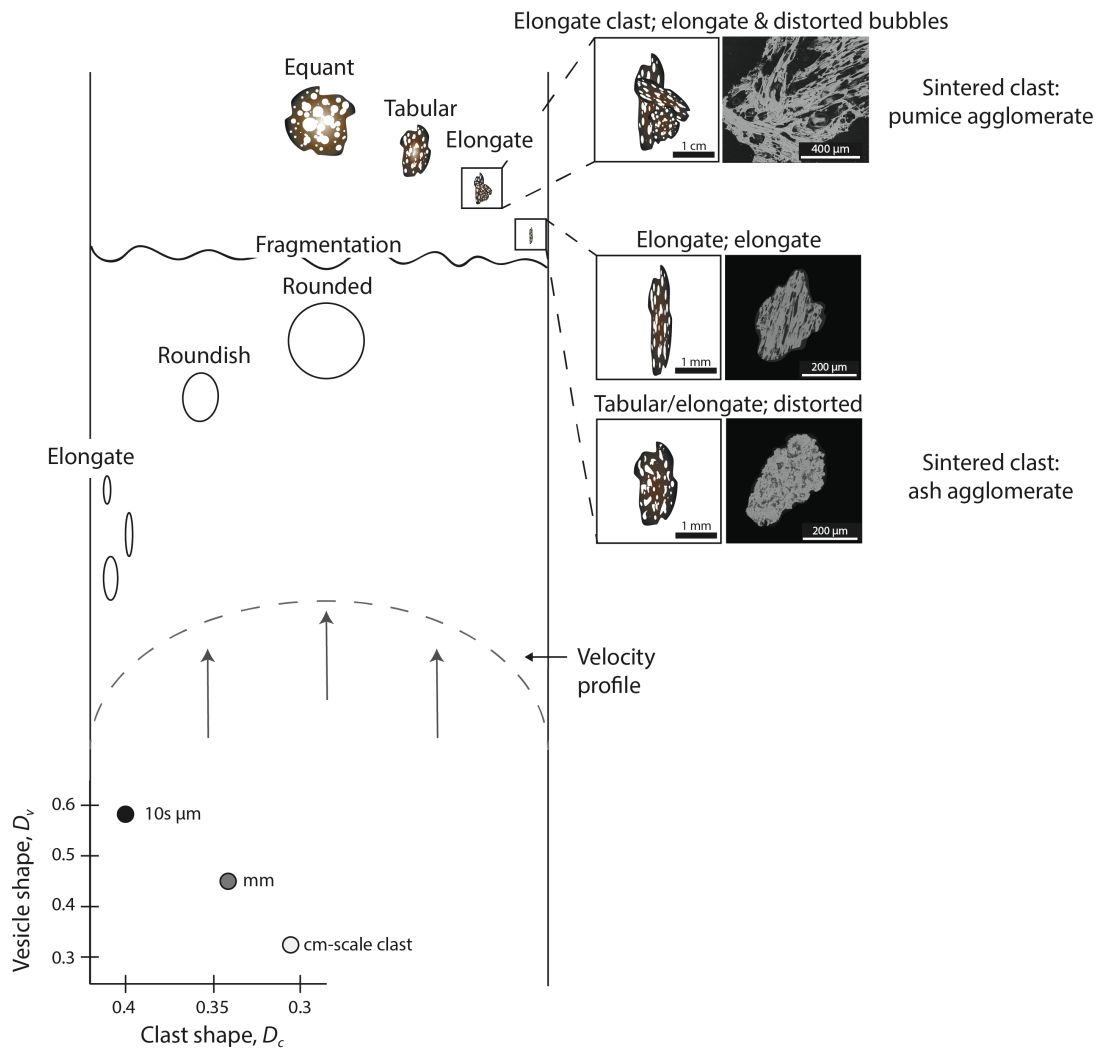


Figure 8: Conceptual model of pyroclast formation in the conduit: at fragmentation, smaller clasts are sourced from closer to the conduit wall, where they undergo higher shear stresses that elongate vesicles and fragment magma more finely. More equant, larger clasts with less elongated vesicles are preferentially produced towards the center of the conduit. Measured average clast shape versus vesicle shape are plotted for clasts from the centimeter ( $2 \text{ mm} < d < 64 \text{ mm}$ ), to the mm-scale ( $0.5 < d < 2 \text{ mm}$ ) to sub-mm scale ( $0.125 \text{ mm} < d < 0.5 \text{ mm}$ ) in size. Average clast shape calculated from  $>100$  clasts for each size range; bubble shape determined from texturally-representative images of individual clasts from each phi subdivision listed in Figure 3 and subsequently averaged.

## 7. Bridge

In Chapter II, I evaluated the characteristics of pyroclasts formed by explosive eruptions. I contextualized findings with previous works that disparately evaluated such characteristics as texture and/or shape on a limited size fraction of rock. In contextualizing this work with those of previous studies, it was clear that pyroclast characteristics are interrelated and reflect the processes controlling their formation. In Chapter III, I leverage this knowledge to shape the methodology of the study. I once again focus on a singular eruption in detail but add more pit locations. I then apply my streamlined, precise approach to sample curation by sieving samples every phi size fraction, and picking consistent size fractions for textural comparison. In this way, I assess trends on three scales: in fine detail for single samples (i.e. one stratigraphic layer), in broad eruption-scale detail for a given pit (i.e. layer versus layer), and in whole-deposit detail wherein we can track variations in depositional conditions. I additionally examine all juvenile material (i.e. pumiceous *and* dense) to further broaden the lens through which we interpret volcanic processes.

## CHAPTER III

### LEVERAGING PHYSICAL DATA OF JUVENILE PRODUCTS TO UNDERSTAND THE EXPLOSIVE-EFFUSIVE TRANSITION

This chapter is being prepared for journal submission. K.R. Trafton and T. Giachetti conceived the study. K.R. Trafton collected and analyzed the data, wrote the manuscript, and improved its contents based on the edits of T. Giachetti.

#### **1. Introduction**

Explosive volcanism produces myriad hazards, from deadly pyroclastic flows to widespread ejecta dispersal. In contrast, effusive eruptions can saturate airways with toxic gases and produce pervasive lava flows, but nonetheless have great humane consequences. Characterizing such components offers invaluable insights into the innerworkings of a volcano, allowing for better constraint of hazards.

Eruptive behavior has been interpreted to be controlled by regional stress fields (Scandone et al., 2007), decompression rate (Alidibirov et al., 1996; Castro et al., 2008), magma storage conditions (Popa et al., 2021), crustal properties (Jaupart et al., 1991; Kennedy et al., 2010), and external assimilates (Austin-Erickson et al., 2008). The properties of the magma itself are also major controls (e.g., volatile content, rheology, crystallinity; Sparks et al., 1999; Ruprecht et al., 2010; Popa et al., 2021). In general, characterizing pyroclasts' physical (Clarke et al., 2007; Mueller et al., 2011; Larue et al., 2013; Janebo et al., 2018; Davies et al., 2021) and geochemical (Rust and Cashman, 2007; Cassidy et al., 2015; Watkins et al., 2017; Giachetti et al., 2020) signatures gives diagnostic snapshots of near-fragmentation conduit processes.



Historic observations at Volcán Chaitén in 2008 (Chile; Castro et al., 2009) and Cordon Caulle in 2011-2012 (Chile; Schipper et al., 2013, Schipper et al., 2021), the first and only observations of rhyolitic eruptions, showed that explosive and effusive volcanism of highly silicic magmas can exist concurrently, despite classically being considered irreconcilable endmembers (Eichelberger et al., 1986; Jaupart and Allègre, 1991). Recent work interprets hybrid activity to result from the pyroclastic origin of obsidian, wherein sintered pyroclastic products can partially clog the conduit and effuse as lava while explosions continue (Wadsworth et al., 2020). Evidence for a pyroclastic origin of obsidian is based on both textural and geochemical observations. Obsidian particles found in the tephra deposit of the ~1350 C.E. Mono Craters eruption (CA, USA), preserve juxtaposed variably-bubbly domains that trap xenoliths (Gardner et al., 2017) and have variable H<sub>2</sub>O and CO<sub>2</sub> contents (Watkins et al., 2017). Additionally, rhyolitic lava from the 2008 eruption of Volcán Chaitén, Chile and the 2011-2012 eruption of Cordon Caulle contain ash- and lapilli-choked degassing networks (i.e. tuffisites; Castro et al., 2012; Paisley et al., 2019; Schipper et al., 2021). Such an assembly of textural domains strongly suggests that both obsidian pyroclasts and tuffisitic obsidian lava formed principally by agglomeration and sintering of fragmented products in the conduit.

The 2011-2012 eruption of Cordon Caulle began violently with >15 km high Plinian columns (Schipper et al., 2013). The eruption switched to sub-Plinian and then to Vulcanian events, both styles occurring with concurrent lava effusion (Schipper et al., 2013). Many other Plinian rhyolitic eruptions ended with a sputtering or pulsatory behavior that may have also included block-and-ash flows before lava extrusion (e.g. 550

B.P. Inyo volcanic chain, CA, U.S.A., Castro and Gardner, 2008; Novarupta 1912, AK, U.S.A., Nguyen et al., 2014; Ogburn et al., 2015, and references therein; Cassidy et al., 2018, and references therein). Considering these observations, pulsatory behavior may herald a change to final effusive activity, and its onset may help constrain the duration of an eruption.

In this study, we examine the 640 C.E. eruption of Newberry Volcano (central Oregon, U.S.A.), which began explosively with the Newberry Pumice tephra fallout and terminated by the effusion of the Big Obsidian Flow. With only one transition from explosive to effusive behavior, it serves as a simple case for examining eruption dynamics. Previous observations note the presence of lithic-rich layers sandwiching lapilli layers (Kuehn, 2002) in the upper portion of the tephra deposit, which have been interpreted to potentially result from co-shed density currents of a sub-Plinian plume (Rust and Cashman, 2007). Such succession of layers is common in Vulcanian deposits (Sigurdsson et al., 2015), and to date no work has comparatively examined these ash layers in the greater context of the lapilli component. Past studies of the Newberry Pumice fallout deposit examined clast size and distribution (Gardner et al., 1998), geochemistry (Kuehn, 2002; Rust and Cashman, 2007; Di Genova, 2019), tephrochronology (Kuehn, 2002), and textures of obsidian pyroclasts (Rust and Cashman, 2007). However, detailed textural analyses of the pumice that comprises >95 wt% of the fallout (Rust and Cashman, 2007) have yet to be done. To this extent, we perform such physical analyses, including external texture, density, and mass distribution of pumiceous lapilli and ash layers spanning 4 pits roughly along the main dispersal axis of the Newberry Pumice. The crystal-poor nature of the magma (Kuehn, 2002) allows for

largely unfettered observation/analysis of characteristics. We then amalgamate our study with those of previous authors (MacLeod et al., 1995; Kuehn, 2002; Rust and Cashman, 2007) to holistically examine how the 640 CE eruption of Newberry volcano eruption transpired. Ultimately, we contextualize our model of the explosive-effusive transition with those of the greater community (Cassidy et al., 2018; Wadsworth et al., 2020) and assess Vulcanian behavior as a potential harbinger for hybrid explosive-effusive activity during rhyolitic eruptions.

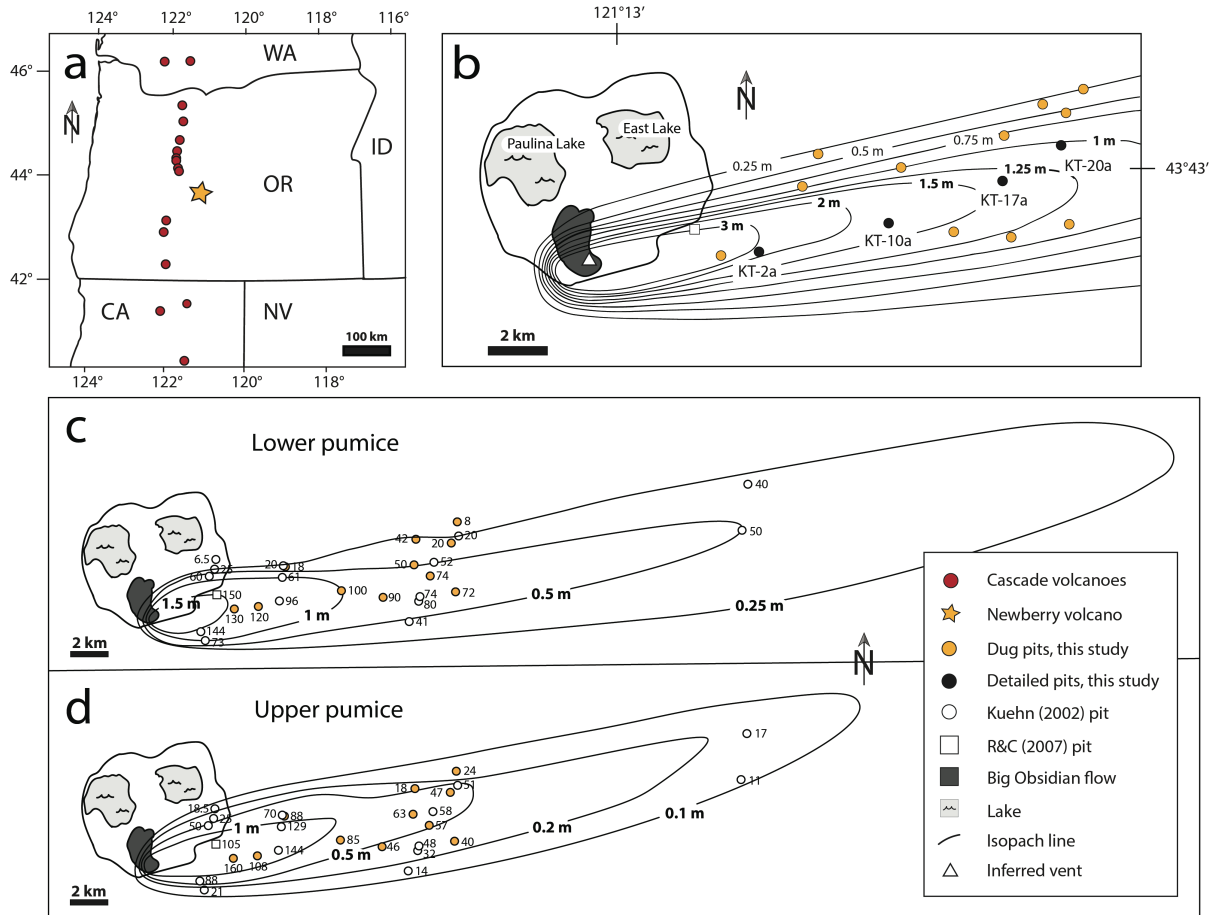
## **2. Geologic Setting**

### *2.1 Locality*

Newberry Volcano (central Oregon, U.S.A) is a shield-shaped composite volcanic complex that lies slightly east of the Cascade volcanic arc at the intersection of the Walker, Brothers, and Sisters fault zones (Fig 1a; Walker and MacLeod, 1991; Jordan et al., 2004). Newberry results from either hot spot (Xue and Allan, 2006) or, as recently proposed, subduction-related volcanism (Till et al., 2013). It tends to erupt every ~1,000 years (Gardner et al., 1998) and is classified as a very high threat volcano by the United States Geological Survey (Ewert, 2007; Ewert et al., 2018). Tomographic imaging of the underlying structure reveals a likely magma chamber 3-5 km below the surface (Heath et al., 2015).

Newberry has produced myriad and varied eruptions, both in terms of volume and magma composition. It is the second most voluminous volcano in the Cascades (~500 km<sup>3</sup>) and has hundreds of volcanic vents and cones (Donnelly-Nolan et al., 2011), having erupted explosively over 50 times in the past 600,000 years. Fallout from these explosive

eruptions at Newberry has been found in five states across the western U.S.A. (Kuehn and Foit, 2006). Mafic lava flows and scoria cones swath the flanks of the volcano and extend ~100 km from the actual caldera that formed ~75,000 years ago (MacLeod et al., 1995).



**Figure 1** a) Locality map of Newberry Volcano, central OR, U.S.A. b) Newberry Volcano, where black lines are isopach lines delineating entire deposit thickness for its 1300 BP eruption. R&C (2007) refers to Rust and Cashman (2007)'s sample site, which is the same as Kuehn (2002)'s 97-5 site. c) Lower pumice deposit and d) Upper pumice deposit inferred by pit data from this study, Kuehn (2002), and Rust and Cashman (2007). Lower pumice's 0.25 m line was drawn with the assumption that the eastern part of the deposit was all lower pumice, thus following Kuehn (2002)'s whole deposit 0.25 m isopach line.

### 2.3 *The 640 C.E. Big Obsidian eruptive period*

The most recent eruption of Newberry was the 640 C.E. Big Obsidian Flow eruptive event. It began explosively with tephra fallout (the Newberry Pumice;  $0.4 \pm 0.2$  km<sup>3</sup> non-DRE; Kuehn, 2002) and terminated effusively with lava extrusion (the Big Obsidian Flow; 0.1 km<sup>3</sup>; Sherrod and MacLeod, 1979). The focus of this study is the Newberry Pumice. The Newberry Pumice forms a singular ellipse elongated east-northeast from the interpreted vent in the southern tip of the Big Obsidian flow (Fig. 1b). The 0.25 m isopach extends ~60 km from the caldera towards Brothers, OR (Kuehn, 2002; MacLeod et al., 1995). The Newberry Pumice attains an estimated near-vent thickness of >13 m, where 1 m blocks can be found (Sherrod et al., 1997).

The main components of the Newberry Pumice deposit are juvenile pumice and obsidian pyroclasts, and lithics. Pumices lapilli are generally light gray, though some richer in microlite appear as a darker gray. Obsidian pyroclasts appear as translucent to black dense chips. Lithics include mafic, red/brown/gray mafic scoriaceous and dense clasts (Kuehn, 2002; Rust and Cashman, 2007; this study). The Newberry Pumice is notably distinguishable from the yellow-orange deposit of the underlying 5670 BCE climactic eruption of Mt. Mazama-Giiwas (Klug et al., 2002).

The Newberry Pumice has been previously divided into two units, the Lower Pumice (LP) and the Upper Pumice (UP), separated by an ash horizon and distinguished by a change in obsidian textures (Rust and Cashman, 2007) and/or marked change in clast size (Kuehn, 2002). Both phases were erupted in roughly the same direction (northeast), but the UP is slightly more northerly (Fig. 1c-d; Kuehn, 2002; this study). The LP also tends to be thicker, more well-sorted, and supported by larger lapilli (Kuehn,

2002). The Newberry Pumice has been interpreted to be from a single Plinian event (Gardner et al., 1998), wherein ash is co-surge deposits, but more recent interpretations favor a two-phase Subplinian event (Kuehn, 2002; Rust and Cashman, 2007) with the first ash layer representing a hiatus and deriving from a plug and fallback (Rust and Cashman, 2007). Subsequent layers have been suggested to represent density currents shed from the plume (Rust and Cashman, 2007).

The Paulina Lake ash flow was also emplaced after tephra deposition and is found in exposures on the south shore of Paulina Lake and the south caldera rim (Kuehn, 2002). It is comprised of poorly-sorted ash and pumiceous lapilli (MacLeod et al., 1995), exhibits bedding in the lower half of the deposit, and varies in thickness from 0.5 to 2 m (Kuehn, 2002). The ~1.8 km long Big Obsidian Flow, which constitutes the final phase of this eruption, is within the caldera and attains thicknesses > 20 m (Fig. 1b; Sherrod et al., 1997). The Newberry Pumice, Paulina Lake ash flow, and the Big Obsidian Flow are all highly silicic (72.8% SiO<sub>2</sub>; Macleod et al., 1995) and geochemically identical in terms of major element composition (Kuehn, 2002), further supporting the idea that they are all part of a single, protracted eruption.

### **3. Methodology**

Fifteen pits were dug dispersed across the deposit, including several pits located roughly on the main dispersal axes of the LP and UP (Fig. 1b-d). At each location, the entire Newberry Pumice deposit was excavated and divided in subunits, which were then measured for thickness, described in detail, photographed, and ultimately sampled. Bulk samples (of several hundred grams of tephra) were taken from varying stratigraphic

heights at each pit and stored in plastic sample bags. Samples from four pits located on the dispersal axis (totaling 37 samples; Fig. 2) were analyzed for componentry, mass distribution, and texture. For one pit (KT-10a), we also measured the density of 100 lapilli from 5 samples scattered across the whole Newberry Pumice section. One pit is proximal (5.8 km from inferred vent, two are medial (10.4 km, 12.7 km), and one medial-distal (16.8 km).

The same sample preparation and analytical procedure were used for all the samples. First, each sample was sieved every phi from 3 to -5  $\phi$  (0.125 to 32 mm), where  $\phi = -\log_2(d)$  and  $d$  is particle equivalent diameter in millimeters. Each sieve fraction was 1) ultrasonicated for five minutes, 2) dried overnight at 100 °C to remove adsorbed water, and 3) weighed using a high precision balance. Point count componentry done on 100-450 clasts every size fraction (every  $\phi$ ), wherein individual grains were designated as pumice, obsidian, or lithics (Fig. 3). Obsidian may appear as clear glass (Fig. 3c), but it is geochemically identical to black obsidian (Rust and Cashman, 2007). Any larger size fractions wherein the lack of sample precluded a statistically robust analysis was noted.

For pumice lapilli 8-16 mm ( $-4 < \phi < -3$ ), we evaluated exterior texture under a microscope for 50-100 clasts every  $\phi$ . We noted whether each lapillus exhibited breadcrusting/fractures, banding of alternating obsidian-like and pumice-like textures, microphenocrysts/xenocrysts, or evidence of sintering, wherein clasts appear to be amalgamations of smaller clasts, exhibiting juxtaposed texturally-distinct domains that trap oxidized ash and/or lithic material (Trafton and Giachetti, 2021; Giachetti et al., 2021; Fig. 3d, e). We also recorded whether the clast texture was predominantly tubular

(i.e. largely comprised of elongate bubbles; Fig. 3f), or homogeneous (i.e., containing more spherical bubbles).

For pit KT-10a (Figs. 1, 2), we measured the volume of >100 lapilli per sample for five samples collected 15-40 cm apart vertically. These lapilli are all within the same  $\phi$  (8-16 mm in diameter) per suggested methodology (Houghton and Wilson, 1989; Shea et al., 2010). Clast density was directly obtained using the classical immersion method (Houghton and Wilson, 1989) or, for smaller clasts, calculated by dividing the mass of the clast using high precision balance by its volume via a Microtrac PartAn 3D particle size analyzer (Trafton and Giachetti, 2021). We report and plot data in terms of both density ( $\rho$ ) and porosity ( $\alpha$ ), and similarly report size in terms of diameter (d), volume (V), and phi size ( $\phi$ ). Clast porosity,  $\alpha$  in %, is given by

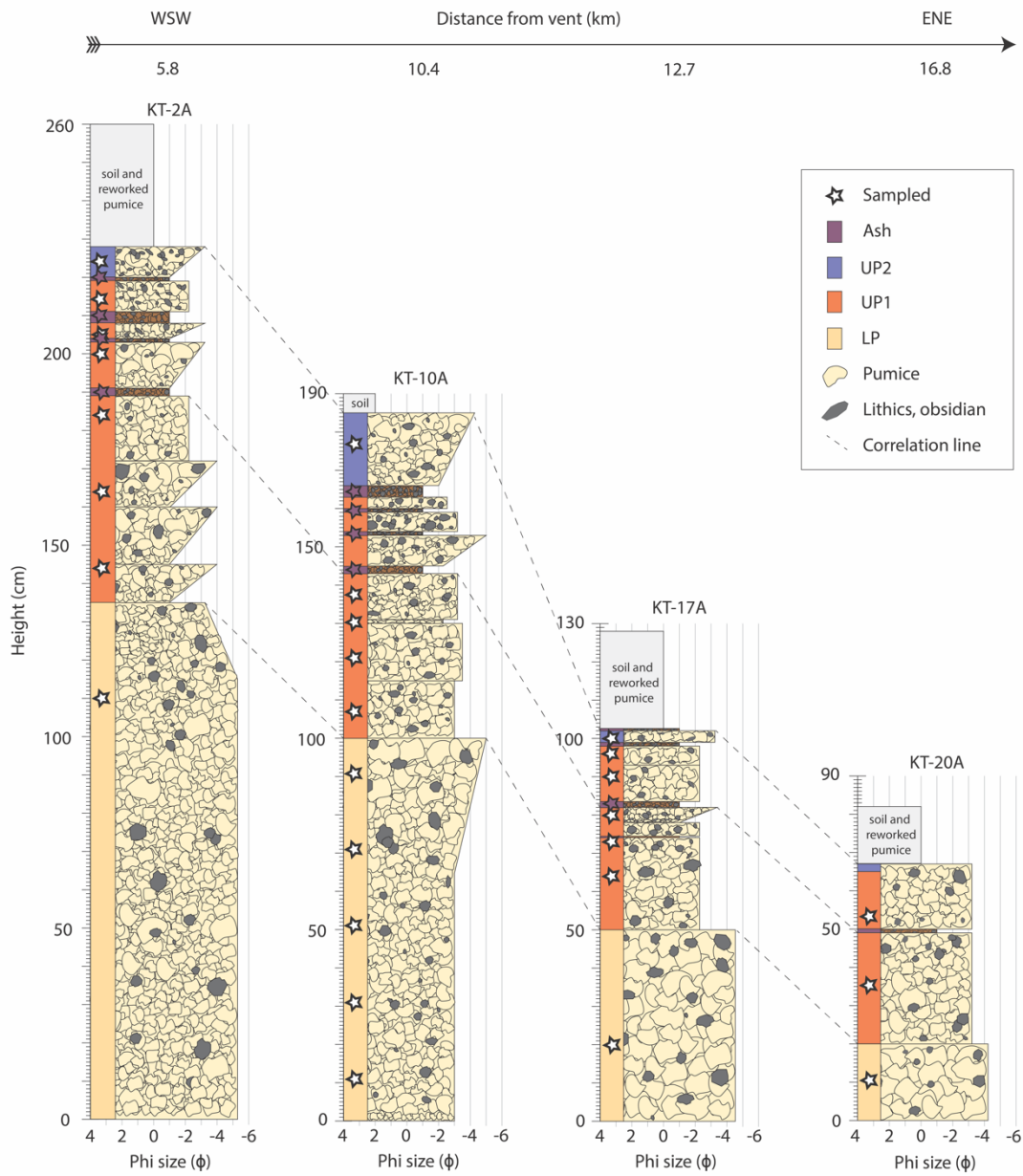
$$\alpha = 100 \times M / \rho_s \times V \quad (1)$$

where M is the mass of a particle, V its volume, and  $\rho_s = 2.32 \pm 0.01 \text{ g cm}^{-3}$  is the density of the solid phase (Giachetti et al., 2021). We assume a density of air of  $0 \text{ g cm}^{-3}$ .

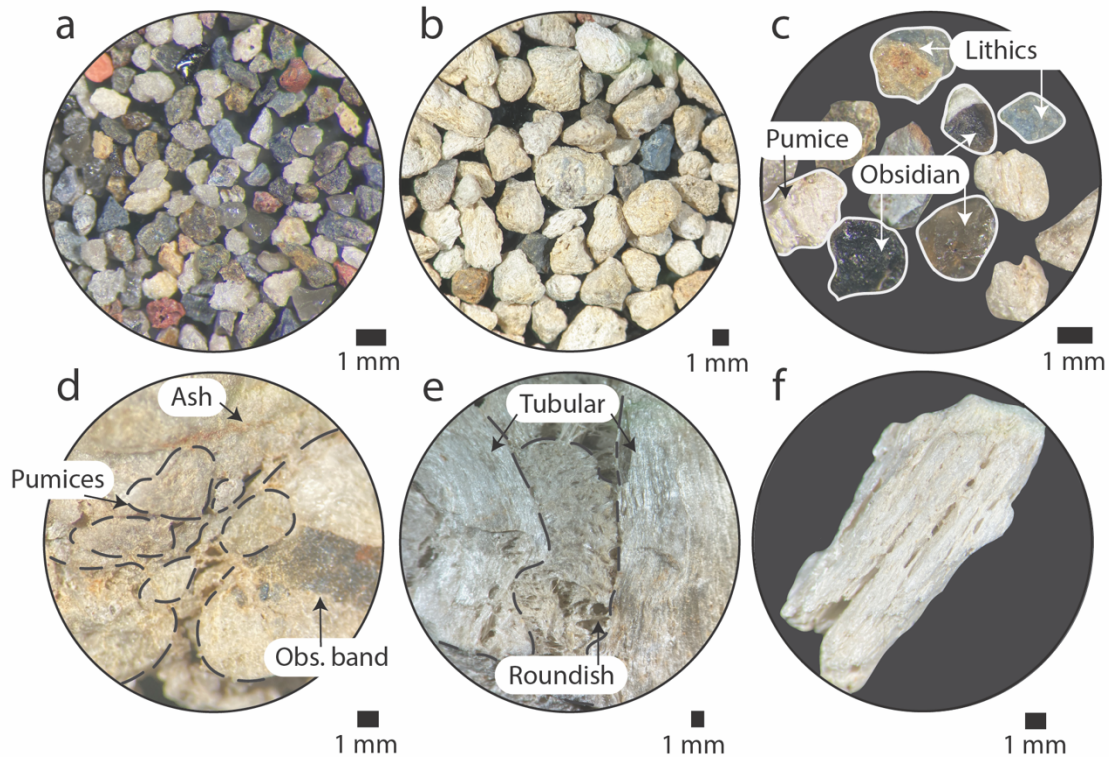
#### 4. Results

Rust and Cashman (2007) and Kuehn (2002) divided the Newberry Pumice stratigraphy into two sections, the Lower Newberry pumice (LP) and the Upper Newberry pumice (UP). At any given proximal or medial pit investigated, the LP comprises  $\sim 60 \pm 5\%$  of the total Newberry Pumice deposit, and presents as a relatively





**Figure 2** Stratigraphic columns of the four sampled pits based on field observations. Depth is represented vertically wherein 0 cm is the contact between the Newberry and the underlying Mt. Mazama deposits. Average clast size in the horizontal based on field observations. Colored bars indicate classification of layers as Lower (LP), Upper (UP1), and Uppermost (UP2) Newberry pumice. Ash layers are also indicated in purple. Sampled layers are starred.



**Figure 3** Physical attributes of samples. a) Ash-sized (0.25-0.5mm;  $-1 < \phi < -2$ ) bulk sample rich in lithics and obsidian. b) Pumice-dominated lapilli sample (2-4 mm;  $1 < \phi < 2$ ). c) Components: pumice, obsidian, and lithics. d) Sintered pumiceous clast made of amalgamated pumice, ash (red-brown line), and obsidian. e) Another type of sintered clast wherein clasts with disparate bubble domains are juxtaposed (i.e. tubular and ~spherical). f) A tubular pumice – an elongated clast with elongated vesicles.

coarse, singular package of pumiceous lapilli. The UP is also largely pumiceous but exhibits alternating packages dominated either by lapilli- or ash-sized particles (Fig. 2). We further divide UP into UP1 and UP2, wherein UP2 is the final lapilli-dominated layer and UP1 contains intermittent lapilli and ash layer packages. We do this as UP1 is texturally distinct from UP2, containing obsidian with highly variable textures (i.e., with xenocrysts, trapped clasts, and/or juxtaposed domains of spherical versus distorted bubbles; Table 1; Rust and Cashman, 2007). UP2 also has a much higher amount of

obsidian in general, an observation also made by Rust and Cashman (2007). We thus present results in terms of the “LP,” “UP1,” and “UP2” sections of the deposit. We also amalgamate data from all ash layers given their similarity in componentry, color, and mass distribution (Fig. 4). Results are summarized in Table 1.

#### *4.1 General trends*

Regardless of section, pyroclast size is positively correlated with pumice content, from 30-55% pumice at ~0.25 mm to 95-100% pumice for clasts larger than ~1 cm (Fig. 4). Conversely, size is inversely correlated with lithic and obsidian content. At the smallest size fraction analyzed ( $\phi = 2-3$ ), pumice content suddenly increases while lithic content decreases. No obsidian clasts larger than 16 mm was found for any section from the pits surveyed; however, more proximal pits do have obsidian of this size (Rust and Cashman, 2007). Less than 1% of the >3000 pumiceous clasts surveyed exhibited obsidian banding or breadcrusting. Less than 3% contain macroscopic crystals.

#### *4.2 Lower Newbery Pumice (LP)*

The lower deposit is one continuous pumice-supported package whose grading changes with distance from the vent from normal grading (KT-2A, most proximal), to reverse grading (KT-10A), to no obvious grading (KT-17A and KT-20A, Fig. 2). The LP also contains the most pumice and least obsidian and lithics (Figs. 4, 5). Pumices in this layer are also the least dense (median density:  $0.61 \pm 0.11 \text{ g cm}^{-3}$ ; Figs. 5, 6a). The mass distribution tends to be sigmoidal wherein the mass is predominantly composed of lapilli-sized clasts (Fig. 5, 6b). It tends to also have the most tubular pumice clasts overall (more

than twice as many tubular as homogeneous pumices; Fig. 5). The fraction of sintered clasts is similarly high, up to 30% of all lapilli exhibiting this texture.

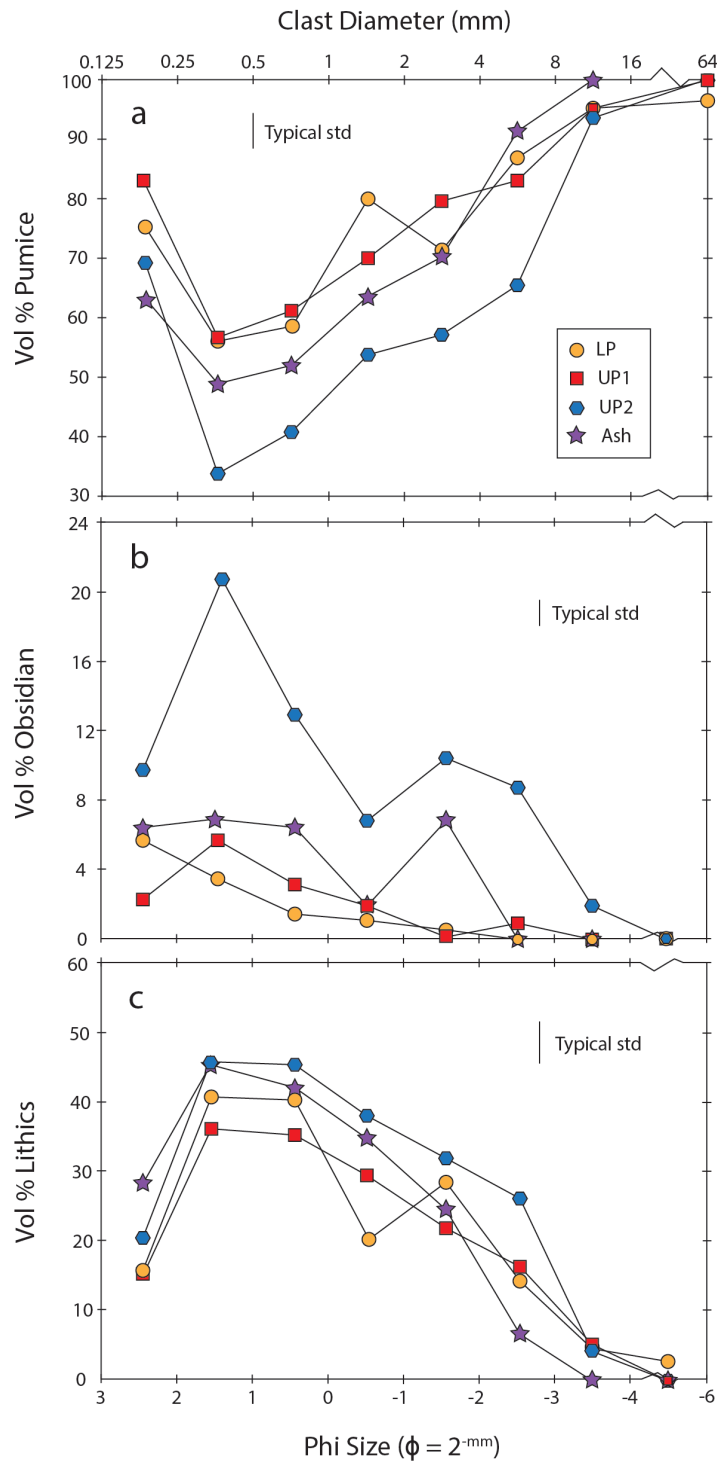
### *4.3 Upper Newberry Pumice 1 (UP1)*

#### 4.3.1. Lapilli-dominated layers

The lapilli-dominated layers of UP1 are generally less coarse than those of LP (Fig. 5, 6b). Proximal to medial deposits may exhibit several packages of a few to ten-centimeter-thick layers that are massive or reversely graded (Fig. 2). These layers contain an increasingly high mass fraction of obsidian pyroclasts and lithics as compared to the LP (Fig. 5). The amount of tubular pumice is highly variable but on average contains fewer tubular lapilli than compared to the LP (Fig. 5). Pumiceous lapilli are also denser than in the LP (median density:  $\sim 0.70 \pm 0.14$  g cm<sup>-3</sup>; Fig. 6a). The mass distribution shifts to lower sizes and exhibits a bimodal distribution with one peak at  $\phi \sim -2 \pm 0.5$  and the other at  $\phi \sim 0.5$  (Fig. 6b), with median diameter around 1 cm.

#### 4.3.2. Ash-dominated layers

The ash layers appear in the upper third of UP1 and are a few centimeters thick at most (Fig. 2). They appear grey to mahogany brown in the field and tend to be riddled with roots, particularly just below UP2 (Fig. 2). The number and thickness of the ash layers vary from pit to pit (none to seven), as closer locales wherein larger clasts were deposited may have resulted in the erasure of delicate ash layers (Kuehn, 2002). The first centimeter(s)-thick ash layer above the first few packages of upper lapilli layers in UP1 is



**Figure 4** Componentry of bulk samples sieved every phi and amalgamated stratigraphically as lower (LP), upper (UP1), uppermost (UP2), or ash for pit KT-10a. Here shown is clast size (in diameter and phi) versus a) volume % pumice, b) volume % obsidian, and c) volume % lithics. Typical standard deviation given for LP, UP1, and ash; there is only one sample for UP2.

used as a datum to correlate three of the pits based on its componentry, color, and consistent thickness in proximal and medial pits (Fig. 2). The componentry of the ash-dominated layers is like that of their lapilli-dominated counterparts in UP1, albeit with a slightly higher portion of lithics and pyroclastic obsidian. Proportions of homogeneous to tubular clasts can be variable or consistent depending on the pit (Fig. 5).

#### *4.4 Upper Newberry Pumice 2 (UP2)*

The UP2 section is a lapilli-dominated layer that is slightly finer than the lapilli-dominated layers that comprise most of UP1 (Fig. 5). This layer coarsens upwards in proximal and medial pits (Fig. 2), a feature that is less evident as distance from the vent increases. UP2 is relatively saturated in lithics and markedly so in obsidian pyroclasts compared to all underlying layers, ash included (Fig. 4). On average, UP2 contains similar amounts of tubular clasts to LP (Fig. 5). Pumiceous lapilli have a more widespread distribution of densities but overall are denser than underlying layers ( $0.72 \text{ g cm}^{-3} \pm 0.16$ ; Fig. 6a). The mass distribution is like that of UP1, albeit with a less pronounced bimodality, with a main peak at  $\phi = -1.5$  and another at  $\phi = 0.5$  (Fig. 6b).

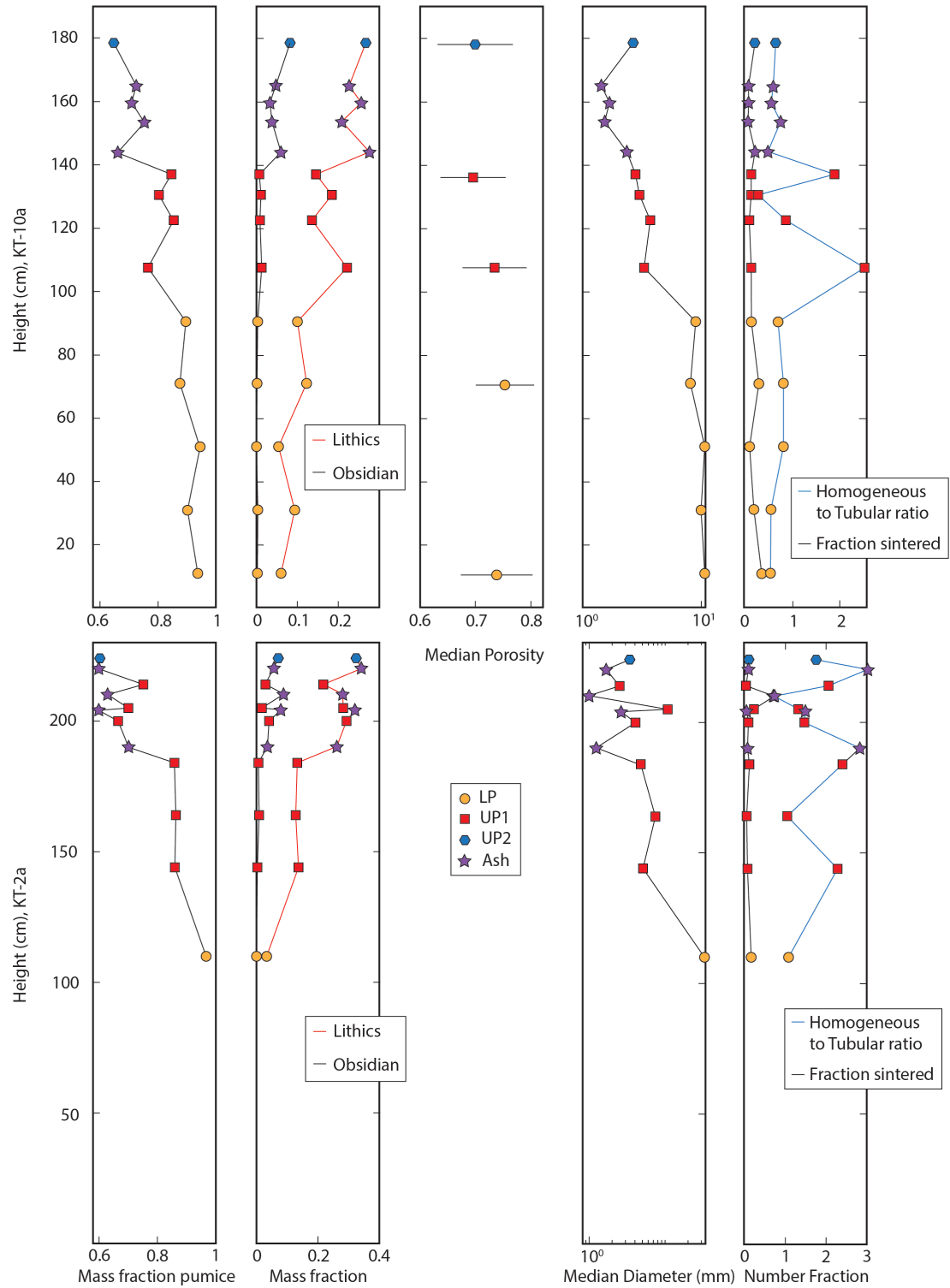
## **5. Discussion**

The main characteristics of all three sections are summarized in Table 1 and discussed below.

### 5.1. LP

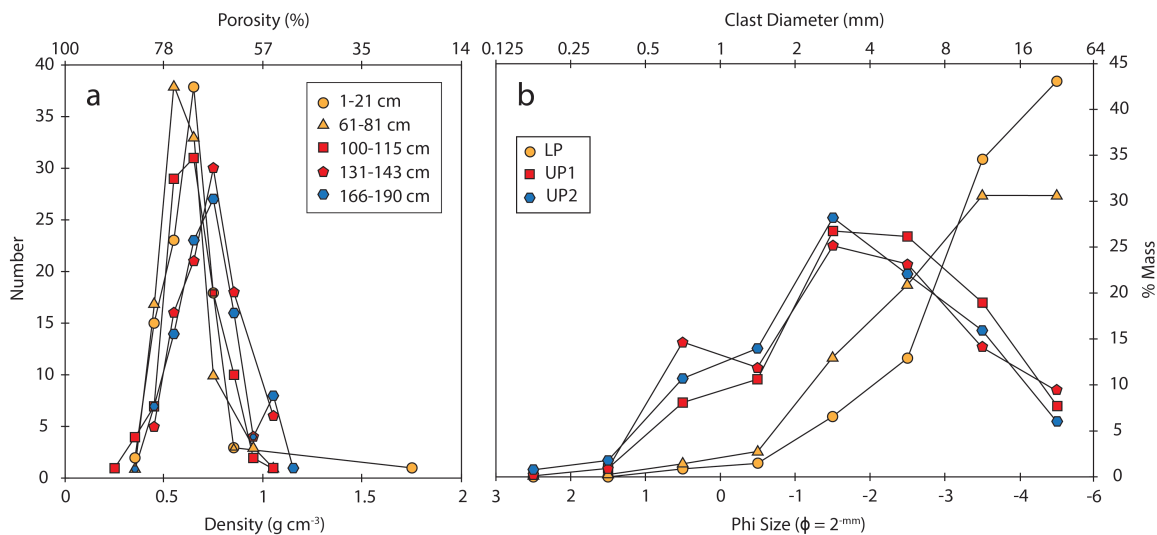
The first section of the Newberry Pumice deposit contains well-sorted lapilli that are predominantly pumice (Figs. 4, 5, 6a), evidencing a steady plume. Based on our, Kuehn (2002), and Rust and Cashman (2007)'s thickness data (Fig. 1), we drew isopach maps for LP and calculated the volume of the LP phase using a Weibull function (Bonadonna and Costa, 2013; Fig. A1). We found the amount of expelled during this phase to be 0.88 km<sup>3</sup> non-DRE (0.2-0.4 km<sup>3</sup> DRE), indicative of a sub-Plinian-sized eruption (Sigurdsson, 2000).

The concentration of tubular clasts in LP is relatively high (55-65%; Fig. 5). Such predominance of tubular lapilli indicates higher ascent rates (Taddeucci and Wohletz, 2001; Palledino et al., 2008) that prevail even into the center part of the conduit, in which elongated bubbles are preserved in cm-scale clasts (Trafton and Giachetti, 2021). The greatest number of clasts showing evidence of amalgamation and partial sintering (10-35%; Fig. 5) also indicates that inter-clast collisions occurred while clasts remained partly malleable, which can occur in (sub-)Plinian eruptions wherein the timescale of sintering of ~50 s is on par with the ascent timescale ~10-60 s (Giachetti et al., 2021). At the same time, disruptive break-up may be comparatively low as there is only one main peak in the particle size distribution (Fig. 6b), as would result from relatively shallow fragmentation zone and efficient fluidization of the packed beds of pyroclasts after fragmentation (Dufek et al., 2012; Giachetti et al., 2021). The observation that LP pumice lapilli tend to be more porous and preserve large bubbles (Fig. 7a, b) is also consistent with shallow fragmentation as it allows for more time between bubble nucleation and sample quench (Gonnermann and Manga, 2007).



**Figure 5** Physical data by stratigraphic layer for pits KT-10a (medial, top row) and KT-2a (proximal, bottom row) pits. Similar general trends are apparent in other pits. Density measurements only done for KT-10a. LP is Lower Pumice, UP is Upper Pumice.





**Figure 6** a) Density and b) mass distribution for different layers from pit KT-10a.

While pumice lapilli record dynamics closer to the inner conduit (Trafton and Giachetti, 2021), obsidian pyroclasts capture conduit margin dynamics (e.g., Gardner et al., 2017; Watkins et al., 2017). The Newberry 640 CE Big Obsidian event, similar to the 1325-1350 CE North Mono Craters eruption in scale and eruptive style (Gardner et al., 2017; Sieh and Bursik, 1986), preserves obsidian pyroclasts that may in part derive from ash amalgamation and advanced sintering along conduit margins (Gardner et al., 2017; Wadsworth et al., 2020). The water content in pyroclastic obsidians in LP is extremely limited (<1 wt%), especially compared to the UP (1-6 wt%). Moreover, the limited breadth of water content preserved in LP clasts suggests shallow formation of these obsidian pyroclasts (<1 km depth; Rust and Cashman, 2007), consistent with a shallow fragmentation of magma.

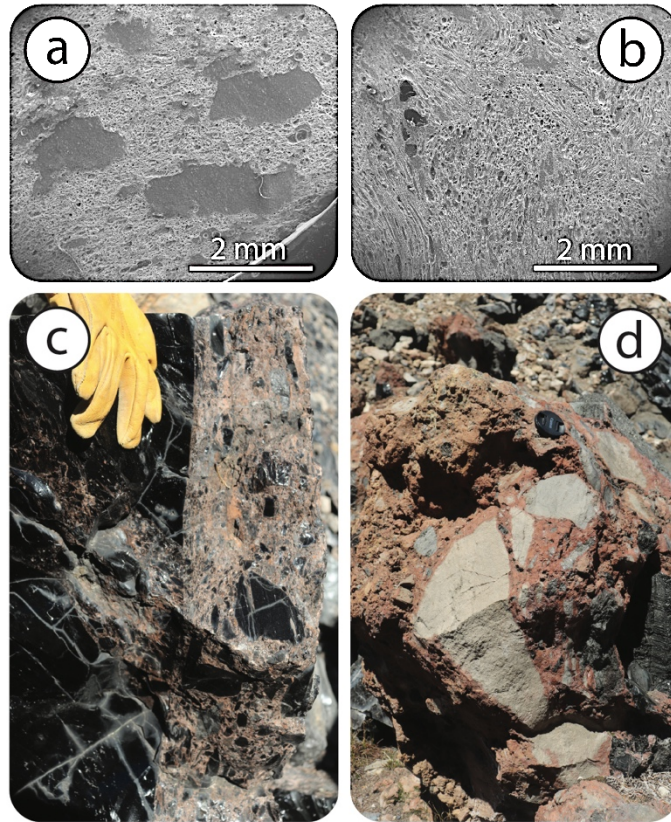
## 5.2 UP1

We interpret the Newberry 640 CE Big Obsidian event to move towards a pulsatory, Vulcanian-like explosive activity starting with phase UP1. Multiple packages of characteristically similar lapilli are sandwiched among ash layers, evidencing an intermittently stable plume or series of discrete plumes. We estimate the total amount of magma expelled during the UP phase (including both UP1 and UP2) to be 0.54 km<sup>3</sup> (non-DRE). Near vent pits exhibit at least seven ash layers (Kuehn, 2002). Assuming ash layer divide discrete pulses, we estimate the amount of magma expelled in each pulse is thus estimated to be ~0.05-0.1 km<sup>3</sup> non-DRE. Vulcanian eruptions are comparable to sub-Plinian eruptions in terms of dispersal area; however, they have tend to have more fine material, which we do see here (Fig. 6; Walker, 1973; Cas and Wright, 1986; Fig. 6).

Rust and Cashman (2007) interpret the first ash layer above LP to be from plug material and welded fallback, while subsequent ash layers would derive from density currents shed from a somewhat instable though still vigorous sub-Plinian column. They interpret lapilli layers in UP1 to preserve episodes of vent widening given that 1) lapilli layers in the UP coarsen upwards (which we also see in proximal and medial pits) and 2) there is an increase in the variability of textured obsidian during this phase. Although the first ash layer at the LP-UP1 boundary described by Rust and Cashman (2007) is not preserved in our pits, we find the consistency in componentry among following ash layers to suggest similar eruption dynamics throughout the UP1 (Fig. 4). We thus interpret all the >7 reversely graded lapilli-dominated layers and associated overlying ash-dominated layers to represent Vulcanian-like episodes. We note an increase in the quantity of lithics in the lapilli-dominated layers of UP1 (14-22 wt%) compared to LP (<12 wt%; Fig. 5).

Phase	LP	UP1	UP2
Packages	1	1-7	1
Volume	0.88 km <sup>3</sup> non-DRE		0.54 km <sup>3</sup> non-DRE
Plume Height	18 km		18 km or less
Eruptive style	Stable subplinian		Vulcanian
Componentry	Least obsidian	More obsidian	Most obsidian, lithics Least pumice
GSD	Largest grains Lapilli-dominated Sigmoidal GSD	More ash-sized grains	AND Bimodal split: one peak at ash, one at lapilli
Density	Least dense (m: 0.59, 0.63 g cm <sup>-3</sup> ) Least spread (std: 0.125, 0.1)	More dense (m: 0.64, 0.73 g cm <sup>-3</sup> ) More spread (std: 0.14, 0.14)	Most dense (m: 0.72 g cm <sup>-3</sup> ) Widest spread (std: 0.16)
Pumice Texture	Most sintered (up to 50%) Most tubular (~50-60%)	Less sintered Less tubular	Least sintered (down to 0%) Least tubular (down to 35%)
Obsidian Textures	Black (60-80 wt%) Grey, microlite-rich (20-40 wt%)	Variable (all ~10-30 wt%) Black, grey, clear, xenolith- and pumice- bearing	Black (~65 wt%) Grey (~20 wt%) Xenolith-bearing (~15%)

**Table 1** Summary of physical attributes of juvenile products of the Big Obsidian period by phase.



**Figure 7** Pictures of internal and external texture. SEM images of a typical pumiceous clast from a) the LP and b) the UP. Found on the Big Obsidian Flow <1 km from the interpreted vent (Kuehn, 2002), composite bombs (Schipper et al., 2021) include c) flow tuffisite, in which the ash-filled veins choked with lithics and pumiceous clasts directly contacts dense, black glass, and d) Ballistic tuffisite, in which an ash matrix sinters together blocks (Tuffen and Dingwell, 2005; Castro et al., 2014). Camera lens cap for scale in d.

Ash layers contain even higher amounts of lithics (20-28 wt%), which could be from energetic plug ruptures that would finely fragment material and incorporate higher amounts of degassed magma (Wright et al., 1980; Cas et al., 1987). The slight increase in pyroclastic obsidian content in UP (~1 wt% in lapilli-dominated layers, 3-6 wt% in ash layers; Fig. 5) compared to LP also suggests that amalgamation and advanced sintering of

ash occurs in parts of the conduit (Gardner et al., 2017), with more conduit erosion occurring during UP compared to LP.

Fewer tubular pumices on average are also found in the UP compared to the LP, which could result from a switch to a top-down style of fragmentation in which sudden depressurization of magma following plug rupture drives rapid volatile exsolution, soon followed by magma fragmentation (i.e., Vulcanian style; e.g. Wright et al., 2007; Druitt and Kokelaar, 2004; Giachetti et al., 2010). Such fragmentation would result in less time for magma to be sheared prior to quench as compared to during continuous rapid ascent as during sub-Plinian activity. This interpretation would also explain the lower median porosity of pumice lapilli in UP1 (70-74%) compared to LP (74-75%) observed at pit KT-10A (Fig. 5; Mueller et al., 2011). However, the decrease in the proportion of tubular pumice lapilli may also be a consequence of a lower surface area/volume ratio of the magma to the conduit if the upper latter had enlarged as compared to during the sub-Plinian activity of LP (Ohashi et al., 2021), as suggested by the increase in lithics and obsidian pyroclasts in UP compared to LP.

Bimodal grain size distributions are often interpreted as evidence for ash aggregation (Miwa et al., 2020; Janebo et al., 2018; Carey and Sigurdsson, 1982). Here, however, the bimodality is evident not in fine ash (fines peak often around  $0.03125 < d < 0.125$  mm), but in the coarse ash fraction ( $0.5 < d < 2$  mm) for lapilli-dominated layers (Fig. 6b). The bimodality of mass distribution in these UP layers is thus interpreted to evidence secondary fragmentation by interparticle disruptive collisions, which impact more cm-scale clasts and whose frequency increases with depth of fragmentation (Dufek et al., 2012). Secondary fragmentation may have been amplified by an increase in welded

fallback and agglutinated ash on conduit margins. Such lateral ash build-up would lead to the creation of a nozzle in the upper part of the conduit that would engender interparticle collisions (see Fig. 2b-c in Wadsworth et al., 2020). This interpretation is consistent with the sudden presence in UP1 of obsidian sintered to xenoliths and pumiceous clasts (see our Fig. 5 and Fig. 2 in Rust and Cashman, 2007), and the increase in black obsidian relative to other types over the course of the UP1 (Fig. 2 in Rust and Cashman, 2007).

### 5.3 UP2

We interpret the UP2 section as one last Vulcanian event capturing the transition in eruption dynamics prior to effusive-only behavior and the emplacement of the Big Obsidian Flow. Compared to UP1, the sharp increase in obsidian (>8 wt% compared to ~1 wt% in UP1 at KT-10A) and slight increase in lithic content (27 wt% in UP2 compared to 14-22 wt% in UP1) captures a final efficient explosion that excavated more wall material relative to magma (Fig. 5). Lapilli are also the most variably dense (Figs. 5, 6a), perhaps resulting from magma fragmented over a wider range of conduit depths (Clarke et al., 2007). The bimodal GSD suggests high secondary fragmentation as would result from a highly collisional regime.

As bubbly magma was fragmented during UP2, co-effusion of degassed lava may have begun. Wadsworth et al. (2020) proposed that pervasive and advanced ash-scale sintering can ultimately result in effusive behavior, arguing that evidence for such a process is preserved in obsidian pyroclasts and tuffisites, ash-filled veins that facilitate degassing. In UP2, the final phase of the 640 CE eruption of Newberry, we observe a marked increase in obsidian content at all sizes (Figs. 4, 5). According to Rust and

Cashman (2007), these obsidian pyroclasts are also predominantly black obsidian whose volatile contents remain consistent with shallow depth formation (Rust and Cashman, 2007). The overall increase in obsidian, as well as the relative lack of xenocrystic material preserved in obsidian, suggests a marked build-up of obsidian forming laterally farther from conduit margins. This obsidian had more time to evolve texturally before excavation (Gardner et al., 2017). It is thus not unreasonable that UP2 occurred while the Big Obsidian Flow was already partly emplaced. We find ballistic and flow obsidian tuffisites <1 km from the interpreted vent (Kuehn, 2002) on the Big Obsidian Flow (Fig. 7), which would have been ejected during UP2, and which is consistent with this hypothesis. Thus, could effusive behavior have begun, with tuffisitic veins increasingly promoting degassing to facilitate the switch to final effusive behavior (Tuffen et al., 2003; Wadsworth et al., 2020). We additionally note finding breadcrust bombs <2 km due east from the vent, common products of Vulcanian explosions (Wright et al., 2007; Giachetti et al., 2010).

#### *5.4 The continuity of the 640 CE eruption at Newberry*

We summarize our interpretation of the continuity of the 640 CE eruption of Newberry in Figure 8.

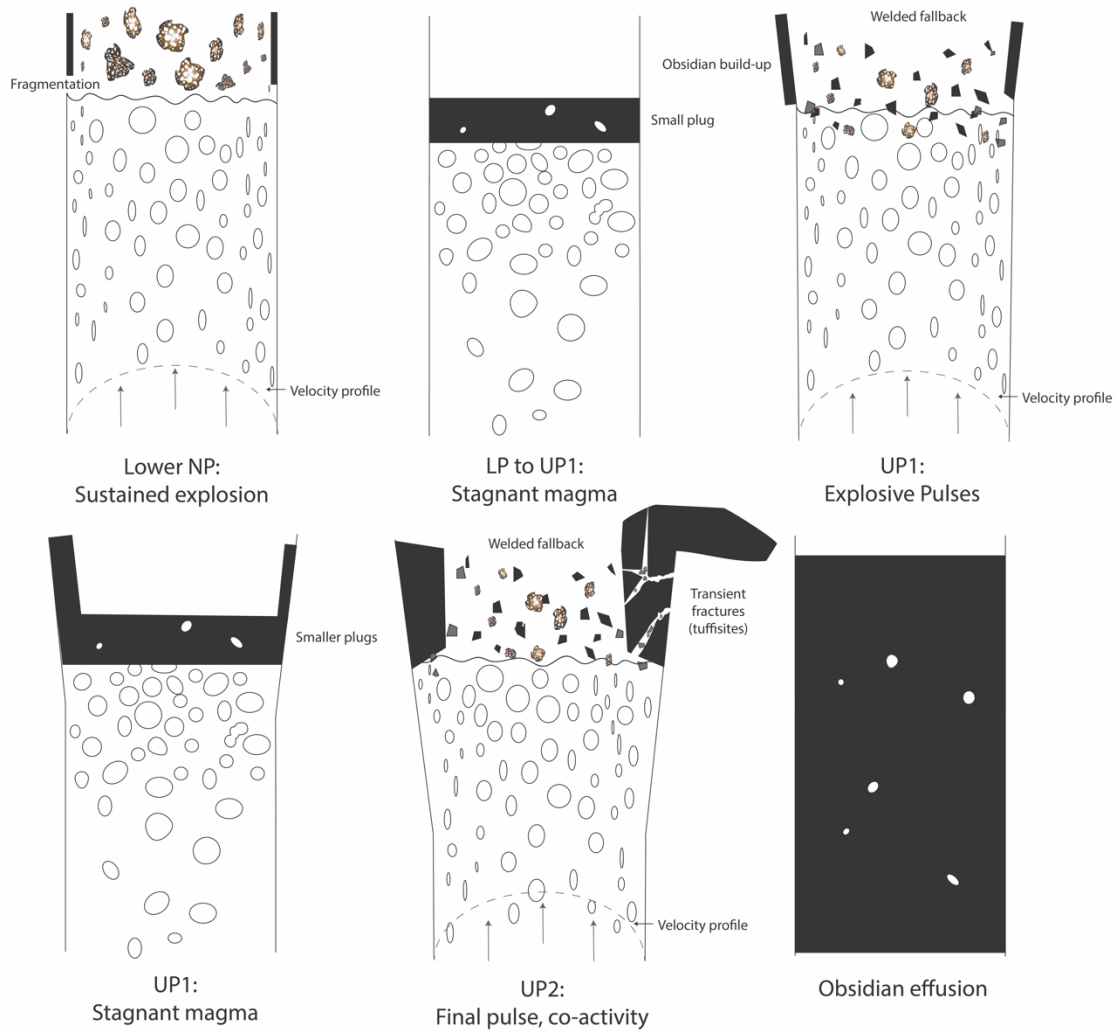
Given the deposit extent (Fig. 1), predominance of pumiceous lapilli (Fig. 2), and grain size distribution (Fig. 6b), we interpret the LP to represent a relatively stable sub-Plinian plume after initial vent widening (Fig. 8a). The consistently high and relatively constant porosity of juvenile porous material, low amount of obsidian and lithics (Fig. 4), and homogeneity in obsidian texture (Rust and Cashman, 2007) additionally suggest

relatively stable conduit conditions. The higher porosity (Fig. 6a) and population of cm-scale bubbles in lapilli (Fig. 7a) can be tied to shallow fragmentation that would have allowed more time for bubbles to grow. Shallow fragmentation is also consistent with volatile content of obsidian pyroclasts found in the LP (Rust and Cashman, 2007).

Aggregation and sintering of ash occur on the conduit edges, above the level of fragmentation (Gardner et al., 2017; Wadsworth et al., 2020), but excavation of these syn-eruptively formed obsidian is limited during this first phase of the eruption.

Following a cessation in surface activity during which magma slowly rises and degasses within the conduit (Fig. 8b), the eruption changes to be more pulsatory in nature as evidenced by the multiple packages of lapilli sandwiched by ash layers. Ash layers may derive from small plugs of degassed magma (UP1; Figs. 2, 8c). This succession of Vulcanian-like pulses ejected a total volume of  $\sim 0.5$  km<sup>3</sup> of tephra wherein each pulse is  $< 0.1$  km<sup>3</sup>. Breadcrust bombs found  $< 2$  km from the vent support a Vulcanian style of ejection (Wright et al., 2007; Giachetti et al., 2010). Reverse grading of lapilli layers (Fig. 2), variability in tubular lapilli (Fig. 5), incorporation of xenocryst-bearing obsidian pyroclasts (Rust and Cashman, 2007), and relative increase in obsidian pyroclasts (Fig. 4) all suggest phases of conduit opening and excavation wherein obsidian was largely scraped from the margins where it had formed after initial fragmentation during the earlier phase of the eruption (LP and earlier UP1 events). Denser lapilli (Fig. 6a) may derive from conduit margin fallback (Kennedy et al., 2005) and the sampling of variably-degassed magma during Vulcanian pulses. The shift of the shape of the GSD to a bimodal distribution (Fig. 6b) may be the result of enhanced secondary fragmentation from





**Figure 8** Conduit model of the Subplinian eruption, which began in a sustained fashion, transitioned to pulsatory explosions, and finished with lava effusion following concurrent explosive-effusive activity.

increased interparticle collisions from such fallback and/or a narrowing upper conduit from agglomerated ash (Fig. 8b).

Co-effusion of lava likely began during UP2, the final explosive event (Fig. 8e). Tuffisitic material preserves juxtaposed porous and dense veins (Fig. 7c, d), indicating degassing promoted through obsidian-plastered conduit margins. In UP2, the overall

amount of obsidian drastically increases (Fig. 4), particularly black obsidian (Rust and Cashman, 2007), suggesting a marked build-up of such sintered material that had time to texturally relax (Gardner et al., 2017) and could have ultimately resulted in lava effusion. Reverse grading (Fig. 2; Kuehn, 2002; Rust and Cashman, 2007), a sigmoidal GSD typical of secondary fragmentation (Fig. 6b), and a further increase in lithics compared to UP1 (Fig. 4c) are additionally consistent with the excavation of a conduit refilling in between explosive events. Following efficient degassing by tuffisitic pathways and excavation of the conduit, the eruption ultimately transitioned to predominantly effusive behavior, and the Big Obsidian Flow was emplaced (Fig. 8f).

##### *5.5. Comparison with the 2011-2012 eruption of Cordón Caulle*

The eruption of Cordón Caulle in 2011-2012 began with a Plinian explosion that erupted rhyolitic tephra ~14 km into the atmosphere above the summit (Collini et al., 2012). The plume fluctuated between 3-10 km high for the next 7-9 days (Collini et al., 2012). Ballistic ejection began after 3 days and continued with column-scale tephra dispersal ~6 days (Pistolesi et al., 2015). For the last two days, ballistic intensity spiked, after which hybrid explosive-effusive activity started with lava emerging from the same vent as that which produced tephra , about 10 days after the onset of the first Plinian explosion (Castro et al., 2012; Silva Parejas et al., 2012; Castro et al., 2013). We interpret the 640 CE eruption of Newberry Volcano to have proceeded similarly judging by the intensity of the eruption (initial plume height: ~18 km; Rust and Cashman, 2007), its continuity, and the similarity in sedimentological characteristics of the erupted products. The 2011 Cordón Caulle eruption, like that of Newberry Volcano, has an increase in ash-

dominated layers, heterogeneous juvenile clasts (e.g., for Cordón Caulle, seen in banded pumice, crystals) and obsidian, and denser lapilli in the latter half of the explosive phase. Products for both eruptions are also all interpreted to result from a single vent (MacLeod et al., 1995; Kuehn, 2002). Based on the similitude between the two eruptions, we thus surmise that the predominantly explosive phase of the 640 CE eruption of Newberry Volcano (LP, UP1, and UP2) lasted a few tens of hours to several days at a maximum.

Wadsworth et al. (2020) and Schipper et al. (2021) point to sintering of recently-fragmented juvenile material as driving the transition in activity from explosive to hybrid to effusive. Schipper et al. (2021) investigated the textures of composite bombs produced during the change from pure explosive to hybrid activity at Cordón Caulle. These bombs capture high-energy fragmentation as 1) their matrix is ash-dominated with components of the bombs potentially deriving from finely fragmented material (Gardner et al., 2018; Giachetti et al., 2021; Wadsworth et al., 2021) and 2) higher energy is required to fragment the sintered material, as it is less porous (Spieler et al., 2004). Schipper et al. (2021) thus suggest explosivity was self-extinguishing, wherein efficient fragmentation enhanced the efficacy of sintering until effusive behavior prevailed. However, they note that this does not mean that extrinsic properties did not affect the transition (e.g., magma ascent rate; Cassidy et al., 2018). At Newberry, we envision a similar self-extinguishing of eruptive behavior, wherein an obsidian-clad conduit permits hybrid activity until a final energetic burst leads to final obsidian effusion (i.e., the Big Obsidian Flow itself). We find ballistic breadcrust bombs in UP2 as would result from energetic Vulcanian plug ruptures, while composite bombs on the obsidian flow evidence a high-energy, pyroclastic origin of obsidian. Volatile contents in the UP2 preserve a very shallow depth

of formation of products (as shallow as 0.2 km below the surface; Rust and Cashman, 2007).

## **6. Conclusion**

Based on sedimentological characteristics and physical aspects of juvenile products, we interpret the explosive phase of Newberry Volcano's 640 CE explosive phase to have transitioned from a relatively-stable sub-Plinian phase to Vulcanian-like pulses. The last Vulcanian event probably occurred at the same time as the onset of the final effusion of degassed lava. The progression of the eruption is similar to that of the only two witnessed eruptions of crystal-poor rhyolitic magma at Chaïten and Cordón Caulle (Chile; 2008 and 2011-2012, respectively), suggesting a commonality in eruption progression for silicic crystal-poor eruptions. Works in progress at Medicine Lake (Glass Mountain eruption; crystal-poor rhyolite; Giachetti and Shea, in prep) and Mount Mazama-Giiwas (Cleetwood eruption; Wiejaczka and Giachetti, in prep) are consistent with this observation. When interpreted through the lens of recent advanced in conduit studies (Gardner et al., 2017; Cassidy et al., 2018 and references therein; Wadsworth et al., 2020; Schipper et al., 2021; Ohashi et al., 2021), these new data, together with previous work on the same eruption (Gardner et al., 1998; Kuehn, 2002; Rust and Cashman, 2007), support the interpretation that Newberry Volcano was modulated by cycles of ash agglomeration, sintering, and excavation along conduit margins. Co-explosive-effusive behavior may be more prevalent than previously thought, and its record may only be evident by thoroughly examining both dense and porous endmembers of juvenile tephra.

## 7. Bridge

The past two chapters have focused on eruptions at Cascade Volcanoes – those of Medicine Lake Volcano and Newberry Volcano. Chapter IV uses samples from these same eruptions and contextualizes them with those at Crater Lake. While Medicine Lake Volcano and Newberry Volcano had eruptions similar in scale, those of Crater Lake were significantly more voluminous. Still, despite differences in eruptive scale, all eruptions are highly silicic and produced porous pyroclasts that preserve textural evidence of inner volcanic processes. Chapter IV rethinks a common viewpoint on the formation of pyroclasts – namely, that they are assembled and don't simply result from one fragmentation and cooling event. Nay, they are the products of potentially myriad fragmentation, collision, and agglomeration events. Such results, as with those of the other studies, has implications for our view of pyroclasts in the greater context of volcanic processes.

## CHAPTER IV

### THE PRODUCTS OF PRIMARY MAGMATIC FRAGMENTATION FINALLY REVEALED BY PUMICE AGGLOMERATES

This manuscript was published in *Geology* under the title, “The products of primary magmatic fragmentation finally revealed by pumice agglomerates.” The manuscript was co-authored with T. Giachetti, J. Wiejaczka, J. Gardner, J. Watkins, and H. Wright. T. Giachetti, K.R. Trafton and J. Wiejaczka gathered and analyzed data. T. Giachetti wrote the manuscript, and all authors provided revisions and rigorously debated the science.

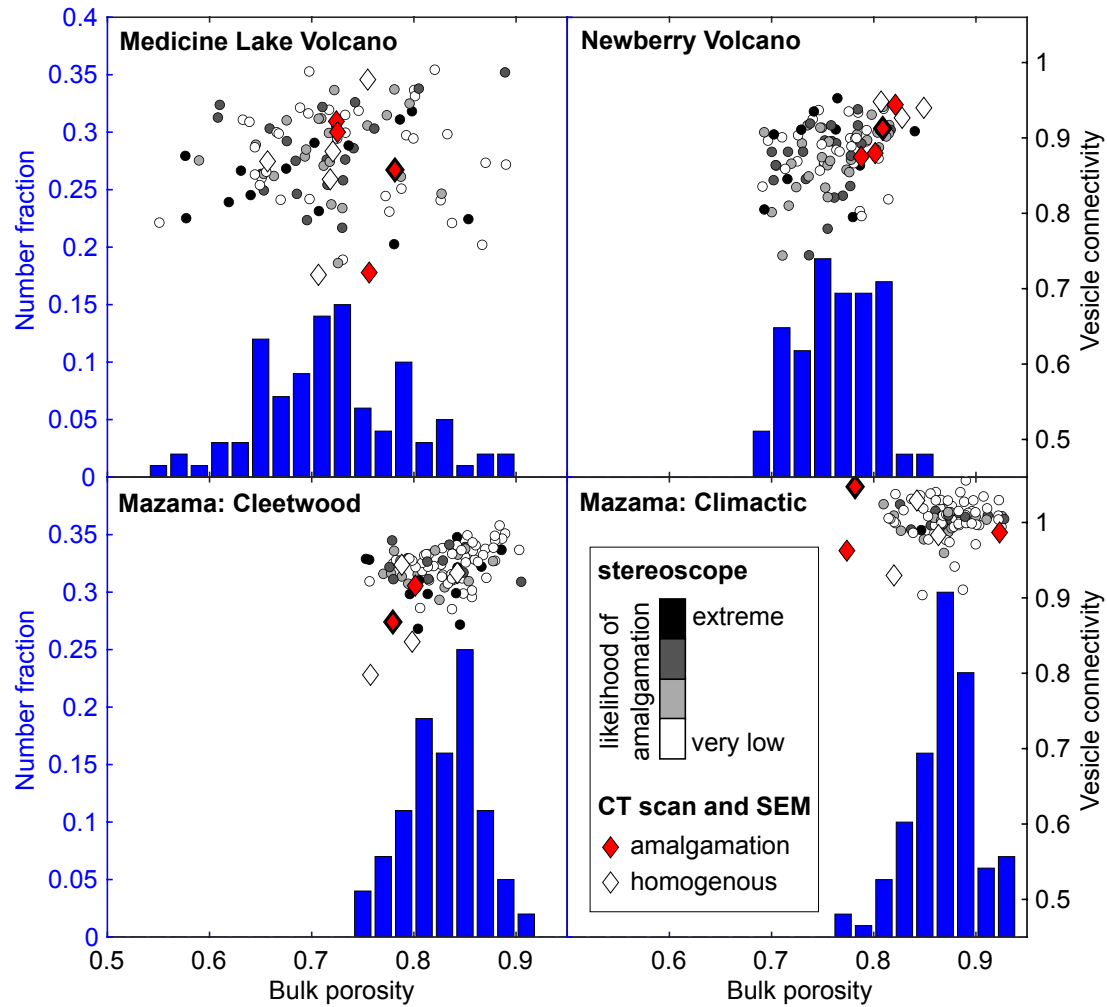
#### **1. Introduction**

Explosive volcanic eruptions of silicic magmas result from fragmentation of magma below Earth’s surface into pyroclasts ranging in size from ash to lapilli and blocks ash. During magma ascent, decreasing pressure forces gas-saturated magma to nucleate bubbles of supercritical fluid. Bubbles then grow by the diffusion of volatiles from the melt and the expansion of the exsolved vapor phase, causing an increase in magma porosity, magma acceleration, and further degassing. Simultaneously, as viscous stresses in the melt impede bubble growth, vapor pressure therein increases (Gonnermann and Manga, 2007). When bubble overpressure exceeds the tensile strength of the surrounding melt and/or if the expanding melt is subjected to a critical strain rate (Dingwell, 1996; Zhang, 1999; Papale, 1999), magma explosively fragments into pyroclasts that range from submicron (ash) to macroscale (blocks) in size.

Fall deposits from explosive Plinian eruptions of silicic magmas have a size distribution different from that expected for a single fragmentation event (Kaminski and Jaupart, 1998). The size distribution of the products of rock fragmentation invariably follows a power law  $N = \lambda d^{-D}$ , where  $N$  is the number of particles greater than size  $d$ ,  $\lambda$  is a scaling factor, and  $D$  is the power law exponent (fractal dimension). For a variety of experimentally fragmented geological objects, fractal dimensions are always  $< 3$  and in most cases in the range  $2.5 \pm 0.3$  (Turcotte, 1997; Kaminski and Jaupart, 1998). By contrast, fallout deposits of silicic Plinian eruptions have total grain size distributions that follow a power law distribution with fractal dimension  $> 3$  ( $D = 3.4 \pm 0.3$ ; Kaminski and Jaupart, 1998; Rust and Cashman, 2011; Pioli et al., 2019; Carazzo et al., 2020). The difference in  $D$  values between experimental and natural fragmentation products has been explained by secondary pyroclast fragmentation in response to thermal stresses during decompression, and/or disruptive inter-particle collisions and abrasion in the conduit and volcanic plume (Dufek et al., 2012; Jones et al., 2017). This  $D$  value differential is at present an unconstrained metric of secondary fragmentation: as the true size distribution of primarily-fragmented pyroclasts remains unknown, so too does the degree to which secondary fragmentation impacts pyroclast size and shape distributions. However, new textural observations of subplinian and Plinian lapilli reported here, interpreted considering recent studies into the origin of obsidian pyroclasts (Gardner et al., 2017; Watkins et al., 2017), indicate that some pumice pyroclasts form by post-fragmentation amalgamation of ‘protopyroclasts’ prior to secondary collisional processes.

## 2. Methods

We made new textural observations of pumice lapilli from four highly silicic subplinian and Plinian eruptions at Medicine Lake Volcano (USA; 1060 C.E. Glass



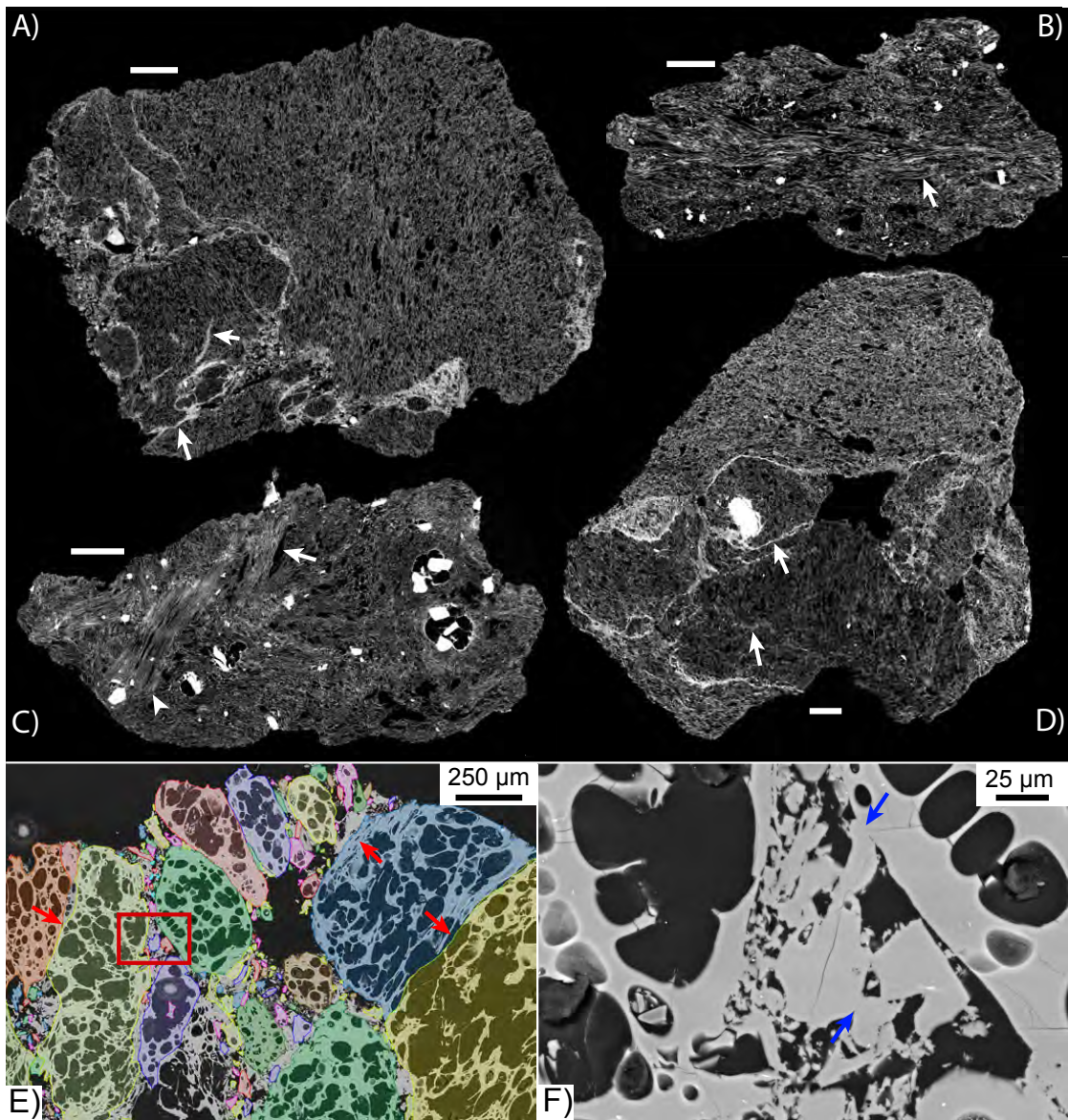
**Figure 1:** Pyroclast bulk porosity distribution (left) and ratio of connected to bulk porosity (i.e., connectivity; right) for each studied eruption. Disc color represents the likelihood of each pyroclast to be an amalgamation of protopyroclasts as based on observation under a stereomicroscope. For clasts analyzed by CT (diamonds), color indicates whether the clast exhibits CT/SEM evidence of amalgamation. The red diamond with thicker edge corresponds to the clast shown in Figure 2 for each eruption.



Mountain eruption; Heiken, 1978), Newberry Volcano (USA; 700 C.E. Big Obsidian Flow eruption; Kuehn, 2002), and Mount Mazama/Giiwas (USA; ~5,750 B.C.E. Cleetwood and climactic eruptions; Young, 1990; Bacon, 1983). These explosive eruptions ejected ~0.1 km<sup>3</sup> (explosive phase of the Big Obsidian Flow and Glass Mountain eruptions) to ~60 km<sup>3</sup> (climactic phase of the ~5,750 B.C.E. eruption of Mt Mazama) of crystal-poor rhyodacitic to rhyolite magma. For each eruption, 100 juvenile pumice lapilli, collected from single beds, were analyzed for their size and porosities (bulk and connected; see Appendix C). In all suites, some pyroclasts exhibit distinct surficial textures from inter-clast amalgamation, visible under stereomicroscope. The proportion of these clasts was determined, and 28 variably-textured lapilli, wherein 6 to 9 (some exhibiting amalgamation-like textures, some not) were arbitrarily chosen from each suite, were then analyzed by X-Ray Computed Tomography (CT; Appendix C).

### **3. Porosity and External Texture of the Lapilli Suites**

The bulk porosity and the ratio of connected to bulk porosity (connectivity) of the pyroclasts suites are roughly positively correlated (Fig. 1). Moreover, median bulk porosity and connectivity increase with erupted volume and mass discharge rate, from 72±7% and 0.88±0.06, respectively, for Medicine Lake, to 76±4% and 0.89±0.04 for Newberry, to 83±4% and 0.94±0.03 for the Cleetwood phase of Mazama, and 87±3% and 1.00±0.03 for the climactic phase of the Mazama eruption. The bulk porosity and connectivity of all four suites of pyroclasts are typical of subplinian and Plinian lapilli in general (Mueller et al., 2011; Colombier et al., 2017). All suites contain pumice lapilli that have surficial textural evidence of amalgamation. The presence of such textures



**Figure 2:** (A-D) Slices taken in CT stacks of pumice lapilli from (A) Newberry (#6), (B) Cleetwood eruption of Mazama (#11), (C) Climactic eruption of Mazama (#4), (D) Medicine Lake (#86D). White arrows highlight a few boundaries between textural domains, some of which appear more subdued, usually closer to the center of the clasts. White scale is 2 mm. (E-F) SEM images of a sample from Medicine Lake Volcano (#8) showing partly sintered particles. The red rectangle in (E) shows the location of (F). In (E), red arrows indicate flattened voids in the rim of individual protopyroclasts. All easily identifiable protopyroclasts have been colored for easier visualization only. In (F), blue arrows point to examples of partly sintered ash particles.

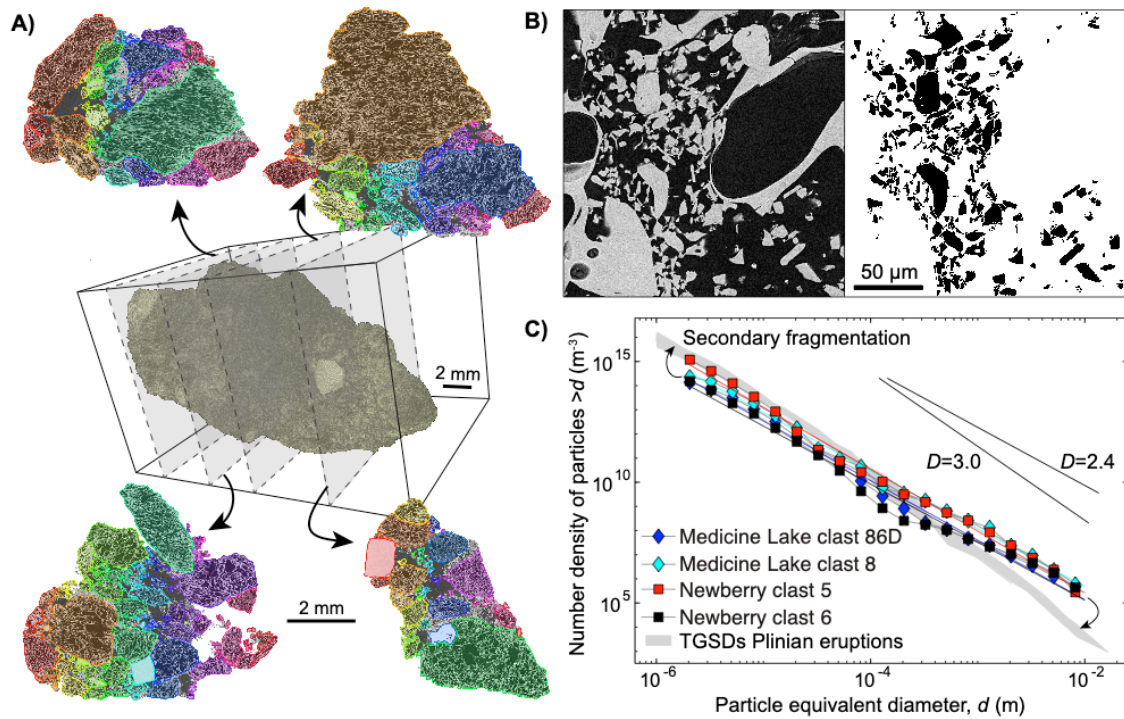
does not depend on the size, porosity, or connectivity of the pyroclast (Fig. 1). However, the overall proportion of extremely-likely to most-likely amalgamated clasts (see Supplemental Material for detail) decreases with erupted volume and mass discharge rate, from 17-37% in the Medicine Lake and 17-39% in the Newberry suites, to 14-25% in Cleetwood and 5-19% in the climactic phase of Mazama.

#### **4. Identifying Protopyroclasts**

All seemingly-amalgamated pyroclasts and over a third (5/14) of those appearing texturally homogeneous consist of juxtaposed domains with variable porosities, vesicle sizes, and vesicle orientations when viewed under CT (Fig. 2). These domains range in size from a few microns to >1 cm. The contrast in porosity and/or vesicle sizes and orientations between textural domains are typically sharp (Fig. 2a, d), but more subtle differences in vesicle texture between domains exist and are trackable in 3-D CT scans (e.g., Fig. 2b-c). Single pyroclasts can contain several to thousands of discrete domains (Fig. 2). Most domains  $\lesssim$ 30 microns are almost all entirely dense (Fig. 2e-f). Boundaries between some larger domains form tomographically bright bands a few microns to tens of microns in thickness (Fig. 2 a, d). Scanning Electron Microscope (SEM) images taken at higher resolution show that these boundaries include partly sintered ash in between domains (Fig. 2e-f) and/or densified domain rims in between which some pores are flattened (Fig 2d). We note that in most CT-scans, boundaries between domains are more easily identifiable towards the outskirts of the clast.

Using SEM and CT image analysis, we manually delineated textural domains from four pumice lapilli (two from Newberry, two from Medicine Lake; Fig. 3a-b) for

which the boundaries between domains are clear enough at all sizes for the latter to be manually separated on the images. Although contrasting textural domains are apparent on the CT images of the Mazama pyroclasts (Fig. 2b,d), exact boundaries are too diffuse to delineate without significant bias; as such, the exercise was thus not carried out for these pyroclasts. This approach allows us to quantify the size



**Figure 3:** Particle size distributions of protopyroclasts. (A) 3D rendering of CT slices. On each slice shown, protopyroclasts were manually individualized and highlighted using different colors. (B) Smaller protopyroclasts individualized on SEM images (raw image left, binarized image at right). Protopyroclasts appearing isolated are sintered in the third dimension. (C) Protopyroclast size distributions obtained in four clasts from Medicine Lake and Newberry volcanoes compared with Total Grain Size Distributions (TGSD) of four Plinian eruptions (Rust and Cashman, 2011). Best fits to Plinian TGSDs using a power law distribution give a fractal dimension  $D=3.0-3.3$ , whereas protopyroclast size distributions are best fit with  $D=2.4-2.6$  (2.40 and 2.56 for Newberry #6 and #5; 2.40 and 2.47 for Medicine Lake #8 and #86D).

distribution of textural domains from  $\sim 3 \mu\text{m}$  up to the size of the lapilli themselves (11-31 mm). In all four cases, the size distribution of textural domains defines a power law distribution that is best fitted using an exponent of 2.4-2.6 (Fig. 3c). Prior to amalgamation, these textural domains thus have a size distribution that matches that predicted by fragmentation experiments conducted on a variety of geological objects (fractal dimension of  $2.5 \pm 0.3$ ; Turcotte, 1997; Kaminski and Jaupart, 1998).

Porous volcanic pyroclasts, when rapidly decompressed in a shock tube apparatus, fragment if the change in pressure exceeds a threshold of approximately  $\sigma/\phi$ , where  $\sigma \approx 1$  MPa is the tensile strength of the silicate melt and  $\phi$  is the porosity of the magma (Spieler et al., 2004). The fractal dimension of these products typically falls within a narrow range of  $2.4 \pm 0.2$  (Alidibirov and Dingwell, 1996; Kueppers et al. 2006). We thus interpret the textural domains highlighted in Fig. 2 to be protopyroclasts, the direct products of primary magmatic fragmentation in the conduit. Because their porosity and connectivity are typical of subplinian and Plinian pumice lapilli (Fig. 1; Rust and Cashman, 2011; Colombier et al., 2017), and none of the 400 clasts analyzed have obsidian edges, amalgamated pyroclasts are highly unlikely to derive from tuffisitic infill. Instead, we posit that these protopyroclasts were preserved by amalgamating and partly sintering inside the conduit during and/or immediately following primary fragmentation (Fig. 3). The size distributions of silicic Plinian fallout deposits, which have a fractal dimension of  $3.4 \pm 0.3$  (Fig. 3c; Rust and Cashman, 2011; Kaminski and Jaupart, 1998; Pioli et al., 2019; Carazzo et al., 2020), must thus be largely overprinted by amalgamation and by secondary fragmentation in the conduit and the plume, and so can

only give limited insight into primary magmatic fragmentation. The number density of protopyroclasts larger than  $\sim 1 \mu\text{m}$  in the four pumice lapilli analyzed is  $\sim 10^{15} \text{ m}^{-3}$  (Fig. 2c), nearly an order of magnitude less than the number density of pyroclasts  $\geq 1 \mu\text{m}$  ultimately produced by Plinian eruptions (Rust and Cashman, 2011). This discrepancy likely arises from secondary fragmentation galvanizing the production of smaller pyroclasts in the conduit and plume.

## 5. Sintering of Protopyroclasts

For protopyroclasts to amalgamate, they must collide at low enough energies and stick together (Dufek et al., 2012). We believe this occurs during the fluidization of the packed beds of pyroclasts. This is a zone in between the unfragmented magma below and the fully fluidized gas-pyroclast mixture above, in other words, just at/above the fragmentation zone (Darteville and Valentine, 2007). In that zone, both the density of particles and their acceleration are high, but acceleration slightly differs for particles of different size, promoting low-energy collisions. As melt viscosity increases during ascent post-fragmentation due to permeable outgassing and diffusive water loss (Rust and Cashman, 2011), so too does the sintering timescale. Pyroclasts thus have the highest chance to collide, amalgamate, and partially sinter in the vicinity of the fragmentation zone. Obsidian pyroclasts from the 1340 C.E. North Mono eruption (Mono Craters, CA, USA) formed by cycles of fragmentation, sintering/suturing, and annealing/relaxation over *varying depths on the conduit wall* (Gardner et al., 2016; Watkins et al., 2017). We propose that this process also occurs *inside the gas-pyroclast mixture across the conduit*,

wherein limited residence time during rapid final ascent limits maturation and densification of the aggregates, preserving protopyroclasts' initial sizes and textures.

Sintering after initial amalgamation must rapidly occur between fragmentation and quench, over the course of ~10-60 s (Gardner et al., 1996). In the absence of confining pressure, the sintering timescale of randomly packed, monodisperse spherical particles is given by (Wadsworth et al., 2019)

$$\tau \approx \frac{\mu R}{\sigma}, \quad [1]$$

where  $\tau$  (s) is the sintering time scale,  $\mu$  (Pa s) is viscosity of the melt,  $R$  (m) is particle radius, and  $\sigma$  is surface tension. Sintering between protopyroclasts appears limited, usually occurring over length scales of  $\sim 10^{-5}$  m or less (Fig 1e-f). Assuming disequilibrium degassing, rhyolitic melt viscosity at fragmentation is  $\sim 10^6$  Pa s (Gonnermann and Houghton, 2012; Hajimirza et al., 2021), a reasonable value for a wide range of silicic magmas (Gardner et al., 1996). For a surface tension of  $\sim 0.2$  N/m (Bagdassarov et al., 2000) and in the absence of confining pressure,  $\sim 10^{-5}$  m protopyroclasts can sinter above fragmentation within  $\sim 50$  s, prior to quench (Eq. [1]).

## 6. Implications

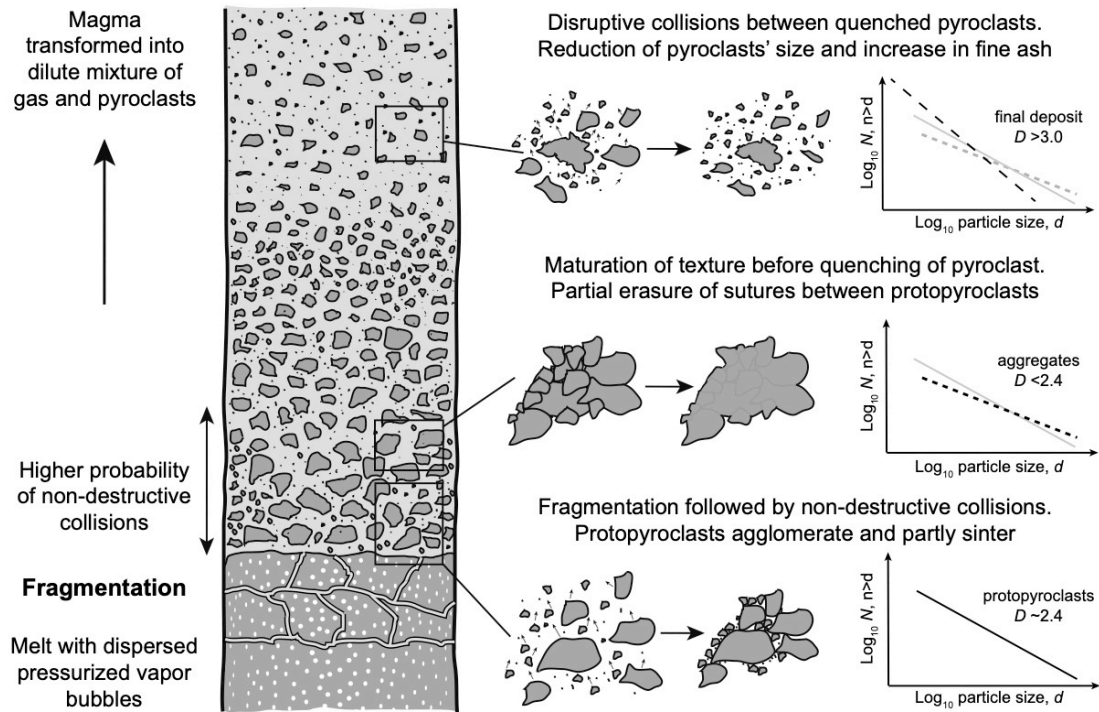
We examined typical pyroclasts from four subplinian and Plinian eruptions that span more than three orders of magnitude of erupted ejecta by volume and more than two orders of magnitude of mass discharge rates. We postulate syn-/post-fragmentation amalgamation and partial sintering of protopyroclasts in the conduit is widespread and has been previously overlooked or interpreted differently. Highly silicic pumice fall

agglomerates have only been reported once to the best of our knowledge (Santorini; Taddeucci and Wohletz, 2001), yet contiguous heterogeneous textures at the sub-mm scale have been widely documented in highly silicic tephra (e.g., Figs. 1A and 4A, Wright and Weinberg, 2009; Fig. 9, Schipper et al., 2013; Fig. 15, Pistolesi et al., 2015). While they are usually interpreted as resulting from heterogeneities in material properties and/or localized degassing, these textures may be from syn-/post-fragmentation amalgamation and partial sintering of protopyroclasts, as described herein. Additionally, Newberry ( $\sim 10^7$  kg/s, Gardner et al., 1998) and Medicine Lake pyroclasts preserve these textures *more often* and *more distinctly* than do those from Mazama ( $10^8$ - $10^9$  kg/s; Young, 1990). This observation could be an indication that the fluidization of packed beds of protopyroclasts at fragmentation during more explosive eruptions is more efficient, leaving less time for mixing and amalgamation of protopyroclasts with highly contrasting textures.

Magmatic fragmentation converts potential energy from the compressed gas inside bubbles into kinetic energy and surface energy of fractures in the melt (Grady, 1982). The size distribution of fragmentation products should reflect eruption explosivity, wherein the fractal dimension of the fragment size distribution increases with the potential energy for fragmentation (Kueppers et al., 2006). However, the unconstrained overprint of secondary fragmentation on the final size distribution of tephra renders this task challenging. The textures described here provide a framework for quantifying the size distribution of primary magmatic fragmentation products, and so could be used to obtain the potential energy for fragmentation (Yew and Taylor, 1994; Kolzenburg et al., 2013). These textures also show that, contrary to what is claimed at this time, studies of



the size and texture of the final pyroclasts (rather than individual protopyroclasts) may tell a post-, rather than pre-fragmentation story.



**Figure 4:** Diagram illustrating primary and secondary fragmentation processes occurring within the conduit, and their effects on pyroclast grain size distributions. The diagram is not to scale: slopes on the graphs have been exaggerated to highlight evolution of particle size distribution.

## CHAPTER V

### CONCLUSIONS

Aptly characterizing the subterranean idiosyncrasies of volcanic eruptions requires creative approaches. In my PhD work, I use pyroclasts as windows into the volcanic conduit. I examined pyroclastic products of four eruptions from three Cascade Volcanoes, with extensive examinations of the most recent eruptions of Newberry Volcano and Medicine Lake Volcano. I leveraged mass amounts of data with several tools to address common assumptions in physical volcanology, asking:

- 1) How representative are the pyroclasts we study?**
- 2) How representative are the methodologies we use to assess their properties?**
- 3) What are studies missing that examine a limited size fraction of a component (i.e. ash or lapilli) or only one component at all (i.e. obsidian or pumice)?**
- 4) How might such patchwork approaches to studying volcanic material impact interpretations of the conduit and of numerical models of ash dispersion?**

In Chapter II, I broached these subjects via case study of pumices from the 1060 CE Glass Mountain eruption of Medicine Lake Volcano. I found that the endmember size approach to studying pyroclasts biases our interpretation to a limited lateral section of the conduit. Pumice texture, morphology, and size directly reflects locational formation in the conduit. Capturing the breadth and complexity of processes occurring within thus requires studying a greater size range of clasts – not simply ash or lapilli. Furthermore,

ash dispersion models should use actual density-size data, or at least log-linear composition-specific models to ensure forecasting of hazards is accurate.

In Chapter III, I applied this knowledge in examining the 640 C.E. Big Obsidian Flow eruption of Newberry Volcano. I expanded my methodologies from 2 pits to >10 as compared to the Chapter II study. I then detailed physical attributes of 4 pits on the dispersal axis down to the layer and clast scale for ash- to lapilli-sized particles, as is necessary based on my previous work. These measurements were then contextualized with geochemical data. Ultimately, I found that sintering can modulate the explosive-effusive transition, indicating that upper conduit processes alone can be responsible for changes in eruptive behavior. Additionally, pulsatory Vulcanian behavior can herald a switch to effusive or hybrid activity.

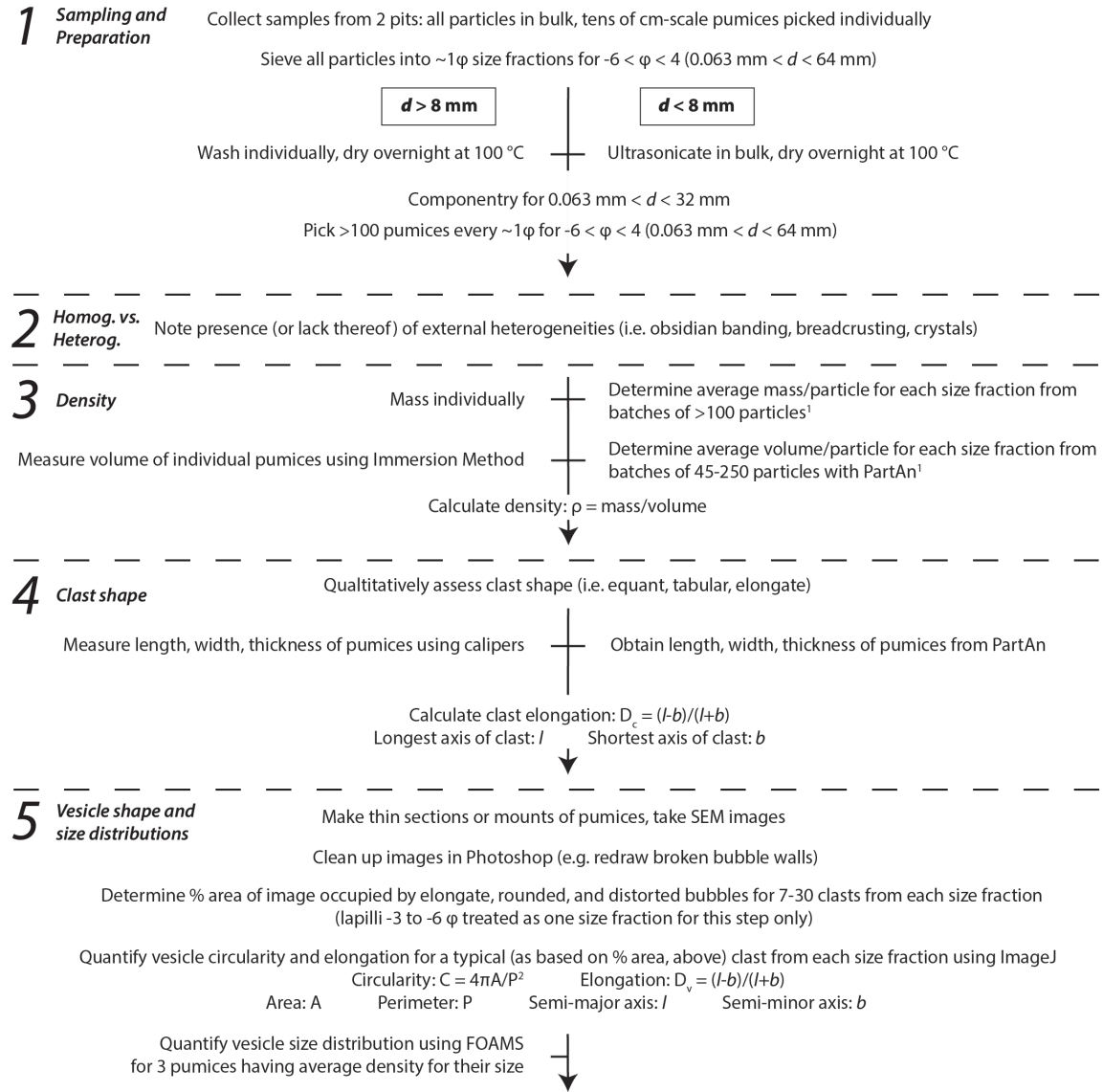
In Chapter IV, I and co-authors examined textures of porous pyroclasts from the aforementioned eruptions, as well as from those of the Cleetwood and climactic eruptions of Mt. Mazama. We find that porous lapilli, like obsidian pyroclasts, can result from cycles of fragmentation and sintering. As such, future work should look to studying the protopyroclasts – that is, the individual domains preserved within a given pyroclast – to understand primary fragmentation processes.

As individual volcanic systems become highly characterized, amalgamating data across such systems will allow for advances in the greater understanding of volcanic behavior. Still, the complex individuality of each volcano underscores the necessity for precise and rigorous eruption-by-eruption literature. As we push hazard science forward, so too must we reflect on not only the depth, but the breadth of our studies – namely,

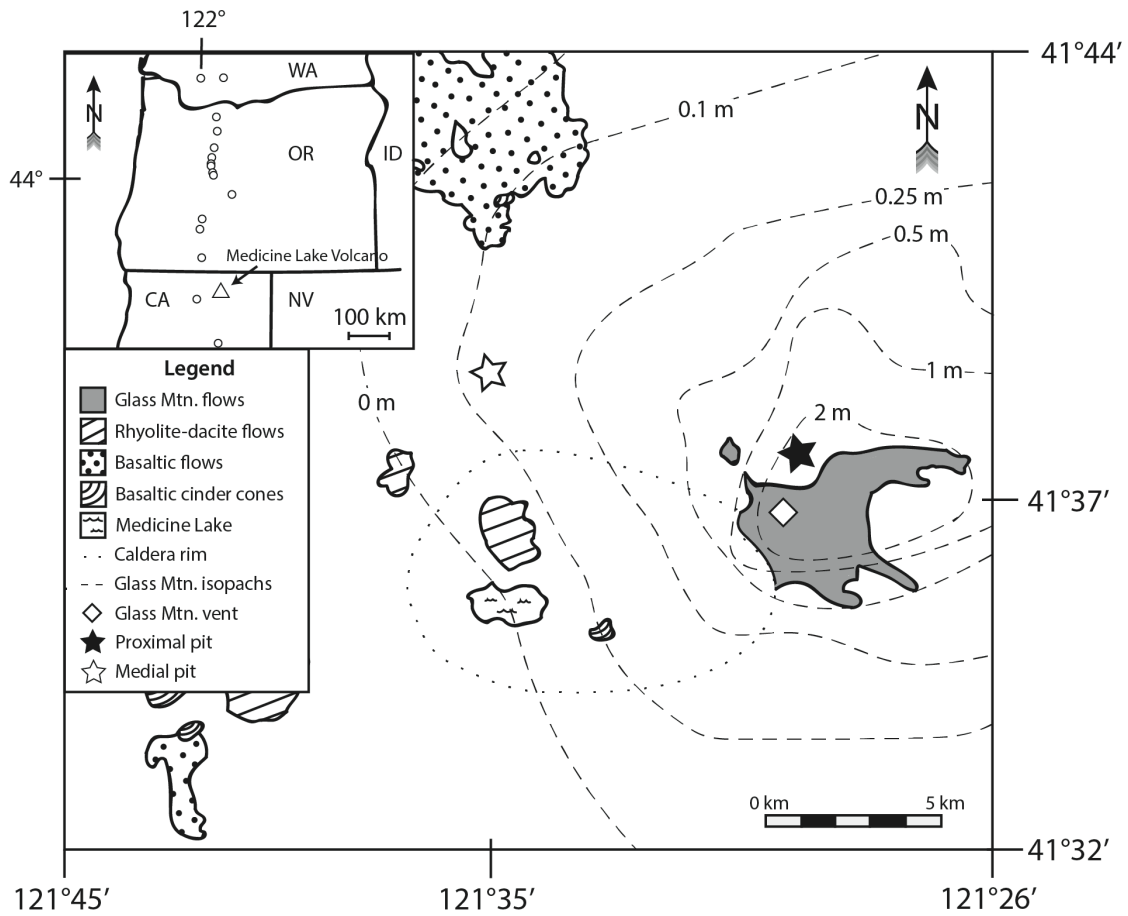
whether our science fulfills humanitarian goals we imperatively cite as the reason for our work.

## APPENDIX A

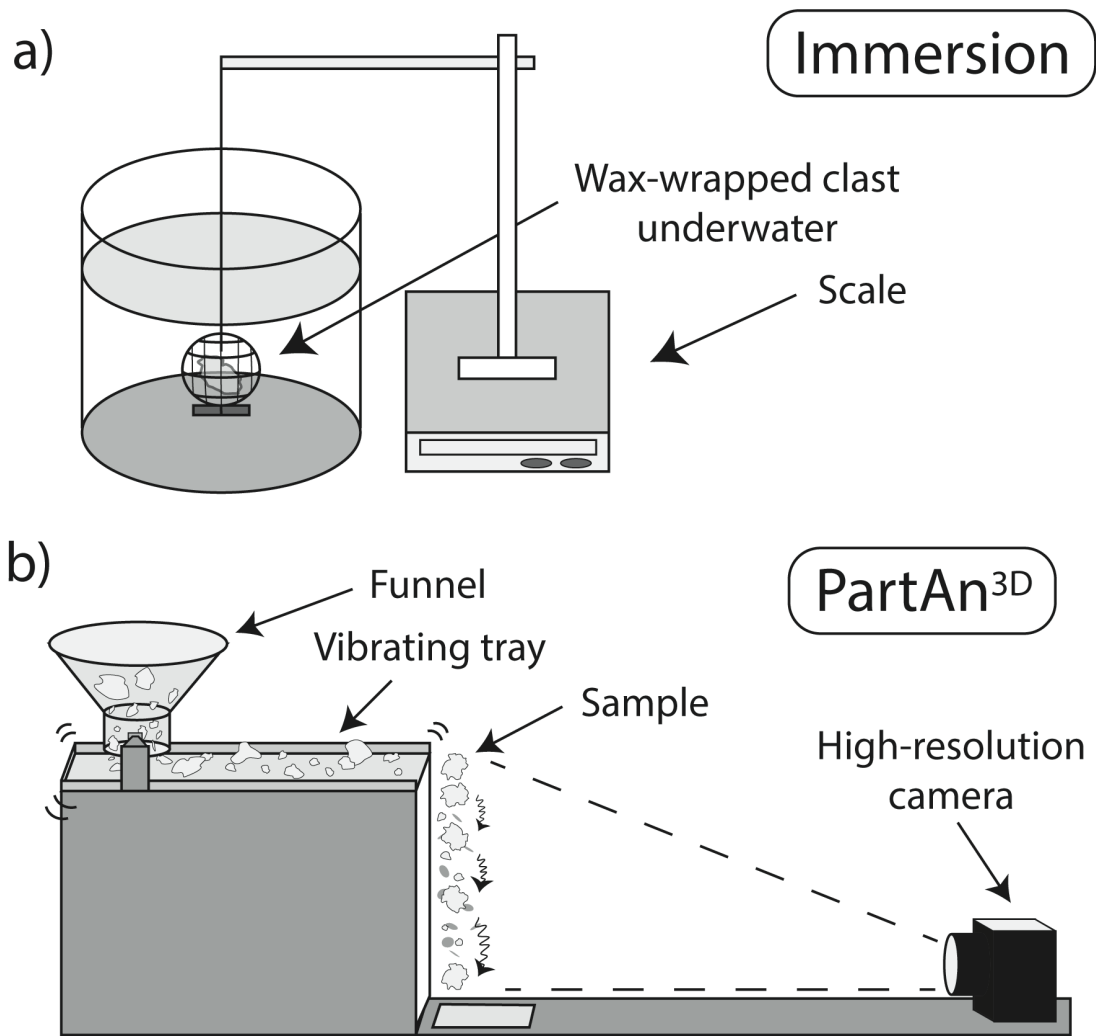
### CHAPTER II: THE MORPHOLOGY AND TEXTURE OF PLINIAN PYROCLASTS REFLECT THEIR LATERAL SOURCING IN THE CONDUIT



**Figure A.1.:** Methodological flowchart for data obtained in this study. Numbers correlate to methodology sub-headers in the manuscript (i.e., number 1 correlates to section 3.1, 2 to 3.2, etc.). <sup>1</sup>Density for  $0.063\text{-}0.125 \mu\text{m}$  particles was later estimated using microscope images as they proved too small for this approach.



**Figure A.2.:** Map of sample locations at Glass Mountain, Medicine Lake Volcano, California. Isolines are from the Plinian phase of the 1060 CE eruption (Heiken, 1978).



**Figure A.3.:** Methods used for determining the volume of a clast. a) The classical immersion method (Houghton and Wilson, 1989) and b) a dynamic image analyzer (Microtrac, PartAn<sup>3D</sup>), which determines both the shape and size of particles using analysis of optical images.

#### A.4. Volume determination

Clast volume was determined using the classical immersion method or a Microtrac Dynamic Image Analyzer (PartAn<sup>3D</sup>; Fig. A.3). For the classical immersion method (Archimedes principle; Houghton and Wilson, 1989) a clast is covered in wax and submerged underwater in a cage with a ballast. The buoyant force on a submerged clast equals the weight of water displaced by the clast. As water has a density of  $\sim 1 \text{ g cm}^{-3}$ , this method provides a simple way to determine the volume of irregularly-shaped particles (cf. Houghton and Wilson, 1989). Then, using the density of the solid phase ( $2.36 \pm 0.05 \text{ g.cm}^{-3}$ ), a volume can be calculated. Each clast was tightly wrapped in parafilm wax to prevent water seepage.

A Microtrac PartAn<sup>3D</sup> dynamic image analyzer was used to quantify the volume and shape of clasts that appeared, by visual inspection, to be smaller than about  $1 \text{ cm}^3$  (Fig. A.2). Clasts pour out of a funnel onto a vibrating tray, then fall in front of a white backlit panel. A high-resolution optical camera ( $1 \mu\text{m px}^{-1}$ ) tracks and takes several images of each clast as it rotates while falling. A software determines shape parameters and calculates particle size in 3D based on a compilation of these images. This instrument can analyze hundreds of thousands of particles in a matter of tens of seconds. Volumes reported in this study were calculated using measured Feret diameters. Before each analysis using the PartAn<sup>3D</sup>, stainless steel spheres of certified volume were dropped to ensure accuracy of measurement. Clast measurements proceeded only if the measured volume of the sphere was within 1% of the sphere's certified volume. Each clast was then dropped at least 15 times to get an average volume. For clasts  $< 8 \text{ mm}$  diameter, 45-250 clasts within each size fractions defined above were dropped, and an average particle



volume calculated. Standard deviation for an individual lapilli clast measured 20 times using the immersion method produced density values within 5% of the mean. Volumes obtained using both immersion and PartAn<sup>3D</sup> on 135 clasts 0.25-3 cm<sup>3</sup> are generally within 10% of each other; clasts <1 cm<sup>3</sup> have measurement differences within 5%. We used immersion data for clasts >1 cm<sup>3</sup> and PartAn<sup>3D</sup> values for smaller clasts, which could not be measured by immersion. The PartAn<sup>3D</sup> also reports numerous shape parameters, such as aspect ratio, sphericity and roughness, for example.

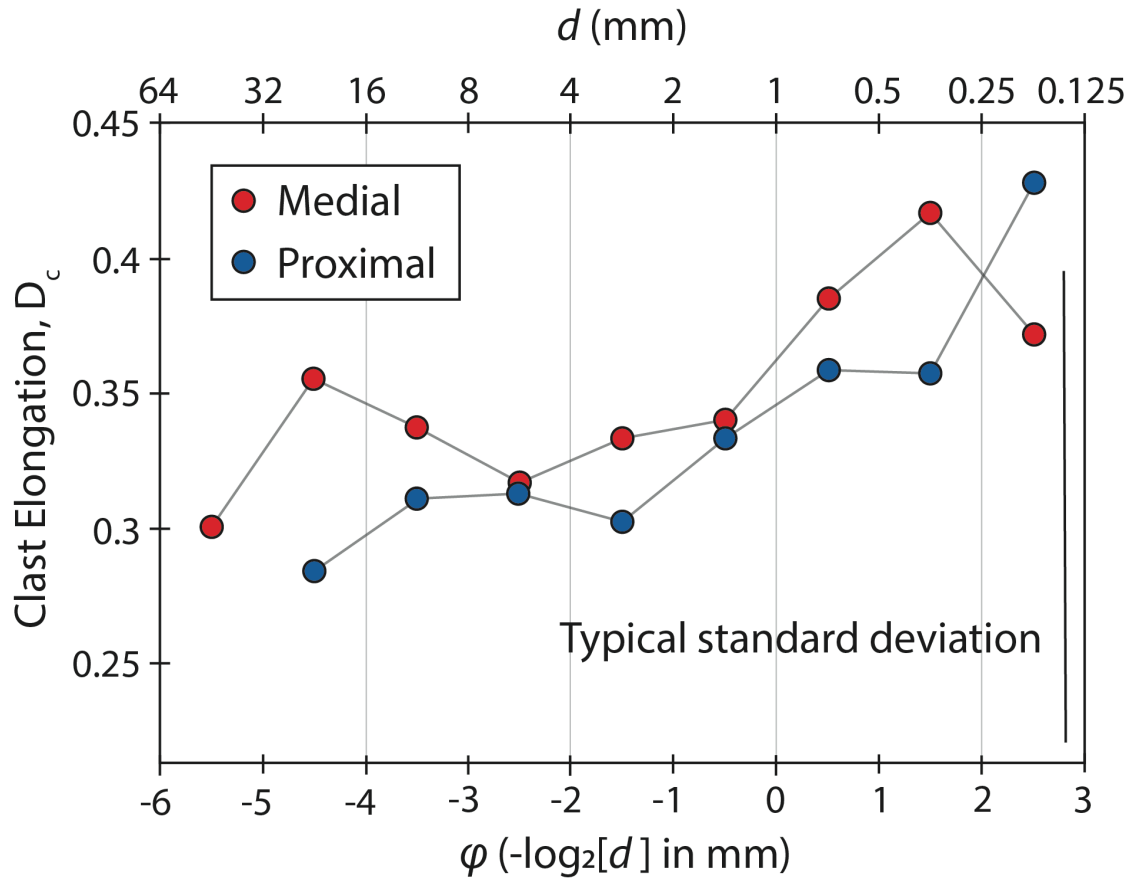
Clast Name	Volume (cm <sup>3</sup> )	Location	Porosity (%)	n	<i>N</i> (m <sup>-3</sup> )
77H	~10 <sup>0.5</sup>	Whole	75.9		
		Rim	74.7 ± 0.9	568	3.5 * 10 <sup>14</sup>
		Center	69.5 ± 1.3	315	3.0 * 10 <sup>14</sup>
69B	~10 <sup>1</sup>	Whole	78.8		
		Rim	72.6 ± 1.9	927	2.3 * 10 <sup>15</sup>
		Center	72.3 ± 2.5	379	1.4 * 10 <sup>15</sup>
79G	~10 <sup>2</sup>	Whole	87.3		
		Rim	85.7 ± 1.0	122	9.3 * 10 <sup>12</sup>
		Center	84.1 ± 2.7	182	1.1 * 10 <sup>13</sup>

**Table A.1.:** Vesicle number data for three pyroclasts from the proximal pit. *n* is the total number of vesicles analyzed. The vesicle number density, *N*, is given per cubic meter of melt.

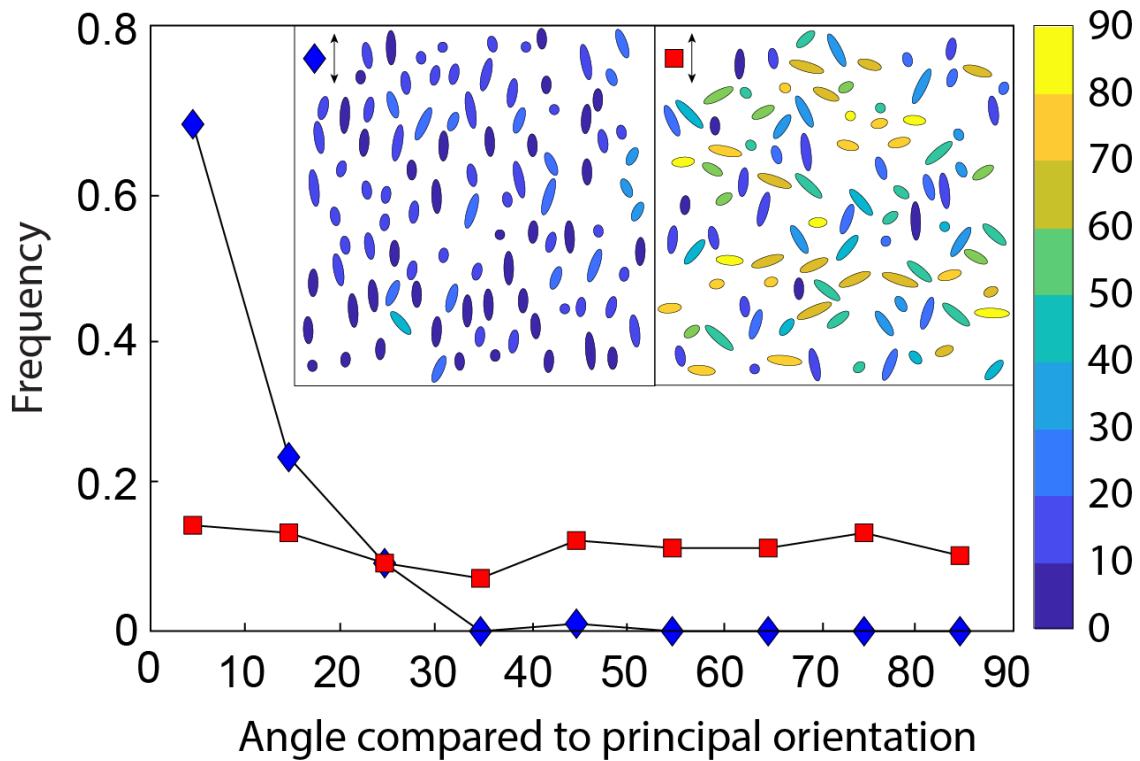
Medial Pit									
Diameter (mm)	Phi size	Number Count				Total	% Grain Counts		
		□ Pumices	■ Obsidians	▒ Lithics	▨ Crystals		25	50	75
16-32	-4 to -5	2	0	0	0	2			
8-16	-3 to -4	16	0	0	0	16			
4-8	-2 to -3	57	2	3	0	62			
2-4	-1 to -2	517	12	37	0	566			
0.85-2	0.23 to -1	352	21	18	0	391			
0.5-0.85	1 - 0.23	231	11	40	0	282			
0.355-0.5	1.5 - 1	421	28	74	12	535			
0.25-0.355	2 - 1.5	624	64	98	36	822			
0.125-0.25	3 - 2	264	71	70	36	441			
0.090-0.125	3.5 - 3	294	72	50	71	487			
0.063-0.090	4 - 3.5	170	65	33	26	294			

Proximal Pit									
Diameter (mm)	Phi size	Number Count				Total	% Grain Counts		
		□ Pumices	■ Obsidians	▒ Lithics	▨ Crystals		25	50	75
16-32	-4 to -5	66	0	1	0	67			
8-16	-3 to -4	400	14	88	0	502			
4-8	-2 to -3	334	15	109	0	458			
2-4	-1 to -2	283	48	213	0	544			
0.85-2	0.23 to -1	47	9	78	36	170			
0.5-0.85	1 - 0.23	145	13	116	46	320			
0.355-0.5	1.5 - 1	149	55	33	28	265			
0.25-0.355	2 - 1.5	252	61	81	64	458			
0.125-0.25	3 - 2	183	15	52	16	266			
0.090-0.125	3.5 - 3	198	16	4	5	223			
0.063-0.090	4 - 3.5	236	1	19	2	258			

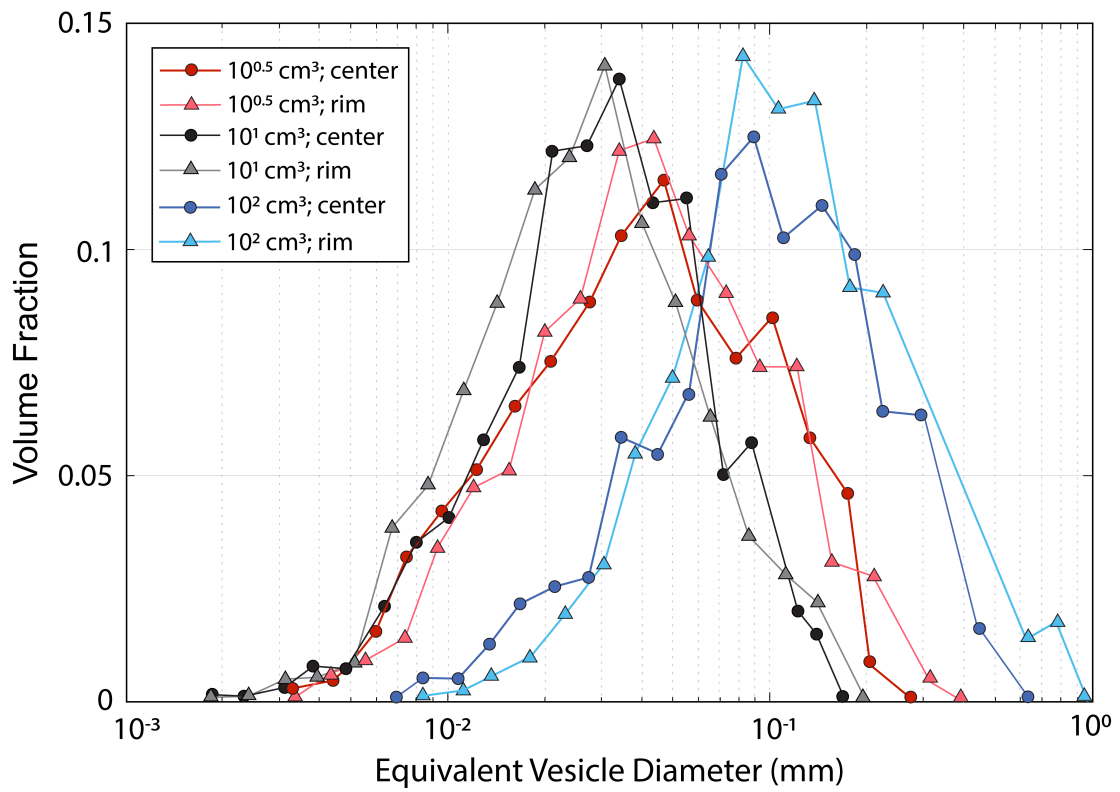
**Table A.2:** Componentry of the proximal and medial samples for clasts <32 mm and per size fraction, as determined by microscope point counts. Additional clasts 32-64 mm were hand-picked on the field; thus, this size fraction is not included as it would be biased. For the proximal pit, pumice is the greatest constituent at endmember size fractions. Obsidian, lithic, and free crystals tend to be most concentrated around 0.25-4 mm. For the medial pit, the amount of pumice continuously decreases while obsidian and quartz content increase at smaller grain sizes. Lithic content stays relatively constant.



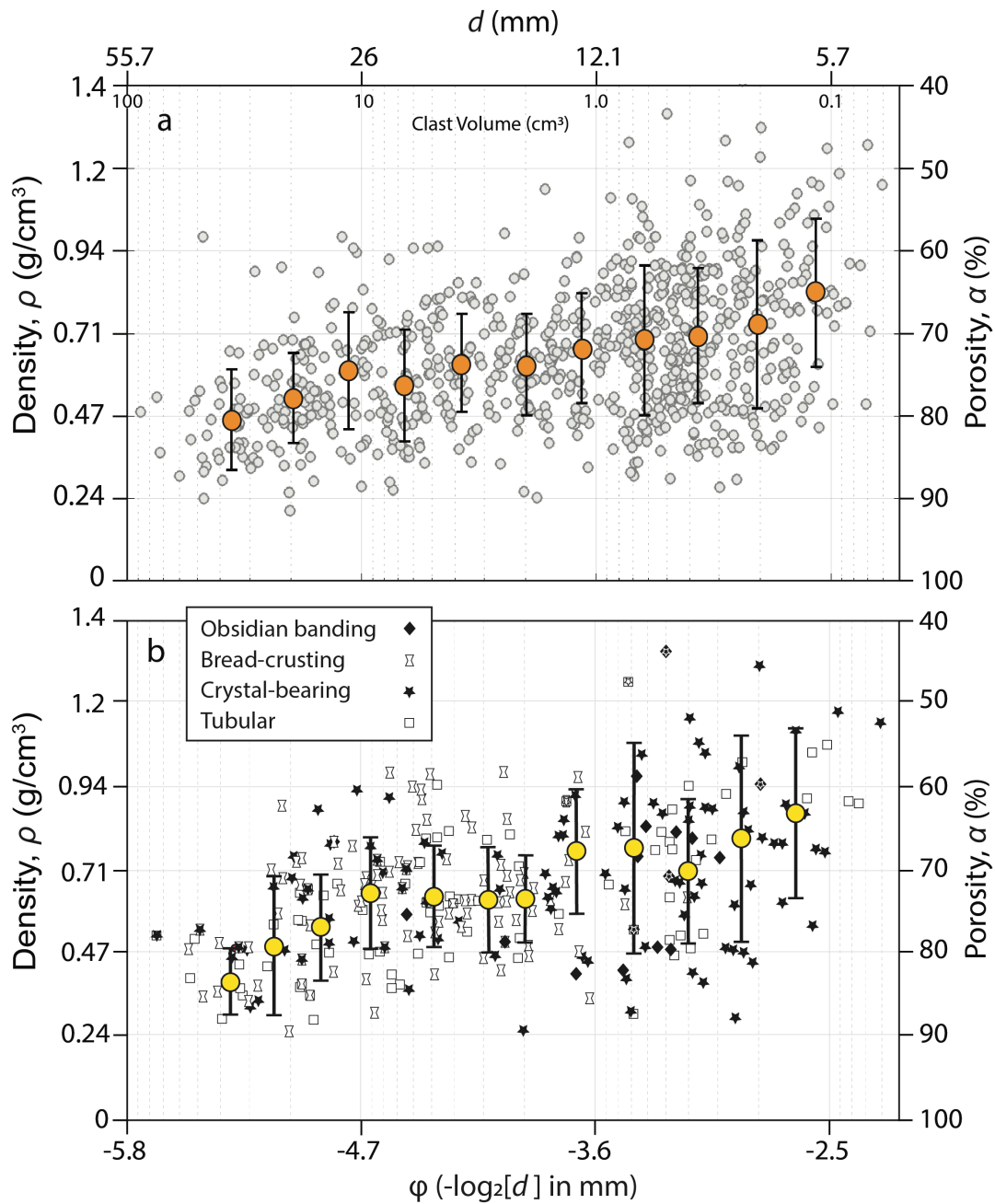
**Figure A.5.:** Plot of median elongation ( $D_c$ ) of clasts for every phi size examined for both medial and proximal pits. Clasts at all size fractions exhibit a wide variety of morphologies; however, small clasts in general tend to be more elongated.



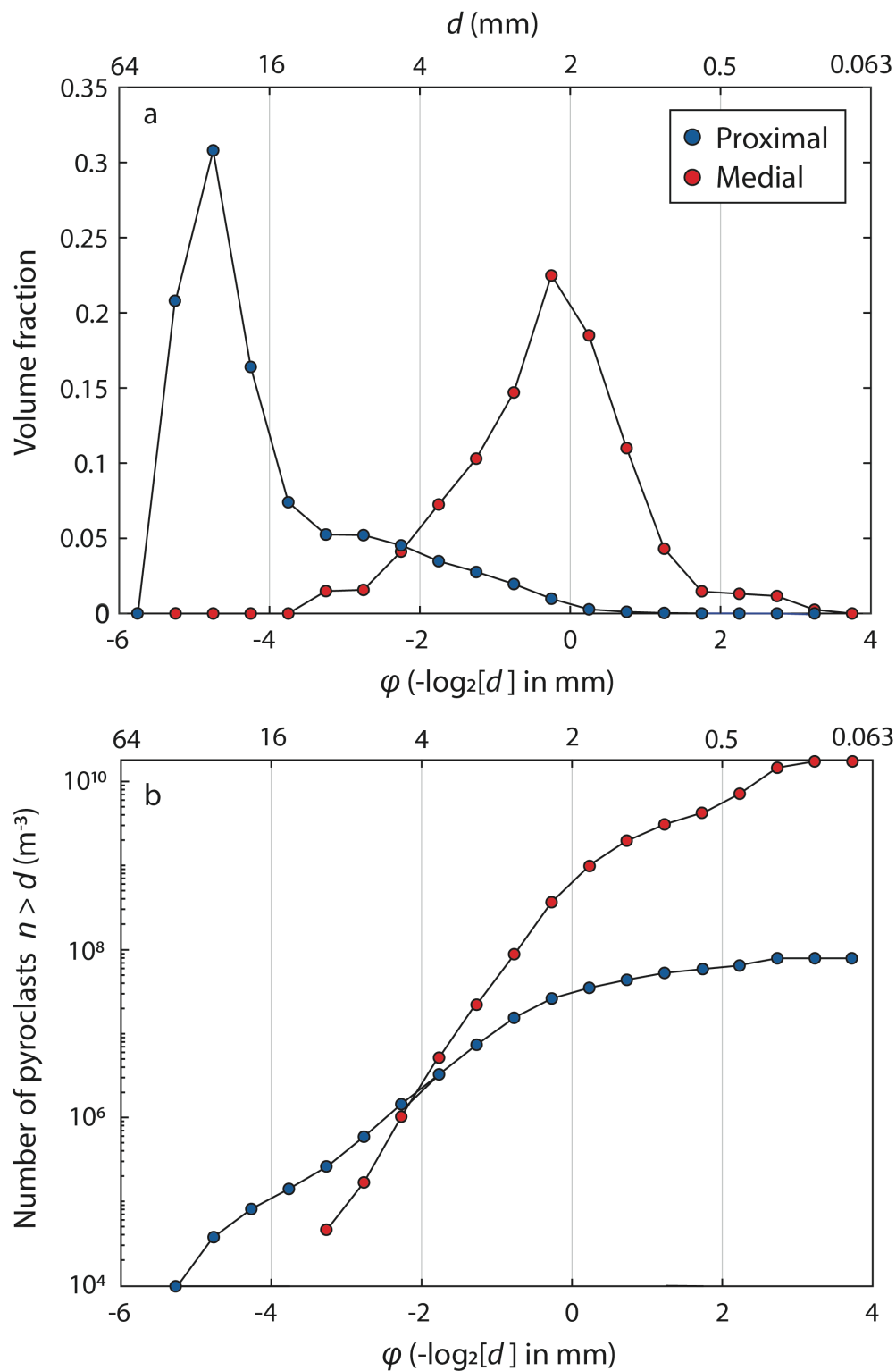
**Figure A.6.** Interpretation supplement for Fig. 5d. Here, we numerically generate two samples (blue, red) with 100 vesicles (ellipses) each that are oriented similarly (blue) or variably (red) overall. The frequency of ellipses exhibiting a given angle compared to the principal orientation of alignment (here set as north-south, 0 degrees) is plotted. For each of the natural samples plotted in Fig. 5d, the direction of vesicle relative to principal orientation of alignment was found and plotted in this way.



**Figure A.7.:** Volume fraction of vesicles versus their equivalent diameter for the core and rim of three clasts from the proximal pit spanning roughly three orders of magnitude in volume (diameters of 11 mm, 23 mm, and 45 mm). For all three clasts, the porosity and vesicle size distribution of the core is similar to that of the rim.

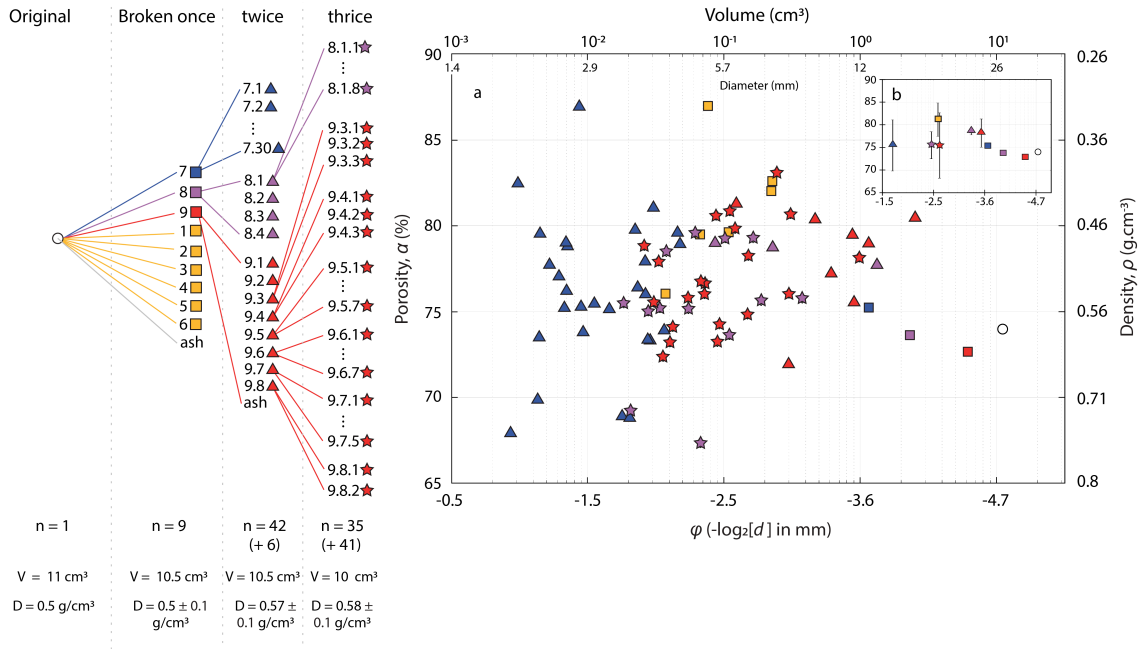


**Figure A.8.:** Porosity and density as a function of size for a) all lapilli and b) heterogeneous lapilli only, from the proximal pit. Averages are binned and plotted as orange or yellow dots with standard deviation error bars. Clasts increase in porosity from  $66 \pm 7\%$  to  $82 \pm 3\%$  over three orders of magnitude of volume, while heterogeneous clasts increase from  $62 \pm 7\%$  to  $84 \pm 3\%$  over the same range of sizes. Clasts may exhibit multiple heterogeneities (i.e., contain crystals *and* obsidian banding).



**Figure A.9.:** Volume fraction (a) and cumulative number density (b) of bulk samples every 0.5  $\phi$  for both pits.





**Figure A.10.:** Porosity and density versus clast size for a clast that was manually broken. Legend on the left shows breaking procedure, which occurred in three increments. Pieces appearing larger than  $\sim 8$  mm were subsequently broken and newly-formed fragments re-measured for their porosity and density. Graphs at right show a) data of all individual fragments and b) averages of the incrementally broken fragments. Standard deviation shows the range in porosity values of multiple resulting pieces at a given increment. Fragments tend to be close in porosity, or even slightly more porous, than the original sample.

## APPENDIX B

### CHAPTER III: LEVERAGING PHYSICAL AND GEOCHEMICAL DATA OF JUVENILE SILICIC PRODUCTS TO UNDERSTAND THE EXPLOSIVE-EFFUSIVE TRANSITION

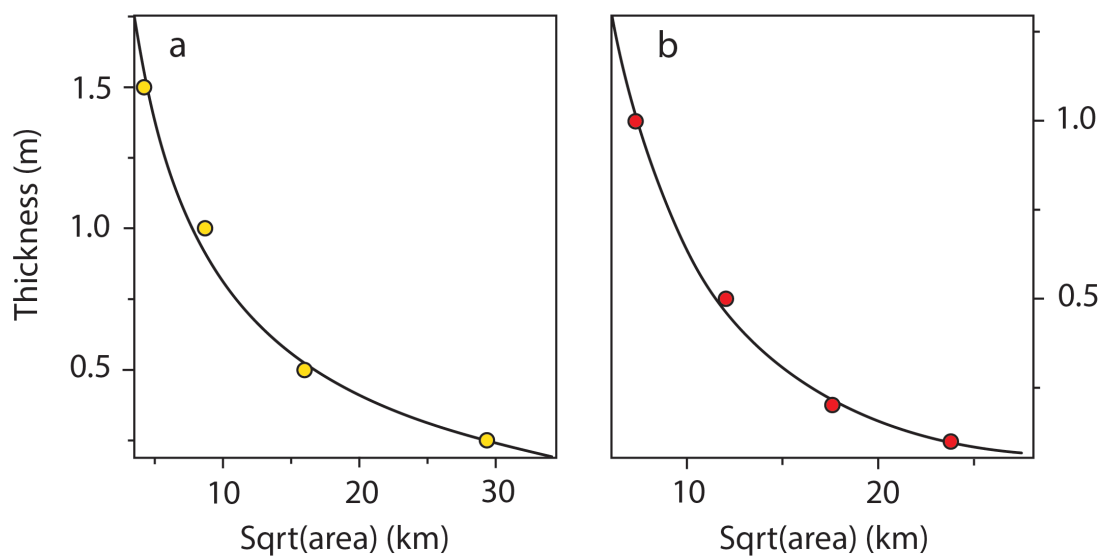


Figure B.1.: Thickness of the Newberry a) Lower Pumice and b) Upper pumice versus the square root of the area of the corresponding isopach ellipse. Figure modified from an AshCalc model that fit the data using a Weibull function (Daggitt et al., 2014).

## APPENDIX C

### CHAPTER IV: THE PRODUCTS OF PRIMARY FRAGMENTATION FINALLY REVEALED BY PUMICE AGGLOMERATES

#### **C.1. Sample collection**

All samples were collected by the authors between 2016 and 2018. They are all pumice lapilli from four subplinian and Plinian fall deposits.

##### *C.1.1. Newberry Volcano*

The Big Obsidian Flow period (~700 C.E.) of Newberry Volcano (Oregon, USA) erupted a volume of ~0.2 km<sup>3</sup> DRE (dense rock equivalent) divided approximately equally between initial pyroclastic fall deposits and final obsidian flow, with only 0.002 km<sup>3</sup> of pyroclastic flow deposit (McLeod and Sherrod, 1988). The estimated mass discharge rate is  $2.8 \times 10^7$  kg/s (Rust and Cashman, 2007). The tephra deposit is typical of subplinian eruptions (Houghton and Wilson, 1989). Samples were collected in two ~2-m-thick pits separated by 1 km, and both located ~10.8 km E of the vent (43.705665°, -121.097255°) on or slightly off the ENE dispersal axis. Samples are crystal-poor to crystal-free rhyolite.

##### *C.1.2. Medicine Lake Volcano*

The Plinian phase of the Glass Mountain eruption (1060±90 C.E.) of Medicine Lake Volcano (California, USA) deposited 0.09 km<sup>3</sup> DRE of fallout tephra with no evidence for pyroclastic density currents (Heiken, 1978). There is no estimate for the mass discharge rate for this eruption but given the similitude in volume and sedimentologic characteristics of the Plinian fall deposits with the Big Obsidian Flow tephra of Newberry,

we estimate the mass discharge rate to be also  $\sim 10^7$  kg/s. Samples were collected within a single layer towards the top of a several-meter section of the pumice-supported tephra fall deposit in a quarry about 2 km NNE of the vent ( $41.618356^\circ$ ,  $-121.495578^\circ$ ; Trafton and Giachetti, 2021), slightly off the NNE dispersal axis of the final phase of this eruption (Giachetti and Shea, in prep). Samples are crystal-poor rhyolite (Heiken, 1978).

### *C.1.3. Mount Mazama*

Both the Cleetwood and climactic eruptions of Mt Mazama occurred around 5,750 B.C.E. (Bacon, 1983). The Cleetwood phase initiated with a Plinian eruption that ejected  $1.5 \text{ km}^3$  of magma and ended with the emplacement of a  $0.6 \text{ km}^3$  obsidian flow. Estimated mass discharge rate is  $2 \pm 1 \times 10^8$  kg/s (Young, 1990). It was followed weeks to tens of years later (Kamata et al., 1993) by the caldera-forming climactic eruption that ejected  $\sim 61 \text{ km}^3$  of dense rock equivalent magma (Buckland et al., 2020). Samples from these two eruptions were collected 46 km SE of the vent ( $42.704941^\circ$ ,  $-121.638693^\circ$ ) in a single pit 2.96 m in thickness. This pit is on the dispersal axis of the Cleetwood phase of the eruption (SE), but off the main dispersal axis for the climactic phase (NE). The Cleetwood sample was collected midway in the 122-cm section of Cleetwood tephra, whereas the climactic sample was collected within the upper 57 cm of the 171-cm climactic Plinian fall deposit, corresponding to the “Upper Pumice fall unit” as designed by Young (1990). This phase of the climactic eruption reached a mass discharge rate of  $1.5 \pm 2.5 \times 10^9$  kg/s (Bacon, 1983). Both the Cleetwood and climactic samples collected are crystal-poor rhyodacite with no major chemical variations between rhyodacite components of the two eruptions (Bacon, 1983).

## **C.2. Lapilli selection**

For each eruption, one hundred ~1-4-cm porous lapilli were randomly picked from the entire sample and then analyzed for volume and bulk and connected porosities. All 400 pyroclasts were then visually inspected using a stereomicroscope to search for evidence of sintering on their surface such as juxtaposed domains with sharply contrasting texture (e.g., porosity, vesicle size distribution, direction of elongation) and/or delineating fractures with ash and/or trapped lithics. To reduce the bias in interpreting textures, each pyroclast was inspected independently by three of the authors and was considered to be “extremely likely” to be an amalgamation of protopyroclasts if identified as such three times, and “most-likely” if identified as such twice. Three to four pyroclasts extremely likely to be an amalgamation of protopyroclasts, together with another 2-3 lapilli that appear homogeneous, were then arbitrarily selected from each eruption for Computed Tomography imaging and further textural analyses.

## **C.3. Measurement of volume and total and connected porosity**

All 400 selected lapilli were rinsed and ultrasonicated in water, dried overnight in a furnace at 100 °C, and analyzed individually. Their volume,  $V$ , was determined either by the classical immersion method (Houghton and Wilson, 1989) or using a Microtrac PartAn<sup>3D</sup> particle size analyzer (Trafton and Giachetti, 2021). The mass of each clast,  $M$ , was measured using a high-precision balance and the bulk (total) porosity calculated using  $\varphi = M/(\rho V) \times 100$ , where  $\rho$  is the density of the solid phase. The volume of solid and isolated pores was obtained using a Micromeritics AccuPyc II 1340 gas pycnometer in a 10, 35 or 100 cm<sup>3</sup> sample chamber, using high-purity helium as working gas. The

connected porosity was then calculated. The density of the solid phase is  $2.36 \pm 0.05 \text{ g.cm}^{-3}$  for Medicine Lake Volcano (Giachetti et al., 2020) and was measured by helium pycnometry on finely crushed powders from several clasts for all other eruptions ( $2.32 \pm 0.01 \text{ g.cm}^{-3}$  for Newberry,  $2.38 \pm 0.01 \text{ g.cm}^{-3}$  for Cleetwood, and  $2.43 \pm 0.01 \text{ g.cm}^{-3}$  for the Climactic phase of Mazama eruption). The connectivity, the ratio of connected to total porosity, is plotted in Figure 1 for all clasts and reported in Table 1 for pyroclasts further analyzed for their texture.

#### **C.4. Computed Tomography and Scanning Electron Microscope**

Twenty-eight samples appearing either texturally homogeneous or extremely likely to be an amalgamation of protopyroclasts were analyzed by X-Ray computed microtomography at the University of Texas High-Resolution X-ray Computed Tomography (CT) Facility. For all analyses, a NSI scanner was used with the following setup: Fein Focus Microfocal source, 100 kV, 0.125-0.2 mA, no filter, Perkin Elmer detector, 0.25-0.5 pF gain, beam-hardening correction = 0.1. Depending on the sample size, the resolution varied from 5.56 to 25.10  $\mu\text{m}/\text{voxel}$ , resulting in a stack of 995 to 1,940 images per sample. The color balance of all the images of each sample was slightly altered to better highlight the different textures and produce the images shown in Figs. 1a-d. Thin sections of a subset of the samples were carbon-coated and analyzed using a Quanta 1000 Scanning Electron Microscope (SEM) at the University of Oregon Center for Advanced Materials Characterization in Oregon (CAMCOR). Both backscattered and secondary electrons were used at an acceleration of 25 kV and a working distance of about 1 cm. Images were acquired at a magnification between  $\times 35$  and  $\times 1,700$ .

### C.5. Protopyroclasts size distribution

As shown on Fig. 2, each pumice lapilli extremely likely to be an amalgamation is made of a few to thousands of textural domains, interpreted to be individual protopyroclasts separated by sharp or subtle boundaries. We measured protopyroclast size distributions in 2D on four samples, two samples from Medicine Lake Volcano (clast 8 and clast 86D, see Table 1 Supplementary material) and two from Newberry Volcano (clast 5 and clast 6) that exhibited a high number of protopyroclasts visible on the CT images. For each of the four samples, we used between 4 and 10 slices from the CT scans (corresponding to a single magnification for each sample) and 3 to 6 SEM images (3-6 magnifications), respectively. For each image, whether CT or SEM, we separated protopyroclasts manually using Adobe Photoshop (i.e., drew lines in between; Fig. 3A-B) and the area of each protopyroclast larger than  $50 \text{ px}^2$  was then obtained using Fiji (ImageJ; Schneider et al., 2012). This procedure allowed us to analyze all protopyroclasts larger than  $\sim 4 \mu\text{m}$  in equivalent diameter,  $d = 2 \times \sqrt{A/\pi}$ , where  $A$  is the area of the object in  $\mu\text{m}^2$ . Protopyroclasts cut by the edge of the SEM image and those with an area larger than  $1/100^{\text{th}}$  of the area of the SEM image were not considered in the distribution (Shea et al., 2010). For each magnification, analyzed protopyroclasts were sorted based on their equivalent diameter into 20 regular logarithmic bins spanning  $10^{-6} \text{ m}$  to  $10^{-2} \text{ m}$ , producing for each magnification a distribution of  $N_A$ , which is the number density of protopyroclasts per unit area. In MATLAB,  $N_A$  distributions of all the magnifications were then merged into a single distribution for the whole sample using magnification cutoffs defined to minimize the change in  $N_A$  values at the shift from one curve to another (Shea et al., 2010). The distribution of  $N_A$  for each sample was then converted into a distribution of number density

of protopyroclasts per unit volume,  $N_v$ , using the method of Sahagian and Proussevitch (1998) and plotted in Fig. 3c.



**Table C.2.:** Data collected on samples from Medicine Lake, Newberry and Mount Mazama volcanoes. Y stands for macroscopic textural heterogeneity and N for none. Evidence of sintering as observed on the CT scan images has been qualitatively graded from – to ++ or classified as banded where heterogeneities form pervasive subparallel domains. Connectivity is the ratio of connected (open) to bulk (total) porosity. In the CT scans column header, “vx” is an abbreviation for voxel.

sample ID	textural heterogeneity (Y/N)	evidence of sintering	mass (g)	pycnometer volume (cm <sup>3</sup> )	external volume (cm <sup>3</sup> )	equivalent diameter (mm)	density (g/cm <sup>3</sup> )	bulk (total) porosity	connected (open) porosity	connectivity	CT scans resolution (μm/vx)
<b>Medicine Lake</b>											
#1	Y	+	6.21	3.17	9.55	26.3	2.36	0.724	0.668	0.92	16.20
#2	N	-?	1.98	0.90	3.43	18.7	2.36	0.755	0.738	0.98	13.30
#3	N	++	1.39	0.77	2.12	15.9	2.36	0.721	0.636	0.88	12.90
#4	Y	banded	2.09	1.49	3.02	17.9	2.36	0.707	0.508	0.72	12.10
#5	Y	++	6.16	3.25	9.50	26.3	2.36	0.725	0.658	0.91	21.00
#6	N	++	0.76	0.40	0.94	12.2	2.36	0.657	0.571	0.87	9.75
#7	N	-	1.49	0.88	2.24	16.2	2.36	0.718	0.607	0.84	11.70
#8	Y	++	0.82	0.65	1.42	13.9	2.36	0.756	0.545	0.72	9.96
#86D	Y	++	7.96	5.09	15.43	30.9	2.36	0.781	0.670	0.86	25.10
<b>Newberry</b>											
#1	N	+	6.29	3.30	14.07	29.9	2.32	0.807	0.765	0.95	17.68
#2	N	-	0.98	0.57	2.46	16.8	2.32	0.828	0.767	0.93	9.29
#3	N	-	5.55	3.20	15.86	31.2	2.32	0.849	0.798	0.94	18.29
#4	Y	++	2.23	1.21	5.39	21.8	2.32	0.821	0.775	0.94	12.47
#5	Y	++	0.91	0.57	1.84	15.2	2.32	0.788	0.689	0.87	8.26
#6	Y	++	1.65	0.97	3.72	19.2	2.32	0.809	0.738	0.91	10.31
#7	Y	++	0.71	0.45	1.54	14.3	2.32	0.801	0.705	0.88	7.51
#1	Y	+	0.94	0.45	5.02	21.2	2.43	0.923	0.911	0.99	12.82
#2	Y	++	1.20	0.56	2.18	16.1	2.43	0.774	0.745	0.96	11.73
#3	N	++	0.40	0.14	1.05	12.6	2.43	0.842	0.867	1.03	8.86
#4	Y	++	0.40	0.14	0.75	11.3	2.43	0.782	0.819	1.05	8.32
#5	N	+?	1.72	0.93	3.93	19.6	2.43	0.820	0.762	0.93	11.24
#6	N	-?	0.85	0.39	2.57	17.0	2.43	0.863	0.849	0.98	8.79
#7	N	-?	3.66	2.09	9.77	26.5	2.38	0.843	0.786	0.93	14.48
#8	Y	++	0.25	0.14	0.53	10.0	2.38	0.801	0.734	0.92	5.56
#9	N	+	0.50	0.34	0.87	11.8	2.38	0.758	0.604	0.80	6.67
#10	N	-	0.59	0.40	1.23	13.3	2.38	0.798	0.672	0.84	6.93
#11	Y	++	0.46	0.28	0.86	11.8	2.38	0.779	0.675	0.87	7.61
#12	N	-	0.66	0.34	1.32	13.6	2.38	0.795	0.744	0.94	8.45
<b>Mazama - Cleetwood</b>											
<b>Mazama - climactic</b>											

## REFERENCES CITED

- Adams, N.K., Houghton, B.F., Fagents, S.A., Hildreth, W. (2006). The transition from explosive to effusive eruptive regime: the example of the 1912 Novarupta eruption, *Alaska. Geol. Soc. Am. Bull.* 118, 620–634. doi:10.1130/B25768.1.
- Alidibirov, M. A. (1994). A model for viscous magma fragmentation during volcanic blasts. *Bulletin of Volcanology*, 56(6), 459-465.
- Alidibirov, M., & Dingwell, D.B. (1996). Magma fragmentation by rapid decompression, *Nature*, 380, 146-149.
- Austin-Erickson, A., Büttner, R., Dellino, P., Ort, M. H., & Zimanowski, B. (2008). Phreatomagmatic explosions of rhyolitic magma: experimental and field evidence. *Journal of Geophysical Research: Solid Earth*, 113(B11).
- Bacon, C.R. (1983). Eruptive history of Mount Mazama and Crater Lake caldera, Cascade Range, USA. *Journal of Volcanology and Geothermal Research*, v. 18, p. 57–115, [https://doi.org/10.1016/0377-0273\(83\)90004-5](https://doi.org/10.1016/0377-0273(83)90004-5).
- Bagdassarov, N., Dorfman, A., and Dingwell, D.B. (2000). Effect of alkalis, phosphorus, and water on the surface tension of haplogranite melt. *American Mineralogist*, v. 85, p. 33–40, <https://doi.org/10.2138/am-2000-0105>.
- Bagheri, G., & Bonadonna, C. (2016). On the drag of freely falling non-spherical particles. *Powder Technology*, 301, 526-544.
- Barsotti, S., & Neri, A. (2008). The VOL-CALPUFF model for atmospheric ash dispersal: 2. Application to the weak Mount Etna plume of July 2001. *Journal of Geophysical Research: Solid Earth*, 113(3), 1–12. <https://doi.org/10.1029/2006JB004624>
- Bentley, B. J., & Leal, L. G. (1986). An experimental investigation of drop deformation and breakup in steady, two-dimensional linear flows. *Journal of Fluid Mechanics*, 167, 241-283.
- Blott, S.J., & Pye, K. (2008). Particle shape: a review and new methods of characterization and classification. *Sedimentology*, 55, 31-63.
- Bonadonna, C., & Costa, A. (2013). Plume height, volume, and classification of explosive volcanic eruptions based on the Weibull function. *Bulletin of Volcanology*, 75(8), 1-19.

- Bonadonna, C., & Phillips, J. C. (2003). Sedimentation from strong volcanic plumes. *Journal of Geophysical Research: Solid Earth*, 108(B7), 1–28. <https://doi.org/10.1029/2002jb002034>
- Bonasia, R., Capra, L., Costa, A., Macedonio, G., & Saucedo, R. (2011). Tephra fallout hazard assessment for a Plinian eruption scenario at Volcán de Colima (Mexico). *Journal of Volcanology and Geothermal Research*, 203(1–2), 12–22. <https://doi.org/10.1016/j.jvolgeores.2011.03.006>
- Brugger, C. R., & Hammer, J. E. (2010). Crystallization kinetics in continuous decompression experiments: implications for interpreting natural magma ascent processes. *Journal of Petrology*, 51(9), 1941-1965.
- Buckland, H.M., Cashman, K.V., Engwell, S.L. and Rust, A.C., 2020. Sources of uncertainty in the Mazama isopachs and the implications for interpreting distal tephra deposits from large magnitude eruptions. *Bulletin of Volcanology*, 82(3), pp.1-17.
- Cannata, C. B., De Rosa, R., Donato, P., & Taddeucci, J. (2014). Ash features from ordinary activity at Stromboli volcano. *International Journal of Geosciences*, 5(11), 1361.
- Carazzo, G., Tait, S., Michaud-Dubuy, A., Fries, A., and Kaminski, E. (2020). Transition from stable column to partial collapse during the 79 cal CE P3 Plinian eruption of Mt. Pelée volcano (Lesser Antilles). *Journal of Volcanology and Geothermal Research*, v. 392, 106764, <https://doi.org/10.1016/j.jvolgeores.2019.106764>.
- Carey, S. N., & Sigurdsson, H. (1982). Influence of particle aggregation on deposition of distal tephra from the May 18, 1980, eruption of Mount St. Helens volcano. *Journal of Geophysical Research: Solid Earth*, 87(B8), 7061-7072.
- Cas, R.A.F. and Wright, J.V. (1987) *Volcanic Successions: Modern and Ancient*. Allen and Unwin, London. <http://dx.doi.org/10.1007/978-94-009-3167-1>
- Cassidy, M., Cole, P. D., Hicks, K. E., Varley, N. R., Peters, N., & Lerner, A. H. (2015). Rapid and slow: Varying magma ascent rates as a mechanism for Vulcanian explosions. *Earth and Planetary Science Letters*, 420, 73-84.
- Cassidy, M., Manga, M., Cashman, K., & Bachmann, O. (2018). Controls on explosive-effusive volcanic eruption styles. *Nature communications*, 9(1), 1-16.
- Castro, J. M., & Dingwell, D. B. (2009). Rapid ascent of rhyolitic magma at Chaitén volcano, Chile. *Nature*, 461(7265), 780-783.

- Castro, J. M., & Gardner, J. E. (2008). Did magma ascent rate control the explosive-effusive transition at the Inyo volcanic chain, California?. *Geology*, 36(4), 279-282.
- Castro, J.M., B. Cordonnier, H. Tuffen, M. J. Tobin, L. Puskar, M. C. Martin, H. A. Bechtel. (2012). The role of melt-fracture degassing in defusing explosive rhyolite eruptions at volcán Chaitén. *Earth Planet. Sci. Lett.* **333**, 63–69 .
- Castro, J.M., B. Cordonnier, H. Tuffen, M. J. Tobin, L. Puskar, M. C. Martin, H. A. Bechtel (2012). The role of melt-fracture degassing in defusing explosive rhyolite eruptions at volcán Chaitén. *Earth Planet. Sci. Lett.* **333**, 63–69.
- Castro, J.M., C. I. Schipper, S. P. Mueller, A. S. Militzer, A. Amigo, C. S. Parejas, D. Jacob. (2013). Storage and eruption of near-liquidus rhyolite magma at Condon Caulle, Chile. *Bull. Volcanol.* **75**, 702.
- Castro, J.M., C. I. Schipper, S. P. Mueller, A. S. Militzer, A. Amigo, C. S. Parejas, D. Jacob. (2013). Storage and eruption of near-liquidus rhyolite magma at Condon Caulle, Chile. *Bull. Volcanol.* **75**, 702.
- Clarke, A. B., Stephens, S., Teasdale, R., Sparks, R. S. J., & Diller, K. (2007). Petrologic constraints on the decompression history of magma prior to Vulcanian explosions at the Soufrière Hills volcano, Montserrat. *Journal of Volcanology and Geothermal Research*, 161(4), 261-274.
- Collini, E., Osoreo, M.S., Folch, A., Viramonte, J.G., Villarosa, G. and Salmuni, G. (2013). Volcanic ash forecast during the June 2011 Cordón Caulle eruption. *Natural hazards*, 66(2), pp.389-412.
- Colombier, M., Wadsworth, F.B., Gurioli, L., Scheu, B., Kueppers, U., Di Muro, A., and Dingwell, D.B. (2017). The evolution of pore connectivity in volcanic rocks. *Earth and Planetary Science Letters*, v. 462, p. 99–109, <https://doi.org/10.1016/j.epsl.2017.01.011>.
- Costa, A., Dell’Erba, F., Vito, M. A., Isaia, R., Macedonio, G., Orsi, G., & Pfeiffer, T. (2009). Tephra fallout hazard assessment at the Campi Flegrei caldera (Italy). *Bulletin of Volcanology*, 71(3), 259–273. <https://doi.org/10.1007/s00445-008-0220-3>
- Daggitt, M.L., Mather, T.A., Pyle, D.M., and Page, S. (2014). AshCalc – a new tool for the comparison of the exponential, power-law and Weibull models of tephra deposition. *Journal of Applied Volcanology*, 3:7.

- Dartevelle, S., and Valentine, G.A. (2007). Transient multiphase processes during the explosive eruption of basalt through a geothermal borehole (Námafjall, Iceland, 1977) and implications for natural volcanic flows. *Earth and Planetary Science Letters*, v. 262, p. 363–384, <https://doi.org/10.1016/j.epsl.2007.07.053>.
- Dingwell, D. B., Lavallée, Y., Hess, K. U., Flaws, A., Marti, J., Nichols, A. R., ... & Schillinger, B. (2016). Eruptive shearing of tube pumice: pure and simple. *Solid Earth*, 7(5), 1383-1393.
- Dingwell, D.B. (1996). Volcanic dilemma—Flow or blow? *Science*, v. 273, p. 1054–1055, <https://doi.org/10.1126/science.273.5278.1054>.
- Dioguardi, F., Mele, D., and Dellino, P. (2018). A new one-equation model of fluid drag for irregularly shaped particles valid over a wide range of Reynolds number: aerodynamic drag of irregular particles. *Journal of Geophysical Research, Solid Earth* 123, 144-156.
- Donnelly-Nolan, J. M., Nathenson, M., Champion, D. E., Ramsey, D. W., Lowenstern, J. B., & Ewert, J. W. (2007). Volcano hazards assessment for Medicine Lake volcano, northern California (No. 2007-5174-A). Geological Survey (US).
- Donnelly-Nolan, J. M., Stovall, W. K., Ramsey, D. W., Ewert, J. W., & Jensen, R. A. (2011). Newberry Volcano—central Oregon’s sleeping giant. *US Geological Survey Fact Sheet*, 3145(6).
- Druitt, T. H., Kokelaar, B. P., & Francis, P. (2004). The eruption of Soufrière Hills volcano, Montserrat, from 1995 to 1999. Geological Society, London, *Memoirs* (Vol. 29).
- Druitt, T. H., Young, S. R., Baptie, B., Bonadonna, C., Calder, E. S., Clarke, A. B., ... & Voight, B. (2002). Episodes of cyclic Vulcanian explosive activity with fountain collapse at Soufrière Hills Volcano, Montserrat. *Memoirs-Geological Society of London*, 21, 281-306.
- Dufek, J., & Manga, M. (2008). In situ production of ash in pyroclastic flows. *Journal of Geophysical Research: Solid Earth*, 113(B9).
- Dufek, J., Manga, M., & Patel, A. (2012). Granular disruption during explosive volcanic eruptions. *Nature Geoscience*, 5(8), 561-564.
- Eichelberger, J. C., & Westrich, H. R. (1981). Magmatic volatiles in explosive rhyolitic eruptions. *Geophysical research letters*, 8(7), 757-760.
- Eichelberger, J. C., Carrigan, C. R., Westrich, H. R., & Price, R. H. (1986). Non-explosive silicic volcanism. *Nature*, 323(6089), 598-602.

- Ewert, J. W. (2007). System for ranking relative threats of US volcanoes. *Natural Hazards Review*, 8(4), 112-124.
- Ewert, J. W., Diefenbach, A. K., & Ramsey, D. W. (2018). *2018 update to the US Geological Survey national volcanic threat assessment* (No. 2018-5140). US Geological Survey.
- Eychenne, J., & Le Penec, J. L. (2012). Sigmoidal particle density distribution in a subplinian scoria fall deposit. *Bulletin of volcanology*, 74(10), 2243-2249.
- Folch, A., Jorba, O., & Viramonte, J. (2008). Volcanic ash forecast-application to the May 2008 Chaitén eruption. *Nat. Hazards Earth Syst. Sci*, 8(4), 927-940.
- Freire, S., Florczyk, A. J., Pesaresi, M., & Sliuzas, R. (2019). An improved global analysis of population distribution in proximity to active volcanoes, 1975–2015. *ISPRS international journal of geo-information*, 8(8), 341.
- Ganser, G.H. (1993). A rational approach to drag prediction of spherical and non-spherical particles. *Powder Technology*, 77, 143-152.
- Gardner, J. E., Carey, S., & Sigurdsson, H. (1998). Plinian eruptions at Glacier Peak and Newberry volcanoes, United States: Implications for volcanic hazards in the Cascade Range. *Geological Society of America Bulletin*, 110(2), 173-187.
- Gardner, J. E., Thomas, R. M. E., Jaupart, C., & Tait, S. (1996). Fragmentation of magma during Plinian volcanic eruptions. *Bulletin of Volcanology*, 58(2–3), 144–162. <https://doi.org/10.1007/s004450050132>
- Gardner, J. E., Wadsworth, F. B., Llewellyn, E. W., Watkins, J. M., & Coumans, J. P. (2018). Experimental sintering of ash at conduit conditions and implications for the longevity of tuffisites. *Bulletin of Volcanology*, 80(3), 23.
- Gardner, J. E., Wadsworth, F. B., Llewellyn, E. W., Watkins, J. M., & Coumans, J. P. (2019). Experimental constraints on the textures and origin of obsidian pyroclasts. *Bulletin of Volcanology*, 81(4), 22.
- Gardner, J.E., Carey, S., and Sigurdsson, H. (1998). Plinian eruptions at Glacier Peak and Newberry volcanoes, United States: Implications for volcanic hazards in the Cascade Range. *Geological Society of America Bulletin*, v. 110, p. 173–187.
- Gardner, James E., Llewellyn, E. W., Watkins, J. M., & Befus, K. S. (2017). Formation of obsidian pyroclasts by sintering of ash particles in the volcanic conduit. *Earth and Planetary Science Letters*, 459, 252–263, <https://doi.org/10.1016/j.epsl.2016.11.037>.

- Giachetti, T., Druitt, T. H., Burgisser, A., Arbaret, L., & Galven, C. (2010). Bubble nucleation, growth and coalescence during the 1997 Vulcanian explosions of Soufrière Hills Volcano, Montserrat. *Journal of Volcanology and Geothermal Research*, 193(3-4), 215-231.
- Giachetti, T., Hudak, M. R., Shea, T., Bindeman, I. N., & Hoxsie, E. C. (2020). D/H ratios and H<sub>2</sub>O contents record degassing and rehydration history of rhyolitic magma and pyroclasts. *Earth and Planetary Science Letters*, 530, 115909.
- Giachetti, T., Trafton, K. R., Wiejaczka, J., Gardner, J. E., Watkins, J. M., Shea, T., & Wright, H. M. (2021). The products of primary magma fragmentation finally revealed by pumice agglomerates. *Geology*, 49(11), 1307-1311.
- Giordano, G., & De Astis, G. (2021). The summer 2019 basaltic Vulcanian eruptions (paroxysms) of Stromboli. *Bulletin of Volcanology*, 83(1), 1-27.
- Gonnermann, H. M. (2015). Magma fragmentation. *Annual Review of Earth and Planetary Sciences*, 43, 431-458.
- Gonnermann, H. M., & Manga, M. (2003). Explosive volcanism may not be an inevitable consequence of magma fragmentation. *Nature*, 426(6965), 432-435.
- Gonnermann, H. M., & Manga, M. (2013). Dynamics of magma ascent. *Modeling volcanic processes: The physics and mathematics of volcanism*, 55.
- Gonnermann, H.M. and Manga, M., (2007). The fluid mechanics inside a volcano. *Annu. Rev. Fluid Mech.*, 39, 321-356, <https://doi.org/10.1146/annurev.fluid.39.050905.110207>.
- Gonnermann, H.M., and Houghton, B.F. (2012). Magma degassing during the Plinian eruption of Novarupta, Alaska, 1912. *Geochemistry Geophysics Geosystems*, v. 13, Q10009, <https://doi.org/10.1029/2012GC004273>.
- Grady, D.E., 1982, Local inertial effects in dynamic fragmentation: *Journal of Applied Physics*, v. 53, p. 322–325, <https://doi.org/10.1063/1.329934>.
- Gurioli, L., Harris, A.J.L., Houghton, B.F., Polacci, M., & Ripepe, M. (2008). Textural and geophysical characterization of explosive basaltic activity at Villarrica volcano. *Journal of Geophysical Research* 113, B08206. doi:10.1029/2007JB005328.
- Hajimirza, S., Gonnermann, H.M., and Gardner, J.E. (2021). Reconciling bubble nucleation in explosive eruptions with geospeedometers. *Nature Communications*, v. 12, p.1–8, <https://doi.org/10.1038/s41467-020-20541-1>.

- Hamada, M., Laporte, D., Cluzel, N., Koga, K. T., & Kawamoto, T. (2010). Simulating bubble number density of rhyolitic pumices from Plinian eruptions: constraints from fast decompression experiments. *Bulletin of Volcanology*, 72(6), 735-746.
- Heath, B. A., Hooft, E. E., Toomey, D. R., & Bezada, M. J. (2015). Imaging the magmatic system of Newberry Volcano using joint active source and teleseismic tomography. *Geochemistry, Geophysics, Geosystems*, 16(12), 4433-4448.
- Heiken, G. (1978). Plinian-type eruptions in the Medicine Lake Highland, California, and the nature of the underlying magma. *Journal of Volcanology and Geothermal Research*, 4(3-4), 375-402.
- Hess, K. U., & Dingwell, D. B. (1996). Viscosities of hydrous leucogranitic melts: A non-Arrhenian model. *American Mineralogist: Journal of Earth and Planetary Materials*, 81(9-10), 1297-1300.
- Hiroi, Y., & Miyamoto, T. (2016). Relationship between eruptive style and vesicularity of juvenile clasts during eruptive episode A of Towada Volcano, Northeast Japan. *Journal of Volcanology and Geothermal Research*, 325, 86-97.
- Houghton, B. F., & Wilson, C. J. N. (1989). A vesicularity index for pyroclastic deposits. *Bulletin of volcanology*, 51(6), 451-462.
- Janebo, M. H., Houghton, B. F., Thordarson, T., Bonadonna, C., & Carey, R. J. (2018). Total grain-size distribution of four subplinian–Plinian tephra from Hekla volcano, Iceland: Implications for sedimentation dynamics and eruption source parameters. *Journal of Volcanology and Geothermal Research*, 357, 25-38.
- Jaupart, C., & Allègre, C. J. (1991). Gas content, eruption rate and instabilities of eruption regime in silicic volcanoes. *Earth and Planetary Science Letters*, 102(3-4), 413-429.
- Jones, T. J., & Russell, J. K. (2017). Ash production by attrition in volcanic conduits and plumes. *Scientific reports*, 7(1), 1-12.
- Jones, T.J., Russell, J.K., Lim, C.J., Ellis, N., and Grace, J.R. (2017). Pumice attrition in an air-jet. *Powder Technology*, v. 308, p. 298–305, <https://doi.org/10.1016/j.powtec.2016.11.051>.
- Jordan, B. T., Grunder, A. L., Duncan, R. A., & Deino, A. L. (2004). Geochronology of age-progressive volcanism of the Oregon High Lava Plains: Implications for the plume interpretation of Yellowstone. *Journal of Geophysical Research: Solid Earth*, 109(B10).



- Kamata, H., Suzuki-Kamata, K., and Bacon, C.R. (1993). Deformation of the Wineglass Welded Tuff and the timing of caldera collapse at Crater Lake, Oregon. *Journal of volcanology and geothermal research*, 56(3), pp.253-265.
- Kaminski, É., & Jaupart, C. (1997). Expansion and quenching of vesicular magma fragments in Plinian eruptions. *Journal of Geophysical Research: Solid Earth*, 102(B6), 12187–12203. <https://doi.org/10.1029/97jb00622>
- Kaminski, E., and Jaupart, C. (1998). The size distribution of pyroclasts and the fragmentation sequence in explosive volcanic eruptions. *Journal of Geophysical Research*, v. 103, p. 29,759–29,779, <https://doi.org/10.1029/98JB02795>.
- Kennedy, B. M., Jellinek, A. M., Russell, J. K., Nichols, A. R. L., & Vigouroux, N. (2010). Time-and temperature-dependent conduit wall porosity: a key control on degassing and explosivity at Tarawera volcano, New Zealand. *Earth and Planetary Science Letters*, 299(1-2), 126-137.
- Kennedy, B., Spieler, O., Scheu, B., Kueppers, U., Taddeucci, J., & Dingwell, D. B. (2005). Conduit implosion during Vulcanian eruptions. *Geology*, 33(7), 581-584.
- Klug, C., & Cashman, K. V. (1994). Vesiculation of May 18, 1980, Mount St. Helens magma. *Geology*, 22(5), 468-472.
- Klug, C., & Cashman, K. V. (1996). Permeability development in vesiculating magmas: implications for fragmentation. *Bulletin of Volcanology*, 58(2-3), 87-100.
- Klug, C., Cashman, K. V., & Bacon, C. (2002). Structure and physical characteristics of pumice from the climactic eruption of Mount Mazama (Crater Lake), Oregon. *Bulletin of Volcanology*, 64(7), 486-501.
- Kolzenburg, S., Russell, J.K., and Kennedy, L.A. (2013). Energetics of glass fragmentation: Experiments on synthetic and natural glasses. *Geochemistry Geophysics Geosystems*, v. 14, p. 4936–4951, <https://doi.org/10.1002/2013GC004819>.
- Kuehn, S. C. (2002). *Stratigraphy, distribution, and geochemistry of the Newberry Volcano tephra*. Washington State University.
- Kuehn, S. C., & Foit Jr, F. F. (2006). Correlation of widespread Holocene and Pleistocene tephra layers from Newberry Volcano, Oregon, USA, using glass compositions and numerical analysis. *Quaternary International*, 148(1), 113-137.
- Kueppers, U., Perugini, D., and Dingwell, D.B. (2006). “Explosive energy” during volcanic eruptions from fractal analysis of pyroclasts. *Earth and Planetary Science Letters*, v. 248, p. 800–807, <https://doi.org/10.1016/j.epsl.2006.06.033>.

- Kueppers, U., Putz, C., Spieler, O., & Dingwell, D. (2012). Abrasion in pyroclastic density currents: Insights from tumbling experiments. *Phys. Chem. Earth*, 45-46, 33-39.
- Larsen, G., Newton, A.J., Dugmore, A.J., & Vilmundardóttir, E.G. (2001). Geochemistry, dispersal, volumes, and chronology of Holocene silicic tephra layers from the Katla volcanic system, Iceland. *Journal of Quaternary Science*, 16(2), 119-132.
- LaRue, A., Baker, D. R., Polacci, M., Allard, P., & Sodini, N. (2013). Can vesicle size distributions assess eruption intensity during volcanic activity?. *Solid Earth*, 4(2), 373-380.
- Lautze, N. C., & Houghton, B. F. (2007). Linking variable explosion style and magma textures during 2002 at Stromboli volcano, Italy. *Bulletin of Volcanology*, 69(4), 445-460.
- Liu, E.J., Cashman, K.V., & Rust, A.C. (2015). Optimising shape analysis to quantify volcanic ash morphology. *GeoResJ* (8), 14-30.
- Macedonio, G., Costa, A., Scollo, S., & Neri, A. (2016). Effects of eruption source parameter variation and meteorological dataset on tephra fallout hazard assessment: Example from Vesuvius (Italy). *Journal of Applied Volcanology*, 5(1). <https://doi.org/10.1186/s13617-016-0045-2>
- MacLeod, N.S. Sherrod, D.R., and Chitwood, L.A., and Jensen, R.A. (1995). Geologic map of Newberry volcano, Deschutes, Kalamath, and Lake counties, Oregon: U.S. Geological Survey Miscellaneous Geologic Investigations Map I-2455, scales 1:62,5000 and 1:24,000.
- MacLeod, N.S., and Sherrod, D.R. (1988). Geologic evidence for a magma chamber beneath Newberry Volcano, Oregon. *Journal of Geophysical Research: Solid Earth*, 93(B9), pp.10067-10079.
- Manga, M., Patel, A., & Dufek, J. (2011). Rounding of pumice clasts during transport: field measurements and laboratory studies. *Bulletin of Volcanology*, 73, 321-333.
- Manville, V., Segschneider, B., & White, J. D. L. (2002). Hydrodynamic behaviour of Taupo 1800a pumice: implications for the sedimentology of remobilized pyroclasts. *Sedimentology*, 49(5), 955-976.
- Martel, C., & Schmidt, B. C. (2003). Decompression experiments as an insight into ascent rates of silicic magmas. *Contributions to Mineralogy and Petrology*, 144(4), 397-415.

- Mastin, L.G., Guffanti, M., Servranckx, R., Webley, P., Barsotti, S., Dean, K., Durant, A., Ewert, J.W., Neri, A., Rose, W.I. and Schneider, D. (2009). A multidisciplinary effort to assign realistic source parameters to models of volcanic ash-cloud transport and dispersion during eruptions. *Journal of Volcanology and Geothermal Research*, 186(1-2), pp.10-21.
- Melnik, O., & Sparks, R. S. J. (2002). Dynamics of magma ascent and lava extrusion at Soufrière Hills Volcano, Montserrat. *Geological Society, London, Memoirs*, 21(1), 153-171.
- Mitchell, S.J., Biass, S., Houghton, R.F., Anderson, A., Bonny, E., Walker, B.H., ... & Rosenberg, M.D. (2018). The interplay among clast size, vesicularity, postfragmentation expansion, and clast breakage: An example from the 1.8 ka Taupo eruption. *Field Volcanology: A Tribute to the Distinguished Career of Don Swanson*, 538, 375.
- Miwa, T., Iriyama, Y., Nagai, M., & Nanayama, F. (2020). Sedimentation process of ashfall during a Vulcanian eruption as revealed by high-temporal-resolution grain size analysis and high-speed camera imaging. *Progress in Earth and Planetary Science*, 7(1), 1-16.
- Moitra, P., Gonnermann, H. M., Houghton, B. F., & Giachetti, T. (2013). Relating vesicle shapes in pyroclasts to eruption styles. *Bulletin of volcanology*, 75(2), 1-14.
- Mueller, S., Scheu, B., Kueppers, U., Spieler, O., Richard, D., and Dingwell, D.B. (2011). The porosity of pyroclasts as an indicator of volcanic explosivity. *Journal of Volcanology and Geothermal Research*, v. 203, p. 168–174, <https://doi.org/10.1016/j.jvolgeores.2011.04.006>.
- Mueller, S., Scheu, B., Spieler, O., & Dingwell, D. B. (2008). Permeability control on magma fragmentation. *Geology*, 36(5), 399-402.
- Mueller, S.B., Lane, S.J., & Kueppers, U. (2015). Lab-scale ash production by abrasion and collision experiments of porous volcanic samples. *Journal of Volcanology and Geothermal Research*, 302, 163-172.
- Nathenson, M., Donnelly-Nolan, J.M., Champion, D.E., & Lowenstern, J.B. (2007). Chronology of Postglacial Eruptive Activity and Calculation of Eruption Probabilities for Medicine Lake Volcano, Northern California. Geological Survey Scientific Investigations Report 2007-5174-B, 10 p. [<http://pubs.usgs.gov/sir/2007/5174/b/>].
- Newman, S., & Lowenstern, J. B. (2002). VolatileCalc: a silicate melt–H<sub>2</sub>O–CO<sub>2</sub> solution model written in Visual Basic for excel. *Computers & Geosciences*, 28(5), 597-604.

- Nguyen, C. T., Gonnermann, H. M., & Houghton, B. F. (2014). Explosive to effusive transition during the largest volcanic eruption of the 20th century (Novarupta 1912, Alaska). *Geology*, 42(8), 703-706.
- Ogburn, S. E., Loughlin, S. C., & Calder, E. S. (2015). The association of lava dome growth with major explosive activity ( $VEI \geq 4$ ): DomeHaz, a global dataset. *Bulletin of Volcanology*, 77(5), 1-17.
- Ohashi, M., Ichihara, M., & Toramaru, A. (2018). Bubble deformation in magma under transient flow conditions. *Journal of Volcanology and Geothermal Research*, 364, 59-75.
- Ohashi, M., Ichihara, M., Kennedy, B., & Gravley, D. (2021). Comparison of bubble shape model results with textural analysis: Implications for the velocity profile across a volcanic conduit. *Journal of Geophysical Research: Solid Earth*, e2021JB021841.
- Paisley, R., Berlo, K., Ghaleb, B. and Tuffen, H. (2019). Geochemical constraints on the role of tuffisite veins in degassing at the 2008–09 Chaitén and 2011–12 Cordón Caulle rhyolite eruptions. *Journal of Volcanology and Geothermal Research*, 380, pp.80-93.
- Pal, R. (2003). Rheology of concentrated suspensions of deformable elastic particles such as human erythrocytes. *Journal of biomechanics*, 36(7), 981-989.
- Palladino, D. M., Simei, S., & Kyriakopoulos, K. (2008). On magma fragmentation by conduit shear stress: evidence from the Kos Plateau Tuff, Aegean Volcanic Arc. *Journal of volcanology and geothermal research*, 178(4), 807-817.
- Pallister, J. S., Hoblitt, R. P., & Reyes, A. G. (1992). A basalt trigger for the 1991 eruptions of Pinatubo volcano?. *Nature*, 356(6368), 426-428.
- Papale, P. (1999). Strain-induced magma fragmentation in explosive eruptions. *Nature*, v. 397, p. 425– 428, <https://doi.org/10.1038/17109>.
- Pardo, N., Cronin, S. J., Wright, H. M., Schipper, C. I., Smith, I., & Stewart, B. (2014). Pyroclast textural variation as an indicator of eruption column steadiness in andesitic Plinian eruptions at Mt. Ruapehu. *Bulletin of Volcanology*, 76(5), 822.
- Parmigiani, A., Degruyter, W., Leclaire, S., Huber, C., & Bachmann, O. (2017). The mechanics of shallow magma reservoir outgassing. *Geochemistry, Geophysics, Geosystems*, 18(8), 2887-2905.
- Pérez, W., Freundt, A., and Kutterolf, S. (2020). The basaltic plinian eruption of the ~6ka San Antonio Tephra and formation of the Masay caldera, Nicaragua. *Journal of Volcanology and Geothermal Research*, 401.

- Pfeiffer, T., Costa, A., & Macedonio, G. (2005). A model for the numerical simulation of tephra fall deposits. *Journal of Volcanology and Geothermal Research*, 140(4), 273-294.
- Pinel, V., & Jaupart, C. (2000). The effect of edifice load on magma ascent beneath a volcano. *Philosophical Transactions of the Royal Society of London. Series A: Mathematical, Physical and Engineering Sciences*, 358(1770), 1515-1532.
- Pioli, L., Bonadonna, C., & Pistolesi, M. (2019). Reliability of Total Grain-Size Distribution of Tephra Deposits. *Scientific Reports*, 9(1), 1–15.  
<https://doi.org/10.1038/s41598-019-46125-8>
- Pistolesi, M., Cioni, R., Bonadonna, C., Elissondo, M., Baumann, V., Bertagnini, A., ... & Francalanci, L. (2015). Complex dynamics of small-moderate volcanic events: the example of the 2011 rhyolitic Cordón Caulle eruption, Chile. *Bulletin of Volcanology*, 77(1), 1-24.
- Pistone, M., Cordonnier, B., Caricchi, L., Ulmer, P., & Marone, F. (2015). The viscous to brittle transition in crystal-and bubble-bearing magmas. *Frontiers in Earth Science*, 3, 71.
- Polacci, M., Baker, D. R., Mancini, L., Tromba, G., & Zanini, F. (2006). Three-dimensional investigation of volcanic textures by X-ray microtomography and implications for conduit processes. *Geophysical Research Letters*, 33(13).
- Polacci, M., Papale, P., & Rosi, M. (2001). Textural heterogeneities in pumices from the climactic eruption of Mount Pinatubo, 15 June 1991, and implications for magma ascent dynamics. *Bulletin of Volcanology*, 63(2-3), 83-97.
- Polacci, M., Pioli, L., & Rosi, M. (2003). The Plinian phase of the Campanian Ignimbrite eruption (Plegrean Fields, Italy): evidence from density measurements and textural characterization of pumice. *Bulletin of Volcanology*, 65: 418-432.
- Popa, R. G., Bachmann, O., & Huber, C. (2021). Explosive or effusive style of volcanic eruption determined by magma storage conditions. *Nature Geoscience*, 14(10), 781-786.
- Rahimi, K. (2017). *Understanding the Role of Water in Explosive Eruptions of Kilauea volcano, Hawaii* (Doctoral dissertation, State University of New York at Buffalo).
- Riley, C.M., Rose, W.I., & Bluth, G.J.S. (2003). Quantitative shape measurements of distal volcanic ash. *Journal of Geophysical Research, Solid Earth* 108, 1-15.
- Rose, W. I., & Durant, A. J. (2009). Fine ash content of explosive eruptions. *Journal of Volcanology and Geothermal Research*, 186(1-2), 32-39.

- Rosi, M., Landi, P., Polacci, M., Di Muro, A., & Zandomeneghi, D. (2004). Role of conduit shear on ascent of the crystal-rich magma feeding the 800-year-BP Plinian eruption of Quilotoa Volcano (Ecuador). *Bulletin of Volcanology*, 66(4), 307-321.
- Rosi, M., Vezzoli, L., Castelmennano, A., & Grieco, G. (1999). Plinian pumice fall deposit of the Campanian Ignimbrite eruption (Phlegraean Fields, Italy). *Journal of volcanology and geothermal research*, 91(2-4), 179-198.
- Rotella, M. D., Wilson, C. J., Barker, S. J., Cashman, K. V., Houghton, B. F., & Wright, I. C. (2014). Bubble development in explosive silicic eruptions: insights from pyroclast vesicularity textures from Raoul volcano (Kermadec arc). *Bulletin of Volcanology*, 76(8), 1-24.
- Ruprecht, P., & Bachmann, O. (2010). Pre-eruptive reheating during magma mixing at Quizapu volcano and the implications for the explosiveness of silicic arc volcanoes. *Geology*, 38(10), 919-922.
- Rust, A. C., & Cashman, K. V. (2007). Multiple origins of obsidian pyroclasts and implications for changes in the dynamics of the 1300 BP eruption of Newberry Volcano, USA. *Bulletin of Volcanology*, 69(8), 825-845.
- Rust, A. C., Cashman, K. V., & Wallace, P. J. (2004). Magma degassing buffered by vapor flow through brecciated conduit margins. *Geology*, 32(4), 349-352.
- Rust, A. C., Manga, M., & Cashman, K. V. (2003). Determining flow type, shear rate and shear stress in magmas from bubble shapes and orientations. *Journal of Volcanology and Geothermal Research*, 122(1-2), 111-132.
- Rust, A.C., & Cashman, K.V. (2011). Permeability controls on expansion and size distributions of pyroclasts. *Journal of Geophysical Research: Solid Earth*, 116(11), 1–17. <https://doi.org/10.1029/2011JB008494>
- Rust, A.C., and Cashman, K.V. (2007). Multiple origins of obsidian pyroclasts and implications for changes in the dynamics of the 1300 BP eruption of Newberry Volcano, USA. *Bulletin of Volcanology*, 69(8), pp.825-845.
- Sable, J.E., Houghton, B.F., Wilson, C.J.N., and Carey, R.J. (2006). Complex proximal sedimentation from Plinian plumes: the example of Tarawera 1886. *Bulletin of Volcanology*, 69, 89-103.
- Sahagian, D.L., and Proussevitch, A.A. (1998). 3D particle size distributions from 2D observations: stereology for natural applications. *Journal of Volcanology and Geothermal Research*, 84(3-4), pp.173-196.

- Saxby, J., Beckett, F., Cashman, K., Rust, A., & Tennant, E. (2018). The impact of particle shape on fall velocity: implications for volcanic ash dispersion modelling. *Journal of Volcanology and Geothermal Research*, 362.
- Saxby, J., Rust, A., Beckett, F., Cashman, K., & Rodger, H. (2020). Estimating the 3D shape of volcanic ash to better understand sedimentation processes and improve atmospheric dispersion modelling. *Earth and Planetary Science Letters*, 534.
- Scandone, R., Cashman, K. V., & Malone, S. D. (2007). Magma supply, magma ascent and the style of volcanic eruptions. *Earth and Planetary Science Letters*, 253(3-4), 513-529.
- Schipper, C. I., Castro, J. M., Kennedy, B. M., Tuffen, H., Whattam, J., Wadsworth, F. B., ... & Alloway, B. V. (2021). Silicic conduits as supersized tuffisites: Clastogenic influences on shifting eruption styles at Cordón Caulle volcano (Chile). *Bulletin of Volcanology*, 83(2), 1-22.
- Schipper, C. I., Castro, J. M., Tuffen, H., James, M. R., & How, P. (2013). Shallow vent architecture during hybrid explosive–effusive activity at Cordón Caulle (Chile, 2011–12): evidence from direct observations and pyroclast textures. *Journal of Volcanology and Geothermal Research*, 262, 25-37.
- Schneider, C.A., Rasband, W.S. and Eliceiri, K.W. (2012). NIH Image to ImageJ: 25 years of image analysis. *Nature methods*, 9(7), pp.671-675.
- Schwaiger, H. F., Denlinger, R. P., & Mastin, L. G. (2012). Ash3d: A finite-volume, conservative numerical model for ash transport and tephra deposition. *Journal of Geophysical Research: Solid Earth*, 117 (B4).
- Self, S., & Sparks, R. S. J. (1978). Characteristics of widespread pyroclastic deposits formed by the interaction of silicic magma and water. *Bulletin volcanologique*, 41(3), 196-212.
- Shea, T., Hellebrand, E., Gurioli, L., and Tuffen, H. (2014). Conduit- to Localized-scale Degassing during Plinian Eruptions: Insights from Major Element and Volatile (Cl and H<sub>2</sub>O) Analyses within Vesuvius ad 79 Pumice. *Journal of Petrology*, 55(2), 315-344.
- Shea, T., Houghton, B. F., Gurioli, L., Cashman, K. V., Hammer, J. E., & Hobden, B.J. (2010). Textural studies of vesicles in volcanic rocks: an integrated methodology. *Journal of Volcanology and Geothermal Research*, 190(3-4), 271-289.
- Sheridan, M. F., & Wohletz, K. H. (1983). Hydrovolcanism: basic considerations and review. *Journal of Volcanology and Geothermal Research*, 17(1-4), 1-29.

- Sherrod, D. R. (1997). *Volcano hazards at Newberry volcano, Oregon* (pp. 97-513). The Survey.
- Sherrod, D. R., & MacLeod, N. S. (1979). The last eruptions at Newberry Volcano, central Oregon. In *Geol. Soc. Am. Abstr. Programs* (Vol. 11, No. 3, p. 127).
- Sieh, K., & Bursik, M. (1986). Most recent eruption of the Mono Craters, eastern central California. *Journal of Geophysical Research: Solid Earth*, 91(B12), 12539-12571.
- Sigurdsson, H., Houghton, B., McNutt, S., Rymer, H., & Stix, J. (Eds.). (2015). *The encyclopedia of volcanoes: 2<sup>nd</sup> edition*. Elsevier.
- Sigurdsson, H., Houghton, B., Rymer, H., Stix, J., and McNutt, S. (1999). *The encyclopedia of volcanoes: 1<sup>st</sup> edition*. Elsevier.
- Silva Parejas, C., Lara, L. E., Bertin, D., Amigo, A., & Orozco, G. (2012, April). The 2011-2012 eruption of Cordón Caulle volcano (Southern Andes): Evolution, crisis management and current hazards. In *EGU General Assembly Conference Abstracts* (p. 9382).
- Sparks, R. S. J. (1978). The dynamics of bubble formation and growth in magmas: a review and analysis. *Journal of Volcanology and Geothermal Research*, 3(1-2), 1-37.
- Sparks, R. S. J. & Melnik, O. (1999). Nonlinear dynamics of lava dome extrusion. *Nature* 402, 37–41.
- Spieler, O., Kennedy, B., Kueppers, U., Dingwell, D. B., Scheu, B., & Taddeucci, J. (2004). The fragmentation threshold of pyroclastic rocks. *Earth and Planetary Science Letters*, 226(1-2), 139-148.
- Stevenson, R. J., Dingwell, D. B., Webb, S. L., & Sharp, T. G. (1996). Viscosity of microlite-bearing rhyolitic obsidians: an experimental study. *Bulletin of Volcanology*, 58(4), 298-309.
- Stewart, C., Johnston, D.M., Leonard, G.S., Horwell, C.J., Thordarson, T., & Cronin, S.J. (2006). Contamination of water supplies by volcanic ashfall: a literature review and simple impact modelling. *Journal of Volcanology and Geothermal Research*, 158, 296–306.
- Taddeucci, J., & Wohletz, K. H. (2001). Temporal evolution of the Minoan eruption (Santorini, Greece), as recorded by its Plinian fall deposit and interlayered ash flow beds. *Journal of Volcanology and Geothermal Research*, 109(4), 299-317.



- Taddeucci, J., Pompilio, M., & Scarlato, P. (2002). Monitoring the explosive activity of the July–August 2001 eruption of Mt. Etna (Italy) by ash characterization. *Geophysical Research Letters*, 29(8), 71-1.
- Tait, S., Jaupart, C., & Vergnolle, S. (1989). Pressure, gas content and eruption periodicity of a shallow, crystallising magma chamber. *Earth and Planetary Science Letters*, 92(1), 107-123.
- Till, C. B., Grove, T. L., Carlson, R. W., Donnelly-Nolan, J. M., Fouch, M. J., Wagner, L. S., & Hart, W. K. (2013). Depths and temperatures of < 10.5 Ma mantle melting and the lithosphere-asthenosphere boundary below southern Oregon and northern California. *Geochemistry, Geophysics, Geosystems*, 14(4), 864-879.
- Toramaru, A. (2006). BND (bubble number density) decompression rate meter for explosive volcanic eruptions. *Journal of Volcanology and Geothermal Research*, 154(3-4), 303-316.
- Trafton, K. R., & Giachetti, T. (2021). The morphology and texture of Plinian pyroclasts reflect their lateral sourcing in the conduit. *Earth and Planetary Science Letters*, 562, 116844.
- Tuffen, H., & Dingwell, D. (2005). Fault textures in volcanic conduits: evidence for seismic trigger mechanisms during silicic eruptions. *Bulletin of Volcanology*, 67(4), 370-387.
- Turcotte, D.L. (1997). *Fractals and Chaos in Geology and Geophysics* (second edition): Cambridge, UK, Cambridge University Press, 398 p., <https://doi.org/10.1017/CBO9781139174695>.
- Vitturi, M. D. M., Clarke, A. B., Neri, A., & Voight, B. (2008). Effects of conduit geometry on magma ascent dynamics in dome-forming eruptions. *Earth and Planetary Science Letters*, 272(3-4), 567-578.
- Wadsworth, F. B., Llewellyn, E. W., Vasseur, J., Gardner, J. E., & Tuffen, H. (2020). Explosive-effusive volcanic eruption transitions caused by sintering. *Science Advances*, 6(39), eaba7940.
- Wadsworth, F. B., Vasseur, J., Llewellyn, E. W., Schaubroth, J., Dobson, K. J., Scheu, B., & Dingwell, D. B. (2016). Sintering of viscous droplets under surface tension. *Proceedings of the Royal Society A: Mathematical, Physical and Engineering Sciences*, 472(2188), 20150780.
- Wadsworth, F. B., Vasseur, J., Schaubroth, J., Llewellyn, E. W., Dobson, K. J., Havard, T., ... & Hess, K. U. (2019). A general model for welding of ash particles in volcanic systems validated using in situ X-ray tomography. *Earth and Planetary Science Letters*, 525, 115726.

- Walker, G. P. (1973). Explosive volcanic eruptions—a new classification scheme. *Geologische Rundschau*, 62(2), 431-446.
- Walker, G. P. (1980). The Taupo pumice: product of the most powerful known (ultraplinian) eruption?. *Journal of volcanology and geothermal research*, 8(1), 69-94.
- Walker, G. P. L., Wilson, L., & Bowell, E. L. G. (1971). Explosive volcanic eruptions—I the rate of fall of pyroclasts. *Geophysical Journal International*, 22(4), 377-383.
- Walker, G.W., and MacLeod, N.S. (1991). Geologic map of Oregon: Reston, Va., U.S. Geological Survey, scale 1:500,000.
- Watkins, J.M., Gardner, J.E., and Befus, K.S. (2017). Nonequilibrium degassing, regassing, and vapor fluxing in magmatic feeder systems. *Geology*, v. 45, p. 183–186, <https://doi.org/10.1130/G38501.1>.
- Westrich, H. R., & Eichelberger, J. C. (1994). Gas transport and bubble collapse in rhyolitic magma: an experimental approach. *Bulletin of Volcanology*, 56(6), 447-458.
- White, J. D. L., & Houghton, B. (2000). Surtseyan and related phreatomagmatic eruptions. *Encyclopedia of volcanoes. Academic, San Diego*, 495-513.
- Whitham, A. G., & Sparks, R. S. J. (1986). Pumice. *Bulletin of Volcanology*, 48(4), 209-223.
- Wilson, G., Wilson, T. M., Deligne, N. I., & Cole, J. W. (2014). Volcanic hazard impacts to critical infrastructure: A review. *Journal of Volcanology and Geothermal Research*, 286, 148-182.
- Wilson, L., Sparks, R. S. J., & Walker, G. P. (1980). Explosive volcanic eruptions—IV. The control of magma properties and conduit geometry on eruption column behaviour. *Geophysical Journal International*, 63(1), 117-148.
- Woods, A. (2013). Sustained explosive activity: volcanic eruption columns and Hawaiian fountains. *Modeling Volcanic Processes: The Physics and Mathematics of Volcanism*, 153.
- Woods, A. W., & Koyaguchi, T. (1994). Transitions between explosive and effusive eruptions of silicic magmas. *Nature*, 370(6491), 641-644.
- Wright, H. M., Cashman, K. V., Rosi, M., & Cioni, R. (2007). Breadcrust bombs as indicators of Vulcanian eruption dynamics at Guagua Pichincha volcano, Ecuador. *Bulletin of Volcanology*, 69(3), 281-300.

- Wright, H.M., and Weinberg, R.F. (2009). Strain localization in vesicular magma: Implications for rheology and fragmentation. *Geology*, v. 37, p. 1023–1026, <https://doi.org/10.1130/G30199A.1>.
- Wright, H.M., Cashman, K.V., Mothes, P.A., Hall, M.L., Ruiz, A.G., & Le Pennec, J.L. (2012). Estimating rates of decompression from textures of erupted ash particles produced by 1999–2006 eruptions of Tungurahua volcano, Ecuador. *Geology*, 40(7), 619–622.
- Xue, M., & Allen, R. M. (2006). Origin of the Newberry Hotspot Track: Evidence from shear-wave splitting. *Earth and Planetary Science Letters*, 244(1-2), 315–322.
- Yew, C.H., and Taylor, P.A. (1994). A thermodynamic theory of dynamic fragmentation. *International Journal of Impact Engineering*, v. 15, p. 385–394, [https://doi.org/10.1016/0734-743X\(94\)80023-3](https://doi.org/10.1016/0734-743X(94)80023-3).
- Young, S.R. (1990). Physical volcanology of Holocene airfall deposits from Mt Mazama, Crater Lake, Oregon [Ph.D. thesis]: Lancaster, UK, University of Lancaster, 298 p.
- Zhang, Y. (1999). A criterion for the fragmentation of bubbly magma based on brittle failure theory. *Nature*, v. 402, p. 648–650, <https://doi.org/10.1038/45210>.
- Zhang, Y., Xu, Z., Zhu, M., & Wang, H. (2007). Silicate melt properties and volcanic eruptions. *Reviews of Geophysics*, 45(4).